European Funds
Knowledge Education Development

European Union
European Social Fund

„BioTechNan - the programme of interdisciplinary cross-institutional post gradual studies KNOW
in the field of Biotechnology and Nanotechnology"

Application of nonlinear optics methods in sensing
Zastosowanie metod optyki nieliniowej w sensoryce

mgr inż. Krzysztof Nadolski

Supervisors:

dr hab. inż. Katarzyna Matczyszyn, prof. PWr,
Wrocław University of Science and Technology, Poland

Prof. Pierre-François Brevet, Institut Lumière Matière,
Université Claude Bernard Lyon 1, France

Wrocław 2023

Wrocław University of Science and Technology
Uniwersytet Wrocławski
Wrocław University of Environmental and Life Sciences

The project is co-financed by the European Union from the European Social Fund

Université Claude Bernard Lyon 1
iLM Institut Lumière Matière

Acknowledgements

First of all, I would like to thank the supervisors of my Bachelor and Master theses, who I took my first steps in science with: **Prof. Ewa Rysiakiewicz-Pasek** and **Prof. Joanna Olesiak-Bańska**.

I would like to express my acknowledgment to my PhD thesis supervisors, **Prof. Katarzyna Matczyszyn** and **Prof. Pierre-François Brevet**, who always believed in me and guided me during my PhD studies.

This work would not be possible without support of **my colleagues from Wroclaw University of Science and Technology and Institut Lumière Matière**. I would like to thank you for always being ready to help me, as well as for our non-scientific discussions, which made this time very pleasant and facilitated coping with failures, which cannot be avoided during research.

Last but not least, I would like to thank **all my nearest and dearest**, who supported me during this time.

Outline

1. List of abbreviations

2D	Two-dimensional
AC	Alternating current
ACF	Auto-correlation function
AD	Anno Domini
AR	Aspect Ratio
ATR	Attenuated Total Reflection
AuNPs	Gold nanoparticles
C18-SH	1-Octadecanethiol
c.c.	Complex conjugate
CTAB	Hexadecyltrimethylammonium bromide
Cu	Copper
$CuBr_2$	Copper (II) Bromide
CVD	Chemical Vapor Deposition
DDA	Discrete Dipole Approximation
DFCI	Dark Field Confocal Imaging
DFG	Difference-Frequency Generation
DLS	Dynamic Light Scattering
DSEH	Differential Sediment Entrainment Hypothesis
EDS	Energy-Dispersive (Detector)
esu	Electrostatic units in the cgs system of units
FDTD	Finite Difference Time Domain
FEM	Finite Element Method
FoM	Figure of Merit
FRET	Förster Resonance Energy Transfer
H	Horizontally-polarized signal (in the case of HRS polarization analysis)
HRS	Hyper Rayleigh Scattering
L-LSPR	Longitudinal LSPR
LSPR	Localised Surface Plasmon Resonance
MBE	Molecular Beam Epitaxy
MBI	2-mercaptobenzimidazole
NPs	Nanoparticles

OLED	Organic Light Emitting Diode
OR	Optical Rectification
PVP	polyvinylpyrrolidone
RIU	Refractive Index Unit
ROS	Reactive Oxygen Species
R6G	Rhodamine 6G
SEM	Scanning Electron Microscopy
SERS	Surface Enhanced Raman Scattering
SFG	Sum-Frequency Generation
SHG	Second Harmonic Generation
SIM	Surface Integral Method
SPR	Surface Plasmon Resonance
S-SHG	Surface Second Harmonic Generation
TEM	Transmission Electron Microscopy
T-LSPR	Transverse LSPR
UHV	Ultra High Vacuum
UV-Vis	Ultraviolet-Visible spectroscopy (or: spectrum)
V	Vertically-polarized signal (in the case of HRS polarization analysis)

2. Abstract in English

The thesis entitled “Application of nonlinear optics methods in sensing” was prepared under supervision of Prof. Katarzyna Matczyszyn from Institute of Advanced Materials, Wroclaw University of Science and Technology, Poland, and Prof. Pierre-François Brevet from Institut Lumière Matière, Université Claude Bernard Lyon 1, Villeurbanne/Lyon, France. It was a part of the “BioTechNan - the programme of interdisciplinary cross-institutional post gradual studies KNOW in the field of Biotechnology and Nanotechnology” programme, co-financed by the European Union from the European Social Fund. The original work language of this thesis is English.

The thesis is divided into 7 chapters, the first one including a list of abbreviations used in the work. Further, an abstract in English and Polish language is presented. Chapter 4 includes theory crucial to understand the study. With a brief introduction to the fabrication methods of gold nanoparticles, focusing on the *Turkevich* method, the author follows with characterization methods, used in this study: UV-Visible spectroscopy, Transmission Electron Microscopy, Zeta potential measurements and Dynamic Light Scattering. Chapter 4.3 is dedicated to nanoplasmonics, including Maxwell-Garnett theory, Drude model and Localised Surface Plasmon Resonance description. Afterwards, the most crucial terms of nonlinear optics are introduced. A general problem includes a comparison of linear and nonlinear optical processes, with a theoretical explanation on the origin of each. The specificity of various nonlinear optical processes is mentioned, as well as the corresponding Jablonski diagrams. This leads to the meaning of a symmetry centre for nanoparticles, described in Chapter 4.4.1, followed by the method of Hyper Rayleigh Scattering (HRS) section number 4.4.2 with a description of the Hyper-Rayleigh Scattering phenomenon itself and a depiction of a typical HRS measurement setup. A subsection 4.4.2.1 includes polarization-resolved measurements. The definition, origin and meaning of retardation parameters ζ^V and ζ^H, as well as depolarization ratio D^V are discussed. A short review on HRS of metallic nanoparticles is included in 4.4.3. The reader is guided through HRS studies of silver and gold nanoparticles of various sizes and centrosymmetrical shapes. The last subchapter of the theoretical introduction, namely 4.5, focuses on the applications with gold nanoparticles: starting with the older publications and moving to the recent use published in the scientific literature. This subchapter includes a subsection 4.5.1, dedicated to sensing, explaining crucial attributes of a good sensor.

Chapter 5, called *Results and discussion* is divided in four parts. 5.1 is dedicated to a PhD candidate statement about the substantive contribution to the presented publications,

meanwhile sections 5.2-5.4 include the synopsis of each publication and the publication itself. Section 5.2 considers gold nanotriangles as an example of non centrosymmetrically-shaped nanoparticles. Centrosymmetric nanoparticles, such as nanospheres, nanorods or nanocubes are well described in the literature. The behaviour of the latters is driven by volume-dependent phenomena although experimentally the consequences of the imperfect geometrical shapes are observed as well. In our current work, nanotriangles of mean edge length ranging from 26 to 87 nm were synthesised and characterised. Noteworthy, the samples contained significant amount of nanospheres, i.e. from 26 to 58%, thus it is a novel approach to study a mixture of various shapes. The first hyperpolarizability is significantly lower compared to centrosymmetric nanoparticles, however the influence of stabilizing agent is unsure: in fact, the values for triangles and spheres from this synthesis are close. Furthermore, it is revealed that the HRS signal exhibits a surface-dependent behaviour also for big nanoparticles, which is contradictory to centrosymmetrical nanoparticles, for which the electric dipole approximation is not sufficient above 50 nm diameter. Indeed, it is further confirmed by polarization-resolved studies that the retardation parameters, whose growth is associated with size increase in the case of centrosymmetrical nanoparticles, remain low. The depolarization ratio demonstrates a value of around 0.45, far from 0.2 expected for a point-like one-fold structure, in line with a dominant three-fold symmetry.

The HRS response of gold nanotriangles is rather driven by their non centrosymmetrical shape, than the size growth. They are an excellent fit for applications where a low retardation level is desired.

Section 5.3 describes the influence of surrounding medium on the HRS response of gold nanospheres. The surrounding medium refractive index was modified by introduction of different amounts of glycerol into 40 and 100 nm nanospheres' suspensions. The HRS signal exhibits an abrupt drop for low glycerol additions, followed by an increase. This cannot be explained in terms of Localized Surface Plasmon Resonance (LSPR) peak shift, thus it is addressed to surface-specific processes. The change is more significant for smaller nanoparticles, however shift of the irradiation wavelength from 820 to 790 nm does not impact the outcome essentially. All polarization-resolved parameters, i.e. the depolarization ratio and retardation parameters present a non monotonous behaviour with the increase of the refractive index. A the lowest glycerol contents, which is desired for sensing purposes, a drop in intensity is observed. Thus, the relative HRS signal change per Refractive Index Unit (RIU) is considered as a Figure of Merit of choice and equals about 4000. It is observed from UV-Vis spectra that the colorimetry is not suitable for detection of such low changes.

Detection of metal ions with use of Hyper Rayleigh Scattering from gold nanoparticles is considered in Chapter 5.4. 50 nm mean diameter nanospheres with copper (II) bromide concentration ranging from 0 to 25 mM were studied. First of all, Dynamic Light Scattering (DLS) and Zeta potential measurements were performed along with UV-Visible spectroscopy to understand the nature of phenomena. It was confirmed that in the case of small copper addition, namely below 1 mM concentration, rather weak ionic interactions between copper and citrate dominate, building corona-like structures, associated with a red-shift of the LSPR peak in the UV-Visible spectra. Above this limit, appearance of a new broad peak around 780 nm is observed, caused by aggregation of nanoparticles. In the meantime, the hydrodynamic diameter exhibits a significant increase over 1 mM $CuBr_2$, meanwhile the Zeta potential notes an abrupt change for low copper content, followed by a plateau. The HRS signal decreases by around 20% until 0.5 mM copper (II) bromide, where it starts to grow. Over 5 mM it reaches a plateau, affected by essential absorption at the incident wavelength 800 nm. The depolarization ratio grows until 5 mM copper ion concentration, and then reaches a value of 0.44. The ζ^{H} retardation parameter is vanishingly small for low copper addition and is not further discussed in frames of sensing purposes. ζ^{V} exhibits a rapid growth, followed by a decrease and stabilization from around 1mM. Various possibilities of defining a Figure of Merit are discussed. The FoM of choice is based on the relative HRS signal change.

A summary of the studies conducted within this thesis can be found in Chapter 6. It is pointed out, that gold nanotriangles are a promising tool for sensing thanks to its low signal retardation. Moreover, gold nanospheres are an appropriate tool for detection of both surrounding medium refractive index changes and metal ion presence. Several significant issues are named, which should be further studied, such as the influence of sharp tips for metal ion detection along with the selectivity, or meaning of the nanoparticle shape in both sensing cases.

Chapter 7 includes literature references.

3. Abstract in Polish

Niniejsza praca zatytułowana „Zastosowanie metod optyki nieliniowej w sensoryce" została przygotowana pod opieką prof. Katarzyny Matczyszyn z Instytutu Materiałów Zaawansowanych, Politechnika Wrocławska, Polska, oraz prof. Pierre'a-François Breveta z Institut Lumière Matière, Université Claude Bernard Lyon 1, Villeurbanne/Lyon, Francja. Była częścią programu „BioTechNan – Program Interdyscyplinarnych Środowiskowych Studiów Doktoranckich KNOW z obszaru Biotechnologii i Nanotechnologii", współfinansowanego przez Unię Europejską w ramach Europejskiego Funduszu Społecznego. Oryginalnym językiem pracy jest język angielski.

Praca została podzielona na 7 rozdziałów, z których pierwszy zawiera listę skrótów użytych w pracy. Następnie zaprezentowano streszczenie pracy w językach angielskim i polskim. Rozdział 4. zawiera teorię kluczową dla zrozumienia niniejszych badań. Zaczynawszy krótkim wstępem do metod otrzymywania nanocząstek złota, skupiając się na *metodzie Turkevicha*, autor przechodzi do metod charakteryzacji użytych w badaniach: spektroskopii UV-Vis, Transmisyjnej Mikroskopii Elektronowej (ang. Transmission Electron Micoscopy), pomiarom Zeta potencjału oraz Dynamicznemu Rozpraszaniu Światła (ang. Dynamic Light Scattering). Rozdział 4.3 jest krótkim wstępem do nanoplazmoniki, wraz z teorią Maxwella-Garnetta, modelem Drude'a i Zlokalizowanym Powierzchniowym Rezonansem Plazmonowym (ang. Localised Surface Plasmon Resonance). Następnie wprowadzono najważniejsze pojęcia z zakresu optyki nieliniowej. Ogólny wstęp zawiera porównanie procesów optycznie liniowych i nieliniowych, wraz z teoretycznym wyjaśnieniem każdego z nich. Charakterystyka różnych procesów nieliniowych optycznie jest przytoczona wraz z ich diagramami Jabłońskiego. To prowadzi do znaczenia środka symetrii nanocząstek, jak opisano w sekcji 4.4.1, po której następuje sekcja 4.4.2 z opisem Hiperrozpraszania Rayleigha (ang. Hyper Rayleigh Scattering) i przedstawieniem typowego układu do pomiarów HRS. Podsekcja 4.4.2.1. dotyczy pomiarów analizy polaryzacyjnej. Przedyskutowano pochodzenie i znaczenie parametrów retardacji ζ^V i ζ^H, jak również współczynnika depolaryzacji D^V. Następnie można znaleźć krótki przegląd HRS metalicznych nanocząstek w 4.4.3. Czytelnik jest prowadzony przez badania HRS nanocząstek złota i srebra różnych rozmiarów i centrosymetrycznych kształtów. Ostatni podrozdział wstępu teoretycznego, to znaczy 4.5, skupia się na zastosowaniu nanocząstek złota: zaczynając od tych dawniejszych, po ówczesne doniesienia publikowane w literaturze naukowej. Ten podrozdział zawiera podsekcję 4.5.1, poświęconą detekcji, opisując istotne właściwości dobrego sensora.

Rozdział 5, nazwany *Wyniki i dyskusja* (ang. *Results and discussion*) jest podzielony na cztery części. Rozdział 5.1. zawiera deklarację doktoranta o wkładzie do prezentowanych publikacji, podczas gdy rozdziały 5.2-5.4 zawierają podsumowanie danej publikacji i samą publikację.

Sekcja 5.2 dotyczy nanotrójkątów złota jako przykład niecentrosymetrycznych nanocząstek. Centrosymetryczne nanocząstki, takie jak nanokulki, nanopręty czy nanokostki, są dobrze opisane w literaturze. Ich zachowanie jest spowodowane przez procesy zależne od objętości. W tej pracy zsyntezowano i scharakteryzowano nanotrójkąty o średniej długości krawędzi w zakresie od 26 do 87 nm. Warto zauważyć, że próbki zawierały znaczne ilości nanokulek, to znaczy od 26 do 58%, więc jest to nowe podejście badania mieszaniny różnych kształtów. Pierwsza hiperpolaryzowalność jest zdecydowanie mniejsza w porównaniu do nanocząstek centrosymetrycznych, niemniej jednak niepewny pozostaje wpływ stabilizatora: w rzeczywistości wartości dla trójkątów i kulek z tej konkretnej syntezy są bliskie sobie. Ponadto, okazało się, że sygnał HRS jest procesem zależnym od powierzchni również w przypadku dużych nanocząstek, w przeciwieństwie do przypadku nanocząstek centrosymetrycznych, dla których przybliżenie dipolowe nie jest adekwatne powyżej 50 nm średnicy. Analiza polaryzacyjna sygnału dowiodła, że parametry retardacji, których zwiększanie się jest związane ze wzrostem rozmiaru w przypadku nanocząstek centrosymetrycznych, pozostają małe. Parametr depolaryzacji ma wartość około 0.45, co jest dalekie od 0.2, wartości oczekiwanej dla punktowej struktury o symetrii jednokrotnej.

Odpowiedź HRS nanotrójkątów złota jest raczej zdominowana przez ich niecentrosymetryczny kształt, niż wzrost rozmiaru. Są one świetnym wyborem dla zastosowań, gdzie pożądany jest niski poziom retardacji sygnału.

Sekcja 5.3 opisuje wpływ ośrodka na odpowiedź HRS nanokulek złota. Współczynnik załamania światła był modyfikowany przez wprowadzenie różnych ilości gliceryny do zawiesin 40- i 100-nanometrowych nanokulek. Sygnał HRS wykazuje nagły spadek dla małych dodatków gliceryny, a następnie wzrost. Nie może to zostać uzasadnione poprzez przesunięcie spektralne LSPR, a raczej trzeba się pochylić nad procesami na powierzchni nanocząstek. Zmiana jest bardziej widoczna dla mniejszych nanocząstek, aczkolwiek zmiana długości fali wzbudzenia z 820 na 790 nm nie powoduje istotnych zmian w wyniku. Wszystkie parametry polaryzacyjne, tj. współczynnik depolaryzacji i współczynniki retardacji oscylują, za wyjątkiem najmniejszych zawartości gliceryny, co jest obszarem pożądanym w przypadku zastosowań do detekcji. Jako kryterium jakości (ang. *Figure of Merit*) zaproponowano względną zmianę sygnału HRS w przeliczeniu na jednostkę załamania światła (ang. *Refractive Index Unit, RIU)*, wynosi ona w tym przypadku około 4000. Z widm spektroskopii UV-Vis można zauważyć, że kolorymetria nie jest metodą odpowiednią do badania tak niskich stężeń.

Detekcja jonów metali przy użyciu HRS nanocząstek złota jest rozważana w rozdziale 5.4. W badaniach wykorzystano nanokulki o średniej średnicy 50 nm ze stężeniem bromku miedzi (II) w zakresie od 0 do 25 mM. Po pierwsze, Dynamiczne Rozpraszanie Światła (*ang. Dynamic Light Scattering*) oraz Zeta potencjał zostały zmierzone wraz ze spektroskopią UV-Vis, żeby zrozumieć naturę zachodzących zjawisk. Stwierdzono, że w przypadku małych zawartości miedzi, czyli stężeniu poniżej 1 mM, dominują raczej słabe oddziaływania jonowe między miedzą i cytrynianem i powstają struktury koronowe, związane z przesunięciem ku czerwieni pasma LSPR w widmach UV-Vis. Powyżej tej granicy obserwuje się pojawienie się nowego szerokiego pasma z maksimum dla około 780 nm, spowodowane agregacją nanocząstek. Tymczasem średnica hydrodynamiczna wykazuje znaczny wzrost powyżej 1mM $CuBr_2$, a potencjał Zeta zmienia się nagle dla małej zawartości miedzi, a następnie jego wartość stabilizuje się. Sygnał HRS maleje o około 20% do 0.5 mM bromku miedzi (II), po czym zaczyna rosnąć. Powyżej 5 mM osiąga plateau, powiązane ze znaczną absorpcją długości fali 800 nm. Współczynnik depolaryzacji rośnie do stężenia jonów miedzi 5 mM, i osiąga wartość około 0.44. Parametr retardacji sygnału ζ^{H} jest zanikająco mały dla małych zawartości miedzi, w związku z tym został on wykluczony do zastosowań w detekcji jonów metali. ζ^{V} wykazuje nagły wzrost, a następnie maleje i stabilizuje się powyżej 1 mM. Różne możliwe definicje kryterium jakości zostały opisane. Zdecydowano się na kryterium oparte na względnej zmianie sygnału HRS.

W rozdziale 6. można znaleźć podsumowanie badań przeprowadzonych w trakcie studiów doktoranckich. Podkreślono, że nanotrójkąty złota są obiecującym narzędziem dla sensingu dzięki niewielkiej retardacji sygnału HRS. Co więcej, nanokulki złota są dobrym materiałem do detekcji zarówno zmian współczynnika załamania światła, jak i obecności jonów metali. Wspomniano o kilku istotnych kwestiach, które wymagają jeszcze lepszego zgłębienia, takich jak wpływ ostrych zakończeń do detekcji jonów metali oraz selektywność tej metody, czy też znaczenie kształtu nanocząstek w obu dyskutowanych przypadkach detekcji.

Rozdział 7. zawiera bibliografię.

4. Introduction

4.1. Fabrication of nanomaterials

Even though the focus of this work is not the preparation of gold nanoparticles of new sizes or shapes, the description of the fabrication process and the final composition is crucial to understand the occurring phenomena.

Nanomaterials can be obtained by two approaches: top-down or bottom-up[1]. The top-down methods are based on decomposition of larger objects, meanwhile the bottom-up methods base on composing (as opposed to decomposing).

One of the most commonly used top-down method is nanolithography, which uses charged ions, electron beams or light to transfer a geometric pattern onto a substrate,[2] see Figure 1. It was proven to be possible to fabricate materials of dimensions lower than 10 nm,[3] however due to long fabrication time, the requirement of high surface finished materials, high costs and imperfections, bottom-up methods are preferred for many applications.

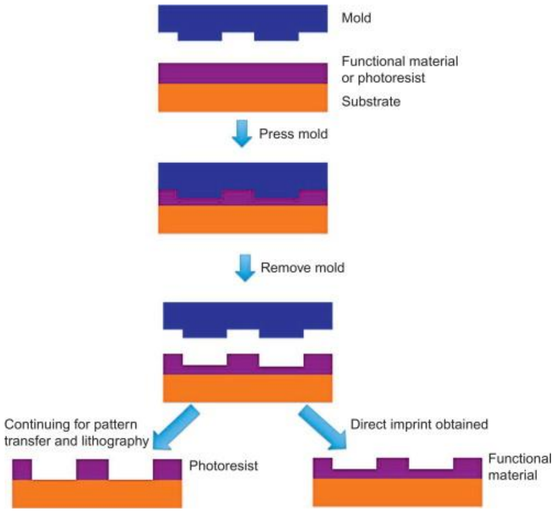

Fig. 1. The principle of nanolithography. Reprinted from [2].

Bottom-up methods include Molecular Beam Epitaxy (MBE).[4] In simple words, this method can be understood as shooting molecules at a substrate. The substrate must be first heated to very high temperatures, usually hundreds of Celsius degrees.[5-6] The atoms or molecules are placed in effusion cells. Fired onto the substrate, the molecules condense and build very slowly and systematically very thin layers. Apart from high temperatures (which excludes many compounds, not temperature-resistant), this method requires Ultra High Vacuum (UHV), which makes it suitable for layers of semiconductors.[7]

An alternative to MBE is Chemical Vapor Deposition (CVD),[8] where a vapor is undergone a chemical reaction in the vicinity of heated substrate surface, and deposited as a solid material. It allows to fabricate a big variety of materials, due to its flexibility in substrate material and temperature, reacting gas composition or applied pressure. However, this method is mostly used for thin film fabrication, but also solar cells,[9] ceramics[10] or carbon nanotubes[11] can be obtained.

The described fabrication methods of nanomaterials are well suitable for preparation of thin layers, nevertheless they are not favourable for plasmonic nanoparticles, where chemical synthesis is usually applied, being another bottom-up fabrication method, which will be described in detail in Chapter 4.1.1.

4.1.1. Chemically synthesized colloidal gold nanoparticles

The most widely applied method of gold nanoparticles' fabrication is chemical synthesis, allowing to obtain nanoparticles of various shapes and sizes, in various surroundings. The current thesis is not focusing on the fabrication process, however understanding the basic principles is crucial.

Synthesis of colloidal gold nanoparticles has been described for the first time by J. Turkevich in 1951, thus this method is nowadays called the *Turkevich method.*[12] Namely, chloroauric acid ($HAuCl_4$) was treated in boiling water with sodium citrate, which acted both as a reducing and stabilizing agent. Nanoparticles of mean size 10-20 nm were synthesized, thus this method was refined by G. Frens, who studied different concentrations of the citrate, which resulted in colloidal gold nanoparticles of different sizes[13] (literature sometimes refers to *Turkevich-Frens* method): from 16 to 147 nm mean diameter.

Gold nanorods, an example of anisotropic gold nanoparticles, have been widely described too. They exhibit two plasmon modes: a longitudinal and a transverse one, connected with oscillation along their longer and shorter axes, respectively.[14] One of the most commonly applied protocols is the seed-mediated growth method.[15-17] Chloroauric acid is added to ice-cooled borane, which reduces gold from Au^{3+} to Au^{0} state. Cetyltrimethylammonium bromide (CTAB) plays the stabilizing role. The product of this reaction was further used as the so-called *seed*. In the next step, chloroauric acid is added to ascorbic acid, which reduces gold from Au^{3+} to Au^{1+} in presence of CTAB micelles. Afterwards, a solution of silver nitrate is added, responsible for the shape formation. Finally, seed is injected. Alternatively, other capping agents than CTAB can be used either directly in the synthesis or in post-synthesis treatment, including citrate[18] or poly(sodium 4-styrenesulfonate) (PSS).[19]

Since for several applications sharp tips, absent in nanorods, are advantageous, scientists have studied other shapes, such as bipyramids,[20-21] triangles,[22-23] stars,[24-25] cubes,[26] cages[27] or popcorn.[28] Nevertheless, keep in mind that nanorods used to be considered as owing sharp tips, as opposed to nanospheres.[29-31] Exemplary TEM pictures of each nanoparticle shape are presented in Figure 2 (a) – (g). In the case of most shapes, nanoparticles of various sizes have been well-studied. For instance, for nanorods "mini gold nanorods" of a few nanometers,[32] "standard" nanorods of 30-50 nm [33] or long nanorods of ~100 nm [34] are known.

For biological applications gold nanoparticles can be obtained in a bio-mediated synthesis. M. Klekotko reported a synthesis protocol, where an extract of *Mentha piperita* was used as reducing and stabilizing agent.[35] Their toxicity, compared to gold nanoparticles obtained by a standard method, was significantly lower. Nevertheless, they were less monodisperse in shape and size compared to gold nanoparticles obtained in a conventional way.

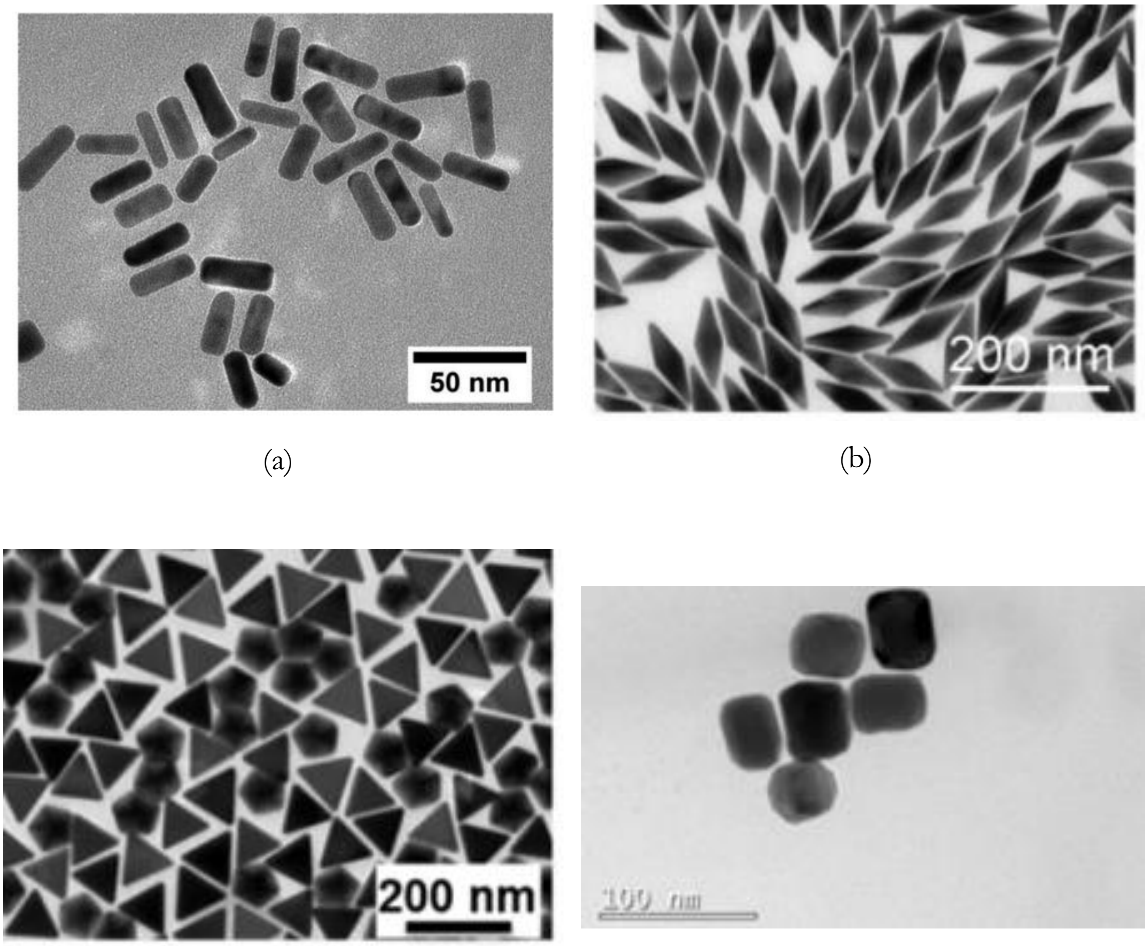

(a)

(b)

(c)

(d)

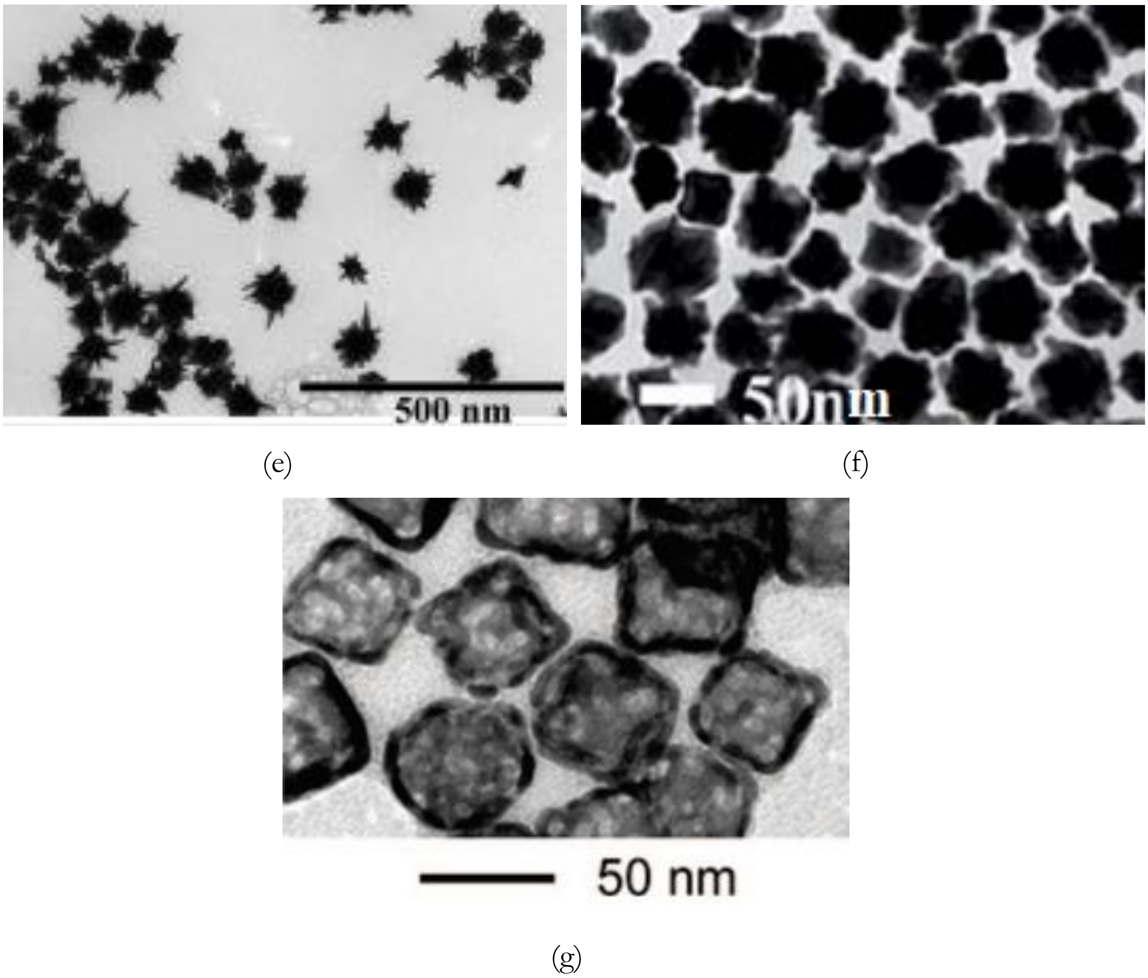

(e) (f)

(g)

Fig. 2 (a) – (g). Exemplary TEM pictures of gold nanoparticles of different shapes: (a) nanorods,[33] (b) nanobipyramids,[36] (c) nanotriangles,[37] (d) nanocubes,[38] (e) nanostars,[39] (f) nanopopcorn[40] and (g) nanocages.[41] Reprinted from the cited publications, respectively.

4.2. Characterization methods

This chapter is dedicated to explain the different characterization methods, used to describe the nanoparticles during the research. Each sub-chapter provides a brief summary of theory connected with the techniques, as well as the information that they provide.

4.2.1. UV-Vis spectroscopy

Bohr and Einstein stated the relation $\Delta E = h\nu$ with $h = 6.626 \cdot 10^{-34} Js$ the Planck constant and ν the photon frequency. The quantification of light energy is the foundation of optical spectroscopy.[42] Furthermore, according to the Bouguer-Lambert-Beer law:[42]

$$A = log\frac{I_0}{I} = \varepsilon cd \quad (1).$$

Where A is the absorbance, I_0 and I the light intensity prior and after the sample respectively, ε is defined as the molar extinction coefficient and d the path length of the sample, given in cm. ε is characteristic for a substance and depends on wavelength. The molar concentration c is given in mol/dm^3. The correlation between A and wavelength λ is called the *absorption spectrum*. In these measurements, a reference, mostly the solvent used in the specimen, is required to eliminate its influence on the signal. In spectroscopy, usually UV, Visible and Infrared ranges are studied, see Figure 3.

Extinction and *absorption* are sometimes used ambiguously, however $extinction = absorption + scattering$. For gold nanoparticles, scattering plays a crucial role for large nanoparticles, i.e. $\gg 50\ nm$.[43]

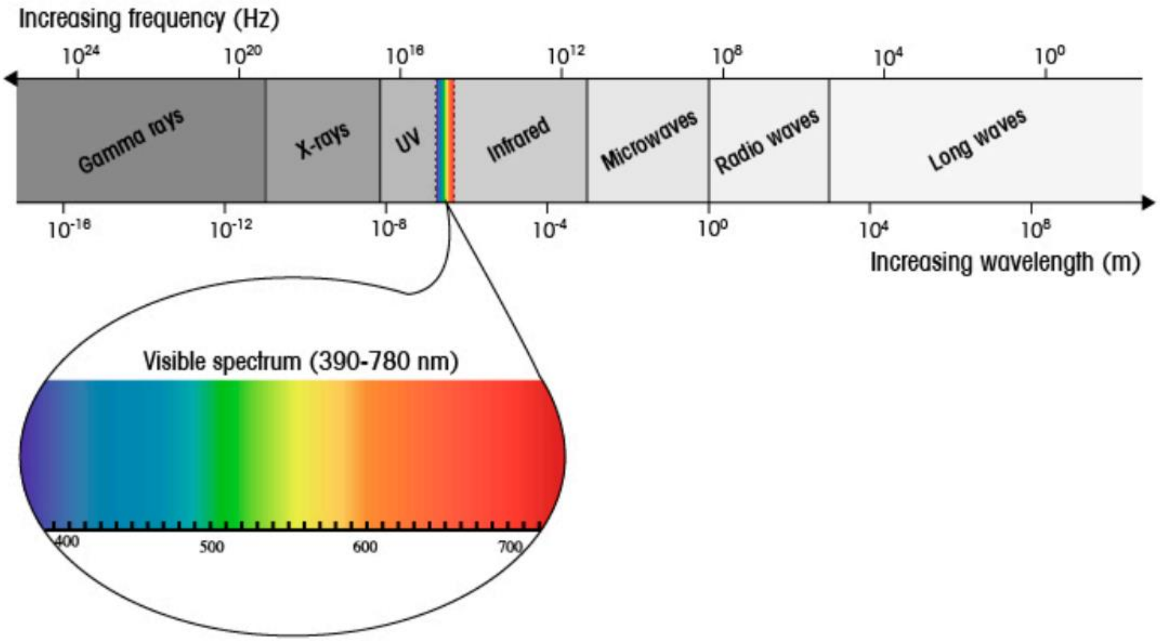

Fig. 3. Depiction of various types of electromagnetic waves, split by wavelength range. UV-Vis spectroscopy focuses on UV and Visible parts and partially Infrared ranges. Reprinted from [44].

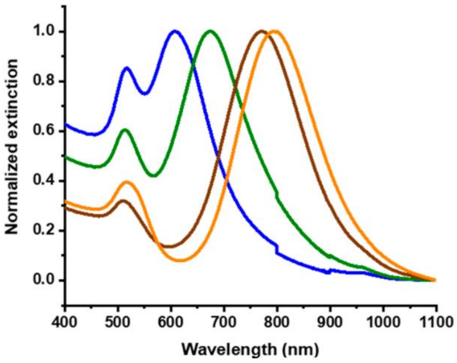

Fig. 4. An example of usage of UV-Vis spectroscopy to monitor nanoparticles' synthesis. The curves show spectra of 2.2, 2.6, 3.2 and 3.8 Aspect Ratio (AR) (from left to right, respectively) mini nanorods. Reprinted from [32].

As will be discussed in Section 4.3, extinction of nanoparticles, i.e. its intensity and spectral localization, is connected with the nanoparticles' shape and size and thus it is a simple and quick monitoring tool. See Figure 4 for an example, where UV-Vis spectroscopy was used to monitor the aspect ratio of synthesized mini gold nanorods.[32] On the other hand, colorimetry-based sensing is a wide field, where changes in UV-Vis spectra are used as a detection tool, which will be further described in Chapter 4.5.

4.2.2. TEM microscopy

Although it has been proven that UV-Visible spectroscopy, described in chapter 4.2.1, may help to resolve the size of gold nanoparticles,[45] it remains insufficient when more quantitative data is required, i.e. a size distribution, or a mixture of different shapes is suspected. Thus, microscopy shall be addressed. A crucial parameter of classical optical microscopy is resolution limit, which however does not allow to investigate structures of size in the range of 10-100 nm. For metallic nanoparticles, since they are conductive, electron microscopy is suitable, with two mostly applied techniques in gold nanoparticles imaging: Scanning Electron Microscopy (SEM) and Transmission Electron Microscopy (TEM). Table 1 contains comparison of chosen properties of light microscopy, SEM and TEM. The wavelength of radiation for electron microscopy techniques was calculated based on the *De Broglie Relation:*[46]

$$\lambda = \frac{h}{p} = h/(mv) \qquad (2),$$

Where p stands for momentum, m mass and v velocity of electrons.[47] Note that the wavelength associated with electrons is comparable to atomic dimensions, thus diffraction or backscattering may be observed. First observation of electron diffraction at the surface of a crystal was noted by Davisson and Germer in 1927.[48]

Table 1. Comparison of chosen properties of light microscopy, Scanning Electron Microscopy (SEM) and Transmission Electron Microscopy (TEM). Reprinted from [49].

Characteristics	Light microscope	SEM	TEM
Wavelength of radiation	Visible light: ~380-760 nm	0,008 nm at 20 kV accelerating voltage	0,0028 nm at 200 kV accelerating voltage
Useful magnification	1 000x	200 000x	2 000 000x
Resolution	200 nm	1 nm	0,1 nm
Specimen thickness	thin, bulk	bulk	thin (electron transparent, ~100 nm)
Examination of live specimens	possible	impossible	impossible
Capital and maintenance cost	low	medium	high
Features studied	surface	surface or subsurface	microstructure

A scheme of TEM and SEM arrangements, as well as conventional light microscopy, is presented in Figure 5. Principally, in Transmission Electron Microscopy, transmitted signal is recorded. This requires thinner specimen, yet the obtained resolution is in the range of 0.1 nm. Contrarily, SEM, working on backscattering, resolution is ~10 times lower, meanwhile it is less expensive and more facile in use. Nowadays both techniques are widely applied for determination of size and shape of gold nanoparticles.[50-53]

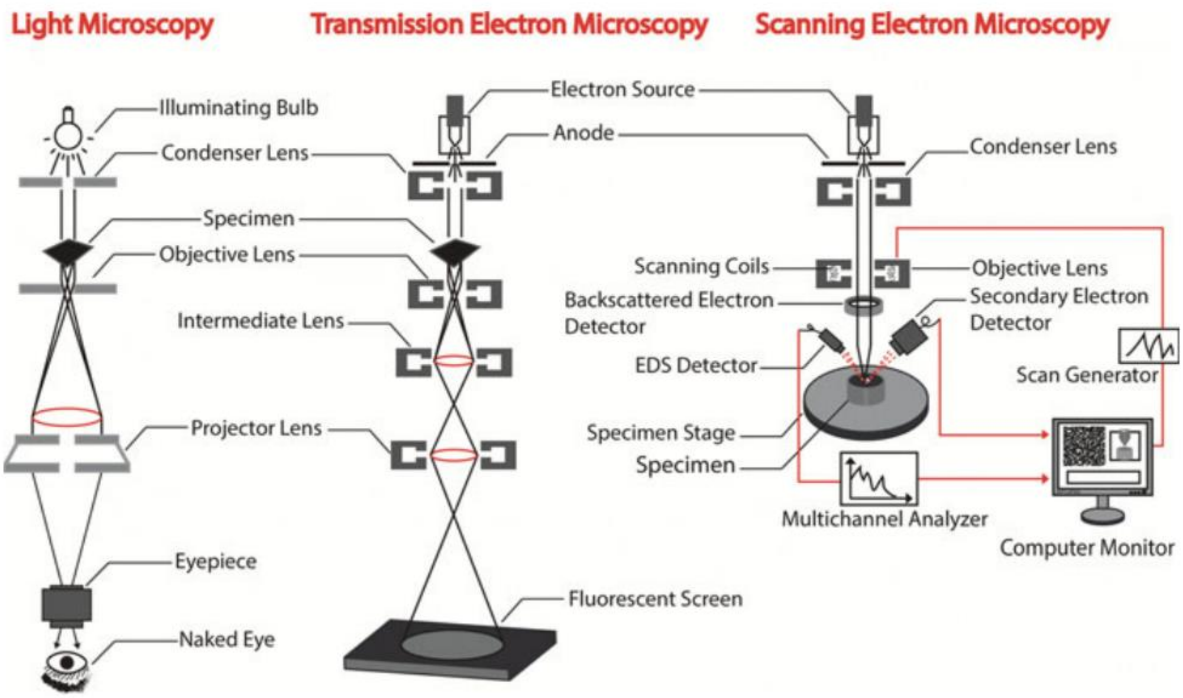

Fig. 5. Schematic comparison of light microscopy, TEM and SEM arrangements. Reprinted from [49].

4.2.3. Zeta potential

UV-Vis spectroscopy and TEM provide information about nanoparticles' morphology, however they are not sufficient alone for nanoparticles' vicinity. UV-Vis spectra may be affected by for instance binding (or generally speaking: interactions) of different molecules[54] or refractive index change,[55] however it is not an equivocal indicator: in some cases, the study of potential on the nanoparticle's surface is required.

Zeta ζ potential is the potential at the slipping plane. It is based on the electroosmosis phenomenon, where applied external electric field allows to obtain the Zeta potential value.[56] The measurements are based on the *Helmholtz-Smoluchowski* equation:

$$u = -\frac{\varepsilon\varphi_0}{\eta}E \tag{3}$$

with u the electroosmotic velocity, ε solvent permittivity, η solvent viscosity, E extrinsic electric field and φ_0 surface potential.

From eq. (3) Zeta potential can be described as:

$$\zeta = -\frac{\mu_{EO}\eta}{\varepsilon} \qquad (4).$$

Where μ_{EO}, the electroosmotic mobility, is defined as:

$$\vec{u} = \mu_{EO}\vec{E} \qquad (5).$$

Zeta ζ potential is a good indicator of the surface state especially in chemically simple environments.[57] In the case of complex biological environments, the outcome is not trivial.[58] The results are also affected if the nanoparticles are small or placed in a polydisperse system.[59]

4.2.4. Dynamic Light Scattering

Methods such as TEM or SEM require deposition of the analyte onto a substrate. An example of a method, where the nanoparticles' size may be examined in solution, is Dynamic Light Scattering, whose principles are described in this section.

If light is irradiated onto a specimen, its scattering intensity fluctuates over time due to Brownian motions.[60] Namely, the larger the particles studied, the larger the intensity fluctuations observed along with slower times, see Figure 6. The time dependent scattering intensity patterns are auto-correlated after short time intervals, which allows to monitor the decay of correlation.[61] In general, decay time constants, derived from *auto-correlation function (ACF)*, of smaller particles are shorter. One of the commonly applied algorithms for ACF calculations is the *CONTIN* algorithm, which allows to determine the translational diffusion constant D.[62] In the measurement, the temperature T is mostly constant, and the viscosity η is known or can be measured, therefore the *Stokes-Einstein equation* can be used to determine the hydrodynamic radius r_h of a particle:[61]

$$D = \frac{k_B T}{6\pi r_h} \qquad (15).$$

Where $k_B = 1{,}380648 \cdot 10^{-23}\,J/K$ is the *Boltzmann constant*.

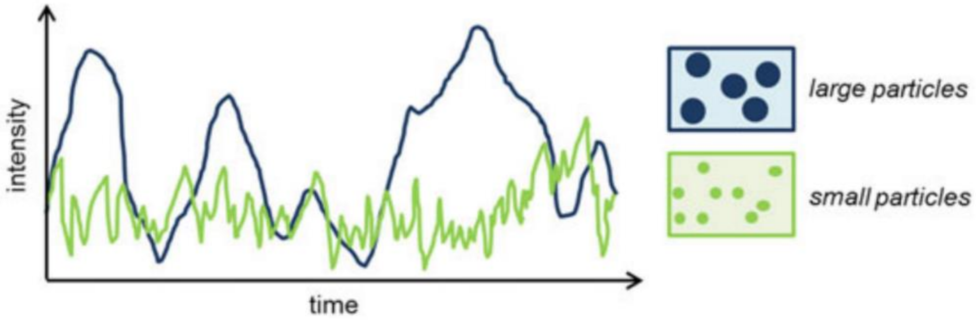

Fig. 6. Generalization of dependence on the signal of scattered light of particles of different size. Reprinted from [61].

The DLS arrangement is significantly simpler and much less costly compared to SEM or TEM (see section 4.2.2), nevertheless in DLS it is most of the time assumed that each particle is spherical, which is not always true for gold nanoparticles. Moreover, the DLS measurement is conducted in solution, which often does not require any specific sample preparation. However, there are also significant limitations, such as sample sedimentation, more likely to occur with dense specimen.[63] Furthermore, if the nanoparticles are spaced relatively close to each other, i.e. in a distance lower than 3 times the difference in size between them, the size distribution will not be precise due to interparticle interactions.[64] Last but not least, as DLS is basing on light scattering, it cannot be excluded that a photon was scattered on a second particle before reaching the detector, which is called *multiple scattering*.[65]

4.3 Nanoplasmonics

Since the gold nanoparticles owe their optical properties, which are of concern in this study, to their plasmonic properties, in particular to their Localized Surface Plasmon Resonance, it is crucial to grasp the fundamentals of nanoplasmonics, presented in this chapter.

In order to understand the principles of nanoplasmonics, let us admit the definition of a plasmon. It is described as a "quantum of energy associated with an eigenfrequency of a plasma oscillation", where plasma shall be understood as an electron gas with electric charges free to move within an ionic background in presence of electromagnetic forces[66]. Surface plasmon resonance (SPR) is a phenomenon, where irradiating a thin metal layer induces movement of electrons in the vicinity of the surface of the layer propagating parallel to the metal surface, i.e. a plasmon is induced[67]. This method is nowadays widely applied to study molecule interactions[68], applying the Kretschmann geometry, where attenuated total reflection (ATR) method is used. Namely, the resonance occurs at a specific incident wavelength and is highly sensitive to any refractive index changes close to the metallic film. The so-called "dark zone", where no reflection is observed, is then moved[69].

In the case of metallic nano-objects, a Localized Surface Plasmon Resonance (LSPR) is an oscillation of conduction electrons. The metallic nanoparticles may exhibit resonance behaviour at certain frequencies if their dielectric permittivity is negative and their dimensions are small compared to the free-space wavelength[70]. Since the electrons may only move within the internal metal framework, collective electron charge oscillations occur, which leads to absorbance of electromagnetic waves within specific bands[71]. The nature of these phenomena will be discussed in detail below.

One of the earliest studies regarding behaviour of metallic nanoobjects was conducted by Maxwell Garnett in 1904[72]. Namely, he introduced a physical quantity connecting absorption and refraction:

$$N = n(1 - i\kappa) \tag{6},$$

where n is the coefficient of refraction and κ refers to the coefficient of absorption. Here, $i = \sqrt{-1}$. The N quantity was not given a name, however considering passage of light through a dielectric medium containing many small metallic particles, he was able to account for some of the observed features[73].

Note the similarity to the current definition of complex refractive index[74]:

$$n_{complex} = n + i\kappa \tag{7}.$$

An approach to describe the interaction of metallic nanoparticles with electromagnetic wave is the quasi-static approximation[75]. Assuming the particle's size much smaller than the propagating wavelength $(d \ll \lambda)$, the phase of the oscillating electromagnetic field remains constant over the particle diameter. For a homogenous isotropic sphere of radius a, the polarizability α thus reads as:

$$\alpha = 4\pi a^3 \frac{\varepsilon-\varepsilon_m}{\varepsilon+\varepsilon_m} \qquad (8),$$

where ε stands for the dielectric response of the sphere (a complex quantity) and ε_m is the dielectric constant of non-absorbing isotropic surrounding medium. Note that the defined polarizability is a complex value.

If the environment medium dielectric constant can be considered close to constant, the metal one can be modelled with the Drude free electron gas model :

$$\varepsilon(\omega) = 1 - \frac{\omega_p^2}{\omega^2+i\gamma\omega} \qquad (9),$$

where $\omega_p^2 = \frac{ne^2}{\varepsilon_0 m}$ is the plasma frequency of the free electron gas, γ the collision frequency, an inverse of the relaxation time of the free electron gas. In a standard way, e stands for the electron charge, m the electron mass and ε_0 the dielectric constant in vacuum. Equation (9) may be also addressed in terms of AC conductivity σ:

$$\varepsilon(\omega) = 1 + \frac{i\sigma(\omega)}{\varepsilon_0\omega} \qquad (10).$$

Note that the Drude model is not specific to metallic nanoparticles and is also an approximation. Johnson and Christy[76] measured the dielectric constant for silver in particular, which then applied to the Drude model (eq. (9)), shows that in resonance conditions the dielectric constant of silver at a certain frequency ω meets:

$$Re\,[\varepsilon(\omega)] = -2\varepsilon_m \qquad (11),$$

called *Fröhlich condition*. The associated mode is named the *dipole surface plasmon* mode of a metallic nanoparticle due to the dipolar oscillation of the conduction band electrons associated with this condition. Considering Riccati-Bessel functions and following Bohren and Huffman,[77] it can be shown that equation (11) is in fact true for plasmonic (metallic) nanoparticles, including gold.[78-79] Moreover, for a Drude metal in air the *Fröhlich condition* is fulfilled at the frequency $\omega_0 = \omega_p/\sqrt{3}$.

Relaxing the assumption of spherical nanoparticles, assuming an ellipsoidal shape of nanoparticles with semi-axes $a_1 \leq a_2 \leq a_3$ for a surface shape equation[77]:

$$\frac{x^2}{a_1^2} + \frac{y^2}{a_2^2} + \frac{z^2}{a_3^2} = 1 \qquad (12),$$

Bohren and Huffman obtained the polarizability α_i along principal axes (i=1,2,3):

$$\alpha_i = 4\pi a_1 a_2 a_3 \frac{\varepsilon(\omega)-\varepsilon_m}{3\varepsilon_m+3L_i(\varepsilon(\omega)-\varepsilon_m)} \tag{13}$$

with geometrical factor L_i defined as:

$$L_i = \frac{a_1 a_2 a_3}{2}\int_0^\infty \frac{dq}{(a_i^2+q)f(q)} \tag{14},$$

where $f(q) = \sqrt{(q + a_1^2)(q + a_2^2)(q + a_3^2)}$. $\sum L_i$ =1, meanwhile for a sphere $L_1 = L_2 = L_3 = \frac{1}{3}$.

The quasi-static approximation assumes vanishingly small spherical nanoparticles, providing relevant results in calculations performed for spherical or ellipsoidal nanoparticles irradiated by visible or near-infrared light. Particles of larger dimensions exhibit significant phase changes of the driving field over a particle, therefore an electrodynamic approach is required. In 1908 Gustav Mie published a paper describing an electromagnetic theory of a rigorous solution for the diffraction of light by a homogenous sphere of any size or composition, immersed in a homogenous medium[80]. In fact, it applies to sets of independent nanoparticles where no coherent phase relationships between light scattered by each particle occurs. This is valid if the nanoparticles are randomly distributed and separated from one another by large distances, compared to the wavelength[73]. Mie's theory concerns finding the solution of Maxwell's equations describing the field stemming from a plane monochromatic wave over a spherical surface, meanwhile the medium properties change precipitously. It provides an exact analytical characterization of the LSPR, where multipolar eigenmodes of the spherical nanoparticles are revealed. Meanwhile, the expansion of the exciting electromagnetic field to vector spherical harmonic functions provides the excitation strength[81].

Mie theory has been further applied for larger spherical particles of volume V[75, 82-83]:

$$\alpha = \frac{1-0{,}1\cdot(\varepsilon+\varepsilon_m)x^2+O(x^4)}{\left(\frac{1}{3}+\frac{\varepsilon_m}{\varepsilon-\varepsilon_m}\right)-\frac{1}{30}(\varepsilon+10\varepsilon_m)x^2-i\frac{4\pi^2\varepsilon_m^{1.5}}{3}\frac{V}{\lambda_0^3}+O(x^4)}V \tag{15}.$$

$x = \pi a/\lambda_0$ stands for the *size parameter* with λ_0 the wavelength in vacuum. The second part of the denominator is associated with energy shifts connected with retardation. This expression may be expanded to higher order corrections, here briefly noted as $O(x^4)$. Furthermore, the quadratic term in the denominator is responsible for energy shifts caused by the *depolarization field*[82].

Equation (15) can be generalized to an ellipsoidal object:

$$\alpha = \frac{V}{\left(L+\frac{\varepsilon_m}{\varepsilon-\varepsilon_m}\right)-A\varepsilon_m x^2+B\varepsilon_m x^4-i\frac{4\pi^2\varepsilon_m^{1.5}}{3}\frac{V}{\lambda_0^3}} \tag{16}$$

with parameters A and B dependent on the material and its morphology.

An example of an observable, namely extinction, may be well modelled by Mie theory, as was shown for instance by Burrows[84], using the formula for the angular dependence of the scattered complex electric fields[77]:

$$E_\theta \approx E_0 \frac{e^{ikr}}{-ikr} sin\varphi \sum_z \frac{2z+1}{z(z+1)} (a_n \frac{P_n^1}{sin\theta} + b_n \frac{dP_n^1}{d\theta}) \quad (17)$$

$$E_\varphi \approx -E_0 \frac{e^{ikr}}{-ikr} cos\varphi \sum_z \frac{2z+1}{z(z+1)} (a_n \frac{P_n^1}{sin\theta} + b_n \frac{dP_n^1}{d\theta}) \quad (18)$$

With k the wavevector, φ and θ the azimuthal and polar scattering angles, respectively. E_0 represents the strength of the incident field, z the degree of the mode (dipolar mode: $z=1$, octupolar mode $z=2$, etc.). P_n^1 stands for the set of associated Legendre polynomials of genre 1, meanwhile a_n and b_n are complex Mie coefficients, obtained by evaluating the overlap integral between the incident field and the field associated with the natural modes of the system.

For other shapes several numerical methods have been reported. The Discrete Dipole Approximation (DDA) approach is based on the discretization of the nanoparticle volume with polarizabile dipoles[66, 85]. Meanwhile, the Finite Difference Time Domain (FDTD) discretises Maxwell's curl equations over time and space[66, 86]. Other well-developed methods are the Finite Element Method (FEM)[87-88] or the Surface Integral Method (SIM)[89].

Metallic nanoparticles exhibit unique optical properties thanks to the LSPR. Mostly gold[90-92] and silver[93-95] nanoparticles are met in applications, however copper[96-97] or platinum[98-99] are also recorded in the literature[100]. Other metals exhibit optical properties in the UV or far IR range, which makes them less suitable. Gold is often favoured due to better stability, moreover their optical properties are more in line with the biological window with deep tissue penetration (see Fig. 7 and 8), which is advantageous for *in-vivo* biological applications[101-102].

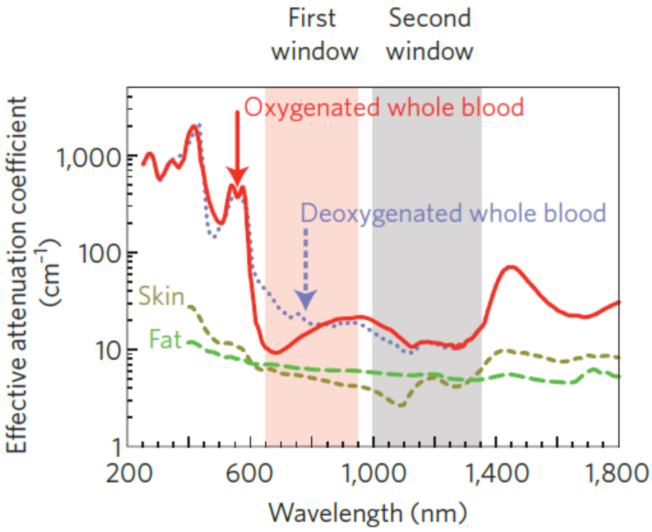

Fig. 7. Effective attenuation coefficient in respect of wavelength for biological tissues with biological windows marked. Reprinted from [101].

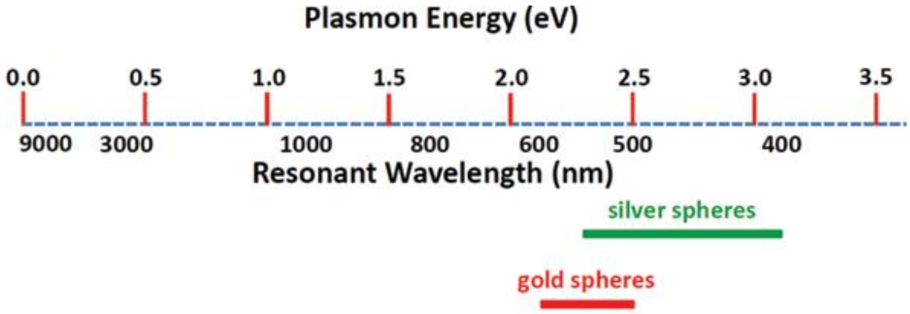

Fig. 8. Comparison of plasmon resonance wavelength of silver and gold nanoparticles. The exact spectrum depends on the nanoparticle size. Reprinted from [103].

The biological window can be also approached by use of nanoparticles of anisotropic shape. Nanoparticles of various anisotropic shapes have been described, including rods[104], bipyramids[21], triangles[23], stars[25], popcorn[28] or cages[27]. Their fabrication has been described in Chapter 4.1.1, see also Figure 2a-g for exemplary TEM pictures.

Optical properties of gold nanoparticles are as well dependent on multiple factors, such as refractive index of the surrounding medium[105]. O. Pluchery showed that the plasmon peak wavelength of spherical particles, calculated by the electrostatic model, shifts from 504 nm in air, to 519 nm or 678 nm in titanium dioxide[66]. Moreover, a shift of the LSPR peak has also been observed in the case of different stabilizing agents[106], which in fact affects as well the nanoparticle's morphology. Interestingly, gold nanoparticles' LSPR is sensitive to compounds appearing in their vicinity, attracted by their surface or stabilizing agent[107]. As a result, gold nanoparticles-based sensing is a field in rapid expansion.

Energy absorbed during photon absorption process in a gold nanoparticle may be transferred into a radiative or a non-radiative process[108], including photoluminescence PL (defined as light emission following absorption of a photon) or thermal processes. PL from bulk gold was first reported in 1969 by Mooradian[109], where Fermi energy of 2.2 eV and Quantum Yield (QD) of the order of 10^{-10} was observed[108]. 14 years later it was followed by a demonstration of LSPR-enhanced PL[110]. The explanation of this phenomenon remains unclear, nevertheless two approaches are known in the literature: the first model relies on an energy transfer from an electron-hole pair, which effects in plasmon excitation followed by a photon emission. On the other hand, a different model asserts an antenna effect, where the internal field enhancement is induced by plasmons, meanwhile the PL is caused by a three-step process associated with non-radiative loss of energy of hot electrons, which is then interconverted to the LSPR and photon emission[108, 111].

4.4. Nonlinear optics

The main focus of this thesis is the Hyper Rayleigh Scattering method applications for sensing purposes. This chapter is dedicated to the basics of nonlinear optics, the comparison to linear optics, with a Subchapter 4.4.1 focusing on Hyper Rayleigh Scattering itself.

In linear optics, following rules must be fulfilled for irradiation or absorption:[112]

- Refractive index and absorption coefficient of a material do not depend on the light intensity.
- The superposition principle is applicable.
- The light frequency cannot be altered after its passage through a medium (unless an absorption process is followed by emission).
- Two separate beams of light do not affect each other, i.e. a beam cannot be used to control another beam of light.

If a medium is irradiated by a laser of high power density, namely $\gg 100\ W/cm^2$, linear optics descriptions appear to be insufficient, however some exceptional scenarios must be kept in mind, i.e. in the case of quantum dots this may happen already during interaction with single photons (the quantum dots are coupled to a propagating mode, thus each photon interacts with the dot, resulting in creation of highly-correlated photons).[113-114] This has also been discussed in theory for graphene-based plasmonics, however it has not been confirmed experimentally due to technical limitations, i.e. lack of single-photon detectors in the range between 2 and 10 µm wavelength.[115]

The polarization vector exhibits the following relation with electric field strength of higher orders:[116]

$$\boldsymbol{P} = \varepsilon_0(\chi^{(1)}\boldsymbol{E} + \chi^{(2)}\boldsymbol{E}^2 + \chi^{(3)}\boldsymbol{E}^3 + \cdots) \qquad (19).$$

$\chi^{(1)}$ is the *linear optical susceptibility*, meanwhile $\chi^{(n)}$ is called *nonlinear optical susceptibility of n-th-order* and is associated with *n-th-order nonlinear optical processes*. ε_0 expresses the free-space permittivity. In linear optics, all components of Equation (19), apart from the first one, are neglectable, then $\boldsymbol{P} = \varepsilon_0\chi^{(1)}\boldsymbol{E}.$ Thus, Equation (19) may be as well written as $\boldsymbol{P} = \boldsymbol{P_L} + \boldsymbol{P_{NL}}$, where $\boldsymbol{P_L} = \varepsilon_0\chi^{(1)}\boldsymbol{E}$ is the linear and $\boldsymbol{P_{NL}} = \varepsilon_0(\chi^{(2)}\boldsymbol{E}^2 + \chi^{(3)}\boldsymbol{E}^3 + \cdots)$ the nonlinear polarization vectors. The wave equation in nonlinear optical media has the form:

$$\nabla^2\boldsymbol{E} - \frac{n^2}{c^2}\frac{\partial^2\boldsymbol{E}}{\partial t^2} = \frac{1}{c^2}\frac{\partial^2\boldsymbol{P_{NL}}}{\partial t^2} \qquad (20).$$

In equation (20) *n* is the classical linear refractive index, *c* is the speed of light in vacuum. $\partial^2\boldsymbol{P_{NL}}/\partial t^2$ shall be understood as a measure of acceleration of charges constituting the medium, which is consistent with electromagnetic Larmor's theorem, stating that electromagnetic radiation is created by acceleration of charges.

Various mechanisms inducing nonlinear polarization in a medium have been reported:[117]

- Electron-cloud distortion.
- Intramolecular motion.
- Molecular reorientation.
- Induced acoustic motion.
- Induced population change.

The first mechanism, i.e. electron-cloud distortion, is mostly met and can contribute to any kind of nonlinear optical processes and be present in various media. Furthermore, its response is extremely rapid, i.e. 10^{-15}-10^{-16} s as it involves electrons.

Let us consider second order nonlinear optical processes, where

$$\boldsymbol{P} = \varepsilon_0 \chi^{(2)} \boldsymbol{E^2} \tag{21}$$

In the simplest case (solely in terms of mathematical considerations), the laser beam electric field may be expressed as:

$$\boldsymbol{E(t)} = E e^{-i\omega t} + c.c. \tag{22}$$

With *c.c.=complex conjugate.* The nonlinear optics processes occur however often under influence of two distinct electromagnetic wave beams, thus let us consider a medium consisting of two distinct frequency components, namely:[116]

$$\boldsymbol{E(t)} = E_1 e^{-i\omega_1 t} + E_2 e^{-i\omega_2 t} + c.c. \tag{23}$$

Note, that if $E_1 = E_2$, Equation (23) takes the form of Equation (22), where the interacting photons are of equal nature.

From Equations (21) and (23) we have:

$$\boldsymbol{P}(t) = \varepsilon_0 \chi^{(2)} \big(E_1^2 e^{-2i\omega_1 t} + E_2^2 e^{-2i\omega_2 t} + 2E_1 E_2 e^{-i(\omega_1+\omega_2)t} + 2E_1 E_2^* e^{-i(\omega_1-\omega_2)t} + c.c. \big) + 2\varepsilon_0 \chi^{(2)} (E_1 E_1^* + E_2 E_2^*) \tag{24}$$

Equation (24) can be expressed using different notation:

$$\boldsymbol{P}(t) = \textstyle\sum_n P(\omega_n) e^{-i\omega_n t} \tag{25}$$

Thus, 5 relations of complex amplitudes of frequency components can be observed:

$$P(2\omega_1) = \varepsilon_0 \chi^{(2)} E_1^2 \tag{26a}$$

$$P(2\omega_2) = \varepsilon_0 \chi^{(2)} E_2^2 \tag{26b}$$

$$P(\omega_1 + \omega_2) = 2\varepsilon_0 \chi^{(2)} E_1 E_2 \tag{26c}$$

$$P(\omega_1 - \omega_2) = 2\varepsilon_0 \chi^{(2)} E_1 E_2^* \tag{26d}$$

$$P(0) = 2\varepsilon_0\chi^{(2)}(E_1E_1^* + E_2E_2^*) \qquad (26e).$$

Each Equation (26) describes a physical process: (26a) and (26b) *Second Harmonic Generation (SHG)*, (26c) *Sum-Frequency Generation (SFG)*, (26d) *Difference-Frequency Generation (DFG)* and (26e) *Optical Rectification (OR).*

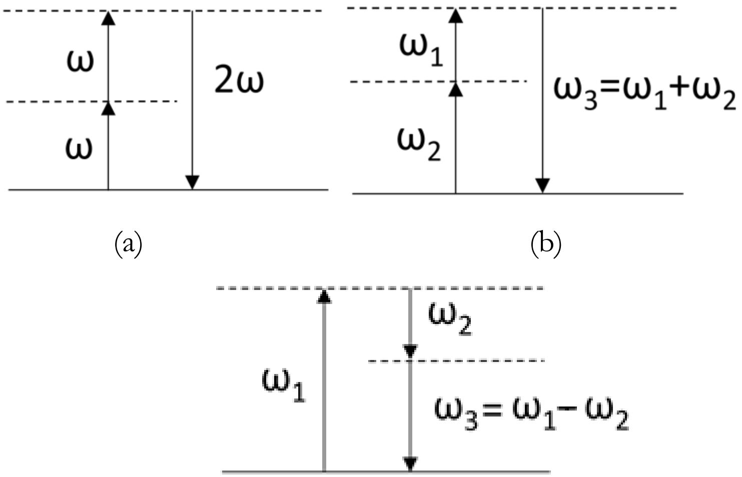

(a) (b)

(c)

Fig. 9. Depiction of energy levels in SHG (a), SFG (b) and DFG (c) processes. Dashed lines represent virtual states.

In the case of Second Harmonic Generation, radiation at the second-harmonic frequency is generated, i.e. energy of two identical photons is converted into one photon of doubled energy (see Fig. 9.(a)). Meanwhile, the SFG process is analogous (Fig. 9(b)), however the two input photons involved have different energy. This may be realised by usage of two different light sources of different wavelengths. In case of DFG, the outcoming photon ω_3 has energy being the difference of energies of the two incoming photons (Fig. 9(c)). Furthermore, Optical Rectification is not connected with electromagnetic radiation absorption or emission; namely, it is a creation of a static electric field across a nonlinear crystal that occurs. The primary trespassing electromagnetic wave remains unaffected as well.

Many applications of nonlinear optics arise from breakage of the rules mentioned in the beginning of this chapter. Namely, in the non-linear optical regime:[112]

- The refractive index depends on the light intensity.
- The superposition principle is not valid.
- The frequency of light changes after passing through a medium, compare with Figure 6.

- A light beam may be used to control another light beam, since they can interact.

Moreover, note that in the case of nonlinear optical processes virtual states are involved, thus the Laporte rule is not conserved in the case of multiphoton absorption.[118] According to the Laporte rule, if an absorption phenomenon shall happen, the parity, i.e. the symmetry of the wave function, must not be conserved. In other words, absorption is possible only with parity change,[119] whereas in the case of multiphoton absorption, the parity may be conserved, i.e. it may be an odd to odd or even to even transition.[120]

4.4.1. Role of the symmetry centre

Note that in the case of eq. (21), $\boldsymbol{P}$ must change its sign when the applied field $\boldsymbol{E}$ changes its sign. However, if a medium is centrosymmetric and the two field components change their sign (compare with eq. (23) or eq. (24)), the right side remains unchanged, namely:[121]

$$-\boldsymbol{P} = \varepsilon_0 \chi^{(2)} (-\boldsymbol{E})(-\boldsymbol{E}) \qquad (27).$$

This is true if $\chi^{(2)} = 0$. This leads to the conclusion that Second Harmonic Generation, a second-order nonlinear optical process, cannot occur in compounds possessing a symmetry centre[122]. Nevertheless, Epperlein showed in 1987[123] that since:

$$\boldsymbol{E} = \hat{E} e^{i(\omega t - \boldsymbol{kr})} \qquad (28),$$

the Nabla ∇ operator works on both the amplitude and phase:

$$\nabla \boldsymbol{E} = \left[\left(\nabla \hat{E} - i \left(\boldsymbol{k} \hat{E} \right) \right) \right] \cdot e^{i(\omega t - \boldsymbol{kr})} \qquad (29).$$

k stands for the wavenumber. Considering a lossless wave propagation in a transparent bulk medium, the first term of Equation (29) vanishes for bulk, but it remains non-zero at the surface of a compound. Thus, Second Harmonic Generation may be also observed in centrosymmetric media, i.e. in fact stemming from their surface.

Interestingly, a different approach where SHG may be observed in centrosymmetric media is breaking the symmetry at interfaces. Nowadays S-SHG (Surface Second Harmonic Scattering) is widely applied in study of interfaces.[124]

4.4.2. Hyper Rayleigh Scattering: First hyperpolarizability

Chapter 4.4. was dedicated to a general introduction to nonlinear optics, whereas this thesis is focusing on the Hyper Rayleigh Scattering, which applies the incoherent Second Harmonic Generation (in other words: Second Harmonic Scattering) phenomenon, thus this subchapter will describe the SHG and HRS in more detail.

It must be however admitted that the name *Hyper Rayleigh Scattering* has been also recently used to refer to the *Chiroptical harmonic scattering,*[125] which is a different phenomenon, and it can cause confusion if the HRS term is used without context, as HRS is not involving a chiroptical phenomenon per se.

In Cartesian tensor notation, for a single molecule the induced dipole moment is:[126]

$$\mu_i = \alpha_{ij}E_j + \beta_{ijk}E_jE_k + \gamma_{ijkl}E_jE_kE_l + \cdots \qquad (30),$$

where μ_i is the induced dipole moment component, along the molecule-fixed *i* axis. α, β, γ, … are components of the polarizability tensor of the first, second, third, etc. order, respectively. β is often called the first hyperpolarizability, γ the second hyperpolarizability, etc… and *i, j, k, l* represent the corresponding frame axes. The polarizability tensors of each order are associated with nonlinear optical processes of corresponding order. One of the methods to determine the first hyperpolarizability value is Hyper Rayleigh Scattering (HRS), see Figure 10. If an aqueous sample is excited by a femtosecond laser and its Second Harmonic signal is recorded:[127]

$$I \propto (N_P < \beta_p^2 > + N_s < \beta_s^2 >) \qquad (31).$$

In equation (31), N_s *and* N_p are particles number per unit volume for the solvent (water) and particles (the studied component), respectively, and *I* the HRS signal. <> expresses the averaging over orientation of molecules. If the signal *I* is normalized to solvent signal, equation (31) can be expressed as:

$$\frac{I}{I_s} = 1 + \frac{N_p<\beta_p^2>}{N_s<\beta_s^2>} \qquad (32).$$

For water $\sqrt{<\beta_s^2>} = 0.087 \cdot 10^{-30} esu$.[128] It must be however noted that in older publications, the value $\sqrt{<\beta_s^2>} = 0.56 \cdot 10^{-30} esu$ [129] was taken for calculations. The new reference was obtained by J. Duboisset et al.,[128] where chloroform with $\sqrt{<\beta^2>} = 0.55 \cdot 10^{-30} esu$ [130] was used as reference for the first hyperpolarizability value of water.

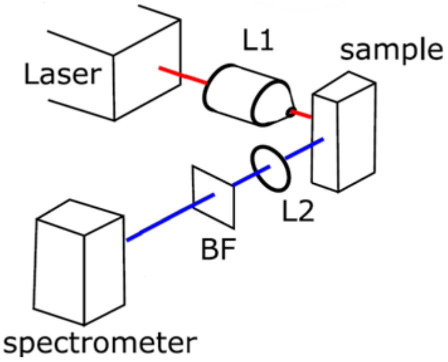

Fig. 10. Scheme of a typical Hyper-Rayleigh Scattering setup. Femtosecond-laser beam focused by a lens (L1) passes through a sample, it is collected in the right-angle regime by a spectrometric device. A filter (BF) is used to not detect direct laser beam in the detector. This picture is drawn, basing on the actual set-up used for experiments, further described in Chapter 5.

4.4.2.1. Polarization analysis

To investigate the origin of HRS signal, polarization-resolved measurements can be performed.[131] In the dipole approximation, SHG is a forbidden process in centrosymmetric media. As has been already discussed in Chapter 4.4.2, SHG signal may be observed at the surface of centrosymmetric compounds. Furthermore, E. Adler has first described and J. I. Dadap further developed a theory for description of multipole expansion.[132] Namely, the Hyper Rayleigh Scattering signal is shown to arise from nonlocal excitation of an electric-dipole moment and an electric-quadrupole (or, more generally speaking, electric-multipole) moment. In terms of local coordinate system, the signal polarized in the direction of parallel (vertical, V) axis exhibits either two lobes, as shown in Fig. 12(a), associated with dipolar response, or four lobes associated with a quadrupolar contribution (see Fig. 12(b)). See Figure 11 for a depiction of experiment geometry, where Z is the direction of incident beam propagation. J. Butet also described the response when the signal is collected perpendicularly to the incident beam (horizontal polarization, H).[133] It allows to monitor retardation of higher order. Thus, if no retardation is noted, the graph is a circle (Fig. 13(a)), i.e. the signal in all directions remains constant. If the signal retardation plays a significant role, the circle transforms into an ellipse (Fig. 13(b)). For a more quantified understanding please see further paragraphs.

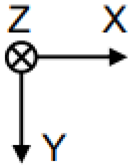

Fig. 11. A depiction of experiment geometry, where the beam is propagated along the Z axis, meanwhile X and Y correspond to the vertical and horizontal polarization plane, respectively.[134]

The polarization-resolved data can be fitted with classical polarization dependence at the harmonic frequency:[135]

$$I^X = a^X cos^4\gamma + b^X cos^2\gamma \, sin^2\gamma + c^X sin^4\gamma \qquad (33),$$

where X stands for V or H, namely vertical or horizontal polarization. *a, b* and *c* are fitting parameters and γ is the polarization angle of the incoming light beam. In order to quantify the degree of deviation from dipolar response in vertically-polarized signal, the retardation parameter ζ^V is introduced:[136]

$$\zeta^V = \frac{b^v-(a^v+c^v)}{b^v} \qquad (34).$$

For a retardation-free reponse $b^v = a^v + c^v$, then the ζ^V is equal to 0. In the case of a purely retarded response $a^v = c^v = 0$, thus the retardation parameter equals unity. The values between 0 and 1 indicate the level of retardation. It must be noted however, that this simplified description assumes fully local SHG response. As it was shown by J. Duboisset and P-F. Brevet,[137] if the nano-object spatial extension must be accounted for, nonlocal response shall be also taken into consideration, connected with field retardation. A combined measurement of right angle and forward geometry give full information about the origin of vertically-polarized HRS.[135] This was however not crucial for sensing purposes and was not further studied in detail.

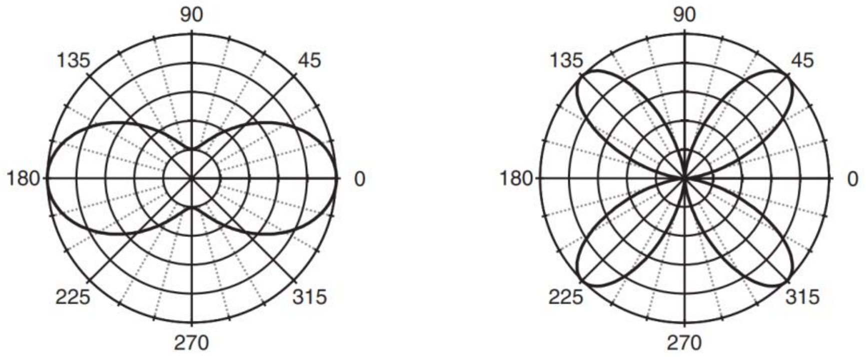

(a) (b)

Fig. 12. Representation of purely dipolar (a) and purely quadrupolar (b) response of vertically-polarized output signal as function of the angle of polarization of the excitation beam.

Reprinted from [138].

If the horizontally-polarized signal exhibits a large retardation, the difference between the highest and the lowest signal is large. Furthermore, a parameter ζ^H can be written as:

$$\zeta^H = \frac{I^H_{max} - I^H_{min}}{I^H_{max} + I^H_{min}} \qquad (35)$$

with I^H_{max} and I^H_{min} the highest and the lowest signal values, respectively. Nevertheless, this may be significantly disturbed if the experiment shows high noise, therefore it may appear to be more appropriate to perform the fitting procedure, as in Equation (33) and use the following form of Equation (35):

$$\zeta^H = \frac{a^H - c^H}{a^H + c^H} \qquad (36),$$

If no dependence of the signal value on incident beam polarization angle is noted, i.e. the polarization graph is a circle (as in Fig. 13(a)), $2a^H = 2c^H = b^H$, hence $\zeta^H=0$, no retardation is observed. In case of a deviation, an ellipsoid instead of a circle is observed, as in Figure 13 (b).

An additional parameter, called the depolarization ratio, namely:[135]

$$D^V = \frac{c^V}{a^v} \qquad (37)$$

informs about the symmetry of the compound. For instance, under Kleinmann approximation, where no strong resonances appear and dispersion may be neglected, for a single-tensor-element β_{zzz} point-like onefold system the depolarization ratio is equal to 0.2,[139-140] meanwhile for a point-like threefold planar geometry a value of 2/3 is expected.

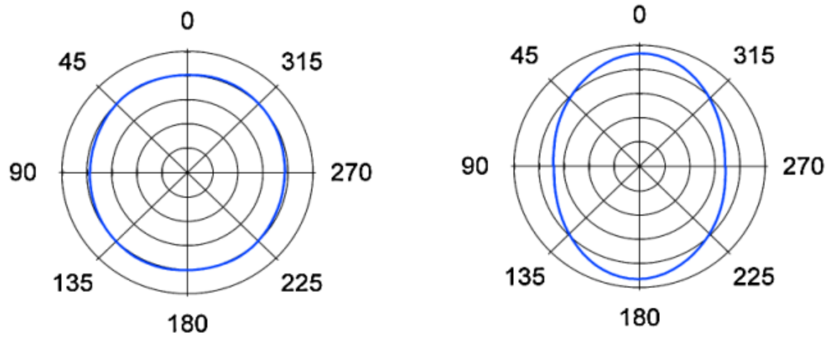

(a) (b)

Fig. 13. Theoretical curves of horizontally-polarized output signal as a function of the polarization angle of the excitation beam for 50 nm (a) and 100 nm (b) mean diameter gold nanoparticles. Reprinted from [133].

4.4.3. HRS of metallic nanoparticles

The Hyper Rayleigh Scattering of metallic nanoparticles has been widely described. One of the first studies of HRS at a metal spherical surface of radius small compared to the excitation wavelength was theoretically performed in 1982.[141] Namely, G.S. Agarwal demonstrated that in conditions of surface-plasmon-polariton resonance, the surface response dominates over the bulk effects, which was previously experimentally shown by Chen.[142] The first hyperpolarizability of metallic nanoparticles was studied by Hao[143] for spherical silver nanoparticles of radius $32 \pm 6\ nm$ with excitation wavelength 820 nm, keeping in mind that contradictory to what was mentioned in the section 4.4.2., the water first hyperpolarizability value was assumed to be $0.56 \cdot 10^{-30}\ esu.$[144] It was also used in other studies published before 2010, when the value of $0.087 \cdot 10^{-30}\ esu$ was reported.[128] Note, that since the first hyperpolarizability of a compound is proportional to the first hyperpolarizability of water (or another solvent), see Eq. (32), the values obtained before 2010 should be divided by, approximately, 6.44 (0.56/0.087). The first hyperpolarizability measured in function of the incident wavelength shows two maxima at around 780 and 820 nm (see Fig. 14). It is compared with the Differential Sediment Entrainment Hypothesis DSEH theory, for which the signal stems from emission by an induced dipole at the harmonic wavelength 2ω, as well as from an induced quadrupole, which corresponds to the two peaks.

First hyperpolarizabilities of gold and silver spherical nanoparticles of size varying from 10 to 150 nm were later reported by I. Russier-Antoine et al.,[131] see Figure 15. They were obtained for 780 nm fundamental beam wavelength in the case of silver and 800 nm for gold nanoparticles. The bigger magnitude for silver may be attributed to different spectral localisation of the LSPR peak, namely closer to the harmonic wavelength. Moreover, the behaviour of studied nanoparticles was attributed to surface or bulk effects in gold and silver, respectively, which is in good agreement with the LSPR peak influence, since this effect scales with volume (i.e. the closer localization of the LSPR peak results in more significant bulk effects contribution).

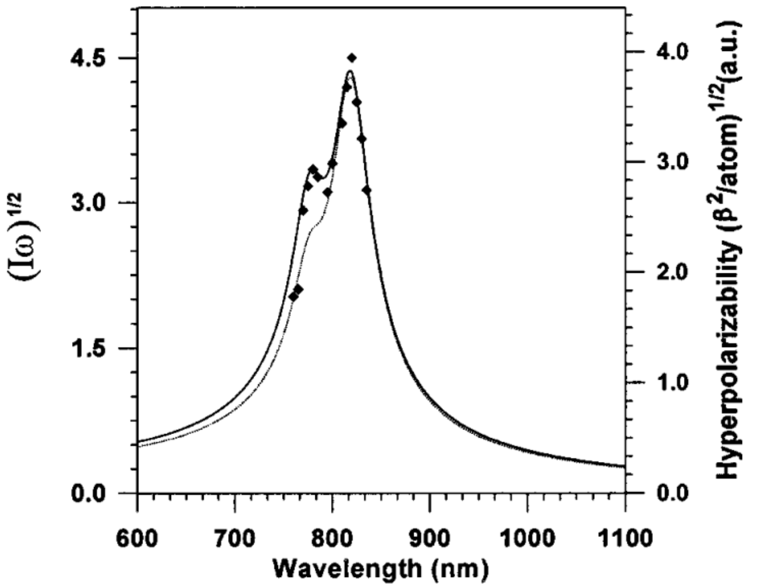

Fig. 14. The first hyperpolarizability of silver spherical nanoparticles as a function of excitation wavelength. Solid squares represent experimental data, the solid line represents theoretical simulation from the Differential Sediment Entrainment Hypothesis (DSEH). Prediction from Agarwal theory[141] is depicted with dashed line. Reprinted from [143].

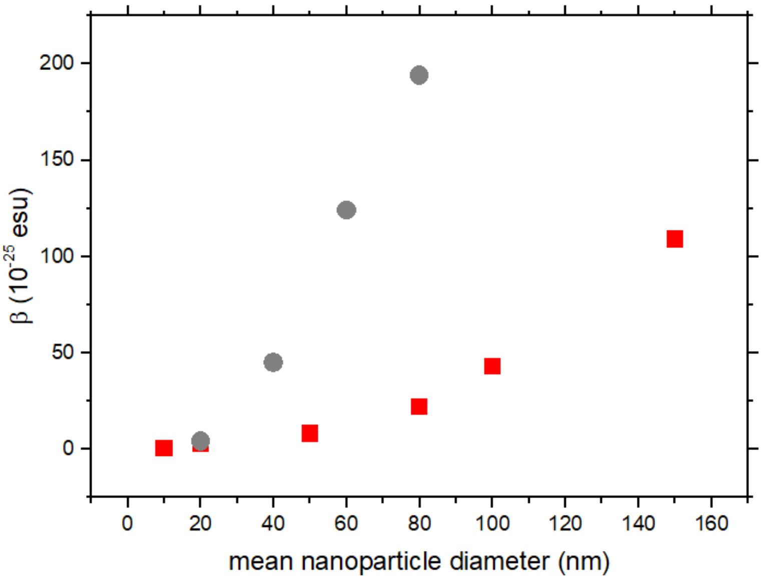

Fig. 15. The first hyperpolarizability as a function of mean nanoparticle diameter for gold (red) and silver (gray) spherical nanoparticles.

The data used to draw the graph was taken from [131] and [135].

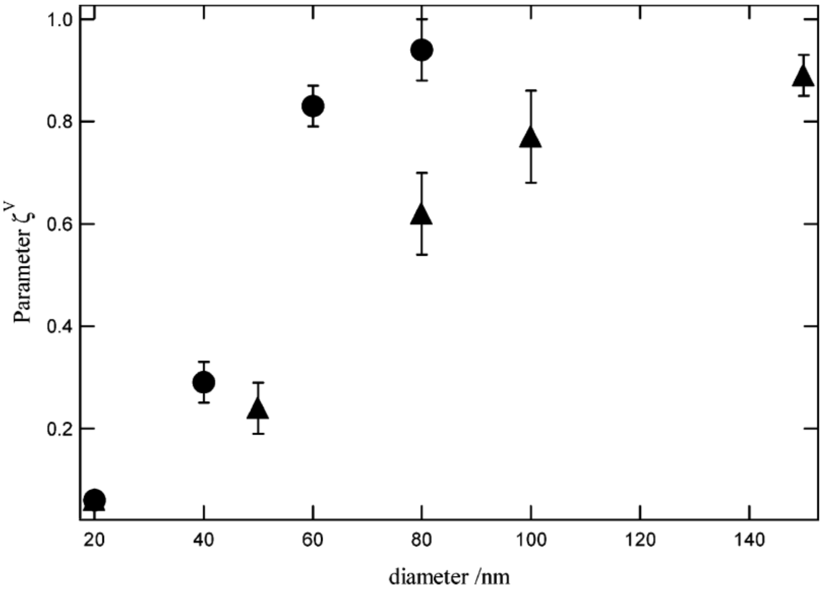

Fig. 16. Signal retardation parameter ζ^V for gold (triangle) and silver (circle) nanospheres of different mean diameter. Reprinted from [131].

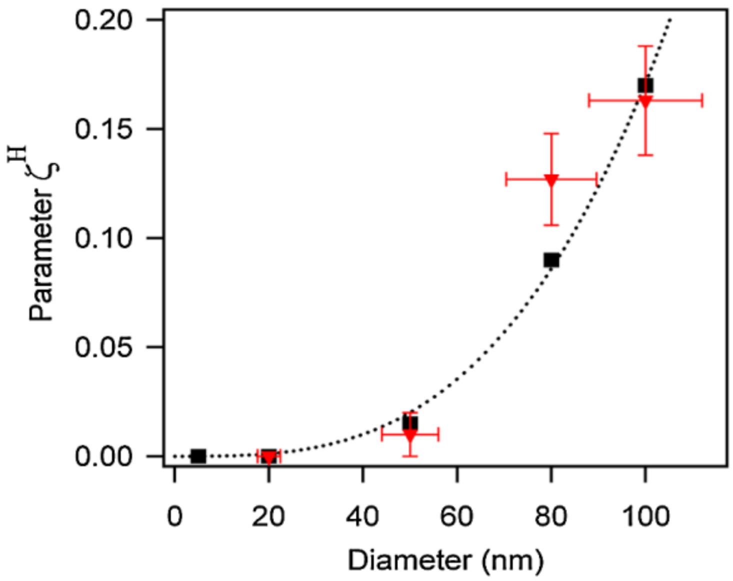

Fig. 17. Retardation parameter ζ^{H} of gold nanoparticles of different mean diameter (red triangles). The black squares correspond to performed simulations. Reprinted from [133].

In the case of polarization-resolved measurements (see Section 4.4.2.1) gold nanoparticles exhibit a significant growth of both retardation parameters, see Figures 16 and 17. Interestingly, silver is more affected by the retardation phenomenon, which is in good agreement with the first hyperpolarizability value scaling with the nanoparticle volume. For an additional confirmation, see Figure 18. The linear plots performed for log-log graphs show slopes around 2 and 3 for gold and silver, respectively.

Furthermore, the response of small nanoparticles, i.e. of mean diameter below 50 nm, is dominated by dipolar contribution, however with size the signal retardation (Fig. 16 and 17) is more significant, whereas around 100 nm the retardation parameter for vertically-polarized signal approaches unity.

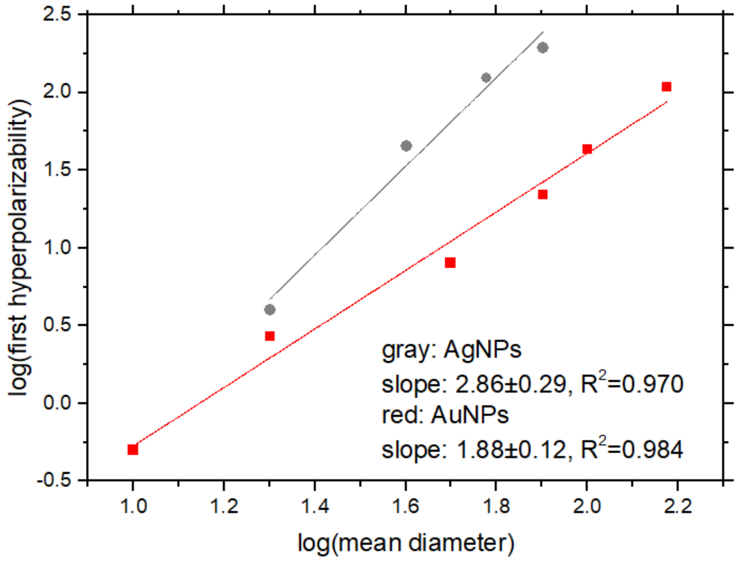

Fig. 18. Figure 15 redrawn in log-log scale, along with linear fits. The slope value confirms scaling with nanoparticles' surface and volume for gold and silver nanoparticles, respectively.

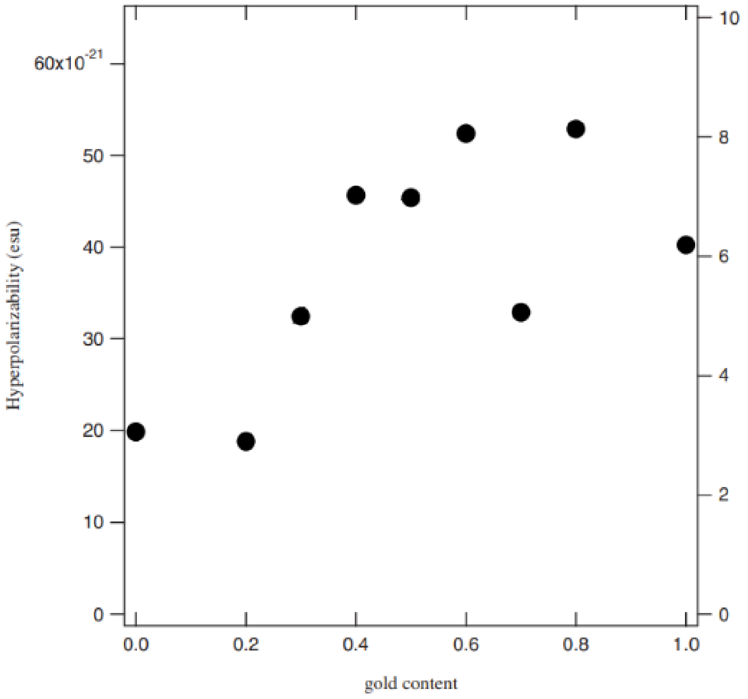

(a)

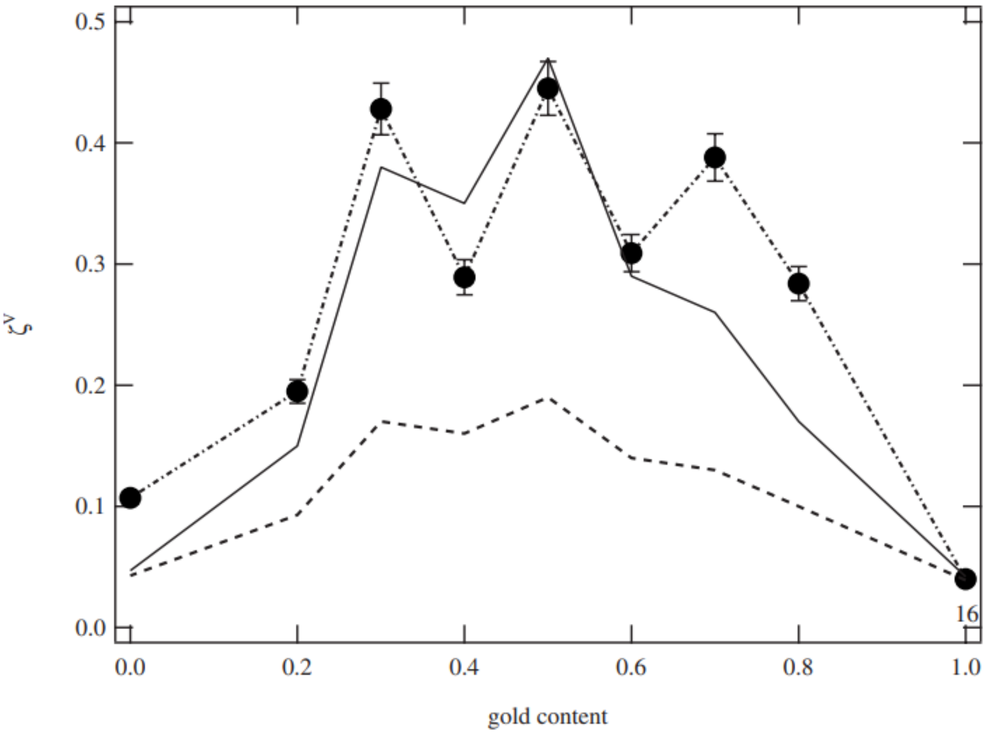

(b)

Fig. 19. First hyperpolarizability value (a) and ζ^V (b) of gold-silver nanoalloyed nanoparticles. The x axis corresponds to fraction of gold in the composition. Reprinted from [138].

A deeper insight into differences between gold and silver HRS properties was provided by study of alloyed nanoparticles.[138] Neither the first hyperpolarizability nor the signal retardation scale linearly with transition from silver to gold (see Fig. 19 (a) and (b)). This anomaly shall be associated with deformations on the nanoparticles' surface, in particular heterogeneity. Thus, the parameter ζ^V is dependent on the signal retardation and specimen deformation, which may be written as $\zeta^V \propto \frac{retardation}{retardation+deformation}$. This is in line with the fact that the highest deviation is observed for equal gold and silver content, where the heterogeneity is the highest. Anisotropic nanoparticles behave differently from isotropic nanospheres. First of all, they may exhibit more than one LSPR mode. What's more, their surface to volume ratio is different. Figure 20 compares exemplary UV-Vis spectra of nanospheres and nanorods. The latter ones exhibit longitudinal (L-) and transverse (T-) LSPR, connected with oscillations along their longer and shorter axes, respectively. This significantly affects nonlinear optical properties: not only is their L-LSPR located close to the typical excitation wavelength in HRS measurements, being usually in the range 700-1000 nm, but their surface-to-volume ratio is remarkably large compared to nanospheres, which may emphasize the surface-based effects. Their first hyperpolarizability value is significantly higher: for CTAB-stabilized nanorods of size 64 x 24 nm it is $8.8 \cdot 10^{-25}\ esu$.[145] Since spheres and rods exhibit different geometry, a *β per atom* approach was proposed. Then, citrate-stabilized nanospheres exhibit $0.17 \cdot 10^{-30}\ esu/atom$ or $0.02 \cdot 10^{-30}\ esu/atom$ in the case of 20 nm or 100 nm mean diameter, respectively. For 64 x 24 nm nanorods this value was reported to be $0.7 \cdot 10^{-30}\ esu/atom$. This may appear contradictory to the higher surface-to-volume ratio, however it was also shown that the stabilizing agent plays an essential role: dodecatheniol- or octadecatheniol nanoparticles owe *β per atom* around 3-10 times lower than CTAB- or citrate-stabilized ones. In the meantime, the CTAB-capped 64 nm x 24 nm nanorods' retardation parameter $\zeta^V = 0.028$, which confirms higher surface contribution than in the nanospheres' case (compare with Figure 12).

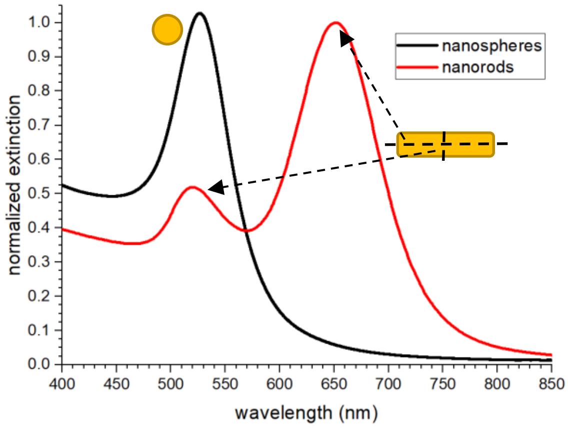

Fig. 20. An example of UV-Vis spectra of nanospheres (black) and nanorods (red), normalized to unity. Nanospheres exhibit one peak, meanwhile nanorods have two characteristic peaks, connected with LSPR towards their longer and shorter axis: longitudinal and transverse mode, respectively. This data was collected in an own study.

In 2018 I. Russier-Antoine et al. published a study on silver nanocubes,[146] where nanoparticles of 39, 48 and 100 nm edge length were investigated. The first hyperpolarizability values were $10.6 \cdot 10^{-25} esu$, $16.6 \cdot 10^{-25} esu$ and $12.8 \cdot 10^{-25} esu$ with the first hyperpolarizability per atom corrected for resonance enhancement: $1.4 \cdot 10^{-32} esu$, $2.7 \cdot 10^{-32} esu$ and $0.6 \cdot 10^{-32} esu$ for 39, 48 and 100 nm edge length, respectively. Here the water first hyperpolarizability value was taken as $0.087 \cdot 10^{-30}\ esu$, however the authors recalculated the first hyperpolarizability per atom of silver nanospheres of 40 and 80 diameter, which were $0.5 \cdot 10^{-32}\ esu/atom$ and $1.4 \cdot 10^{-32}\ esu/atom$, respectively. The resonance enhancement correction was introduced since the nanocubes, contrarily to spheres or rods, do not exhibit discrete peaks in UV-Vis spectra, but rather multiple broad bands. The first hyperpolarizability of cubes and spheres is comparable: in fact the anisotropy is lower than, for instance, of rods. Similarly, the retardation parameters were of the same magnitude like in the case of nanospheres.

HRS of metallic nanoparticles of other metals has also been investigated, including platinum nanoflowers, whose first hyperpolarizability per nanoparticle's magnitude was $\sim 10^{-26}$esu, keeping in mind that the water first hyperpolarizability was assumed to be $0.055 \cdot 10^{-30}\ esu.$ [147] Keeping in mind the latest water hyperpolarizability value of $0.087 \cdot 10^{-30}\ esu$, the platinum nanoflowers' value remains in the 10^{-26} to 10^{-27} magnitude.

The mentioned nanoparticles owe a centre of symmetry, thus the Second Harmonic stems from effects occurring at the nanoparticle's surface (see Section 4.4.1). A pending issue was to investigate non centrosymmetrical nanoparticles. An example of nanoparticles, which do not have a symmetry centre and can be seen as two pyramids of a common pentagonal base, are nanodecahedra, (see Fig. 21).[148] Both the first hyperpolarizability, as well as polarization-resolved measurements showed behaviour similar to the centrosymmetrical nanoparticles. Surprisingly, a symmetry cancellation occurs, which may be also understood in terms of a five-fold symmetry, present in quasicrystallines.[149]

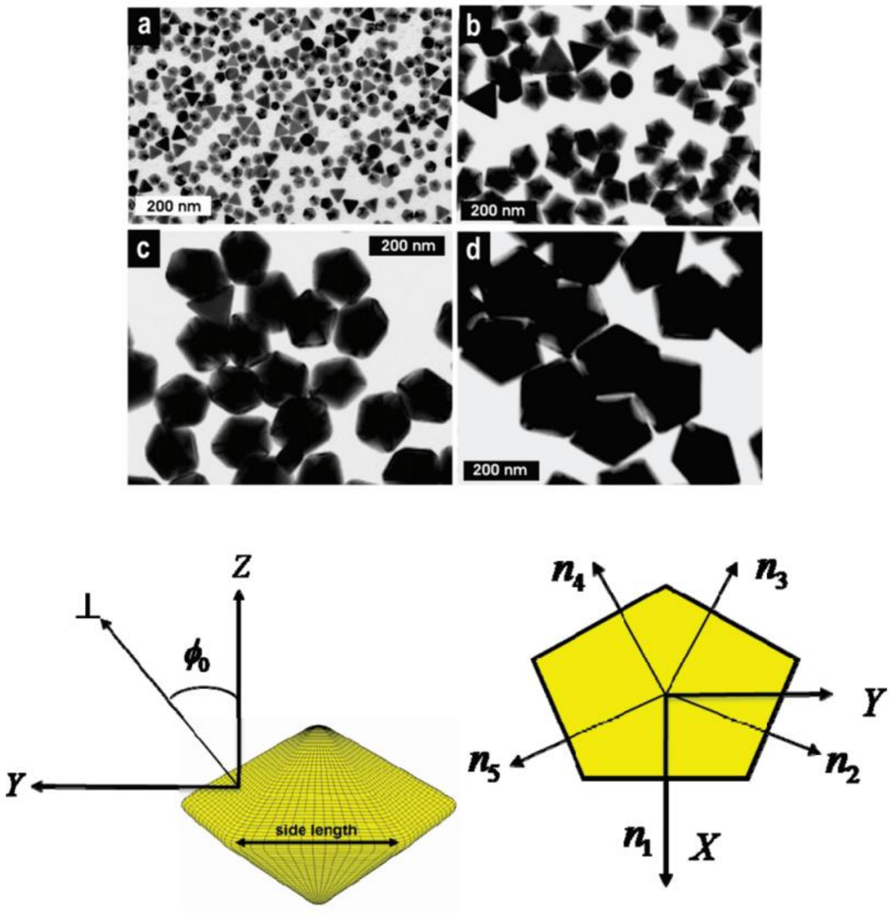

Fig. 21. TEM pictures and schematical representation of gold nanodecahedra. Reprinted from [148].

Furthermore, J. Lyu published a complementary study on monitoring the Hyper Rayleigh Scattering during transition from gold nanotetrapods to nanospheres.[150] Here, the tetrapods exhibited lack of centrosymmetry: the depolarization ratio for nanotetrapods was 0.61, typical for structures of three-fold symmetry with $\zeta^V = 0.01$. With transformation into nanospheres, the retardation parameter increased to 0.33, along with decreased depolarization ratio $D^V = 0.27$. This study is in great compatibility with a study on gold nanotriangles published in 2020 (2 years earlier),[151] which will be discussed in the *Results and discussion* section.

4.5. Applications of gold nanoparticles

This short chapter will introduce the reader to some of the applications of gold nanoparticles, referring also to some historical ones. Since the current thesis rather focuses on some proof of principle, some examples will be briefly mentioned, without providing further details.

Gold nanoparticles may seem to be a novel material, however the oldest known example of their applications is the *Lycurgus Cup* from the 4th century AD, namely a dichroic cup stained with gold and silver nanoparticles, which changes its colour depending on whether reflected or transmitted light is observed,[152] see Figure 38. It is nowadays exhibited at the British Museum. In fact, gold nanoparticles are still used for red glasses production along with copper, since the alternative, cadmium sulfoselenide, is highly toxic.[153-155]

Fig. 38. Lycurgus Cup lit from the front (left) and from behind (right). Reprinted from: https://www.amusingplanet.com/2016/12/lycurgus-cup-piece-of-ancient-roman.html (access: 13.06.2022).

The gold nanoparticles' applications may be divided into multiple groups, depending on the property, which is used.

The first group is applications owing to the chemical properties of gold nanoparticles, as well as their catalytic attributes. AuNPs can act as catalysts for oxidation of alcohols and alkanes,[156] in carbon-carbon coupling reactions[157] or photocatalysis of dehydrogenation of sodium formate.[158] There are multiple theories explaining their catalytic activity, e.g. low-coordinated Au atoms, cationic behaviour of gold or electron transfer from the so-called *F-centres* (holes caused by oxidation).[159] Note that for the catalytic applications, gold nanoparticles of size below 10 nm are used, whereas for optics we will mostly consider bigger ones. Furthermore, gold nanoparticles synthesized from fruit extract *Terminalia arjuna* enhance the seed germination of *Gloriosa superba,*[160] which is an endangered medicinal plant. The presence of

AuNPs ameliorates the permeability of the seed coat, which enables the admission of water and copper dioxide into the cells, which is then responsible for germination and metabolic activity acceleration.

Second group of applications is connected with AuNPs plasmonic properties. Gold nanoparticles can be considered as *plasmonic nanoantenna,* since they allow to transfer the electromagnetic energy from near- to far-field and reverse.[161] Presence of the LSPR gives rise to hotspots, namely localised nanoatenna.[162] Also photovoltaics can benefit from gold nanoparticles, where they allow to reduce the thickness of semiconductor and enhance the absorption of the incident light.[161, 163]

On the other hand, one may see gold nanoparticles' applications depending on what they are used for. Due to their good biocompatibility and relatively low toxicity,[164] gold nanoparticles are widely applied in biology and biomedicine as nanoprobes.

Thanks to enhanced light scattering and absorption, AuNPs are applicable to bioimaging, namely AuNPs scatter light around 10^5-10^6 times stronger than fluorescein.[165-166] This can be also enhanced by use of bigger nanoparticles.[166] Furthermore, the photobleaching of such compounds is neglectable. Dark Field Confocal Imaging (DFCI) allows detection of 10 nm diameter nanoparticles, which is achieved by a high Numerical Aperture lens. Note that the resolution due to the use of AuNPs is notably lower than the diffraction limit of the lens.[165] Not only cancer cell imaging is possible,[167] but also tracking cell division in real time.[168] Since they exhibit good nonlinear optical properties, they can be also used in two-photon microscopy for cancer cell imaging.[169]

Furthermore, an important application of AuNPs is in photodynamic therapy. Gold nanoparticles act as good inhibitors of methylene blue photobleaching,[170] see Figure 39, caused by interactions with the metallic surface. Thus, reduced light source power allows the use of Organic Light Emitting Diodes, which leads to wearable flexible OLEDs, promising for diabetic foot therapy.[171] AuNPs can however act not only as an agent enhancing the Reactive Oxygen Species (ROS) production of other compounds, but they can also be responsible for ROS production, which was shown by Labouret et al. for femtosecond-laser-excited single gold nanorods.[172]

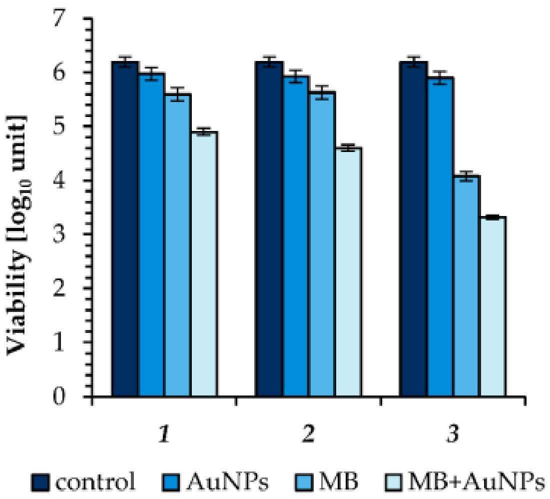

Fig. 39. Viability of *staphylococcus aureus* bacteria after LED irradiation of 5 (a), 15 (b) and 30 (c) minutes. MB = methylene blue, AuNPs = gold nanospheres of 17 nm mean diameter. Reprinted from [170].

Irradiating gold nanoparticles generates heat, which is a problem in most applications, however it emerged a science field called “thermoplasmonics”.[173] The benefits from heating were realized for the first time in 1999 in a study of protein denaturation[174] performed thanks to localized in space and time efficient heating. Nowadays this phenomenon is used in hyperthermia therapy, also called the photothermal effect, where various mechanisms may occur:[173]

- Immune system stimulation and increased diffusion through cell membrane for $T < 41°\mathrm{C}$.
- Blood flow increase and partial cell damage for $41°\mathrm{C} < T < 43°\mathrm{C}$.
- Unfolding of proteins and irreversible cell damage for $43°\mathrm{C} < T < 50°\mathrm{C}$.
- Protein denaturation and damage of DNA for $T > 50°\mathrm{C}$.

It must be kept in mind that this is only a short summary of gold nanoparticles’ applications, with a focus on bio-oriented ones.

4.5.1. Sensing

A significant group of applications of gold nanoparticles is sensing for various purposes. The AuNPs-based sensing mainly relies on the optical phenomena, as depicted in Figure 40.[165] Surface reactivity of gold nanoparticles may be also applied for sensing purposes, however this will not be discussed in this work.[90]

The absorption-based sensing is derived from changes in the UV-Visible spectra of nanoparticles. This can be induced e.g. by change of the refractive index of the surrounding medium.[175] Theoretical calculations based on the Discrete Dipole Approximation (DDA) were performed by Tuersun.[176] The best performance was noted for nanocylinders, as compared with nanoellipsoids and nanobars, see Figure 41 for the LSPR spectral position in respect of surrounding medium refractive index. The sensing sensitivity S was defined as $S = \frac{\Delta\lambda}{\Delta n}$, i.e. the LSPR peak spectral shift divided by the surrounding medium refractive index change. *RIU* stands for *Refractive Index Unit.* The points in the graph represent 4 media, which were taken into account: water ($n=1.33$), alcohol ($n=1.36$), chloroform ($n=1.45$) and benzene ($n=1.50$). It must be noted that the authors have not considered the influence of solvent on nanoparticle's stability or shape.

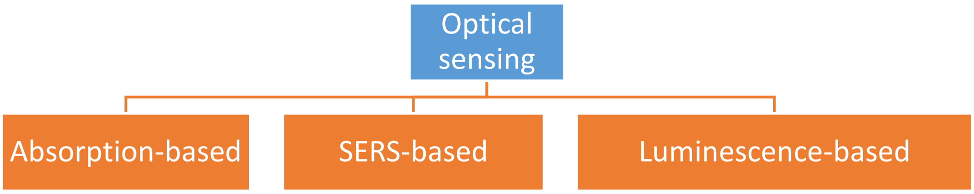

Fig. 40. Scheme of optical sensing techniques, adapted from [165].

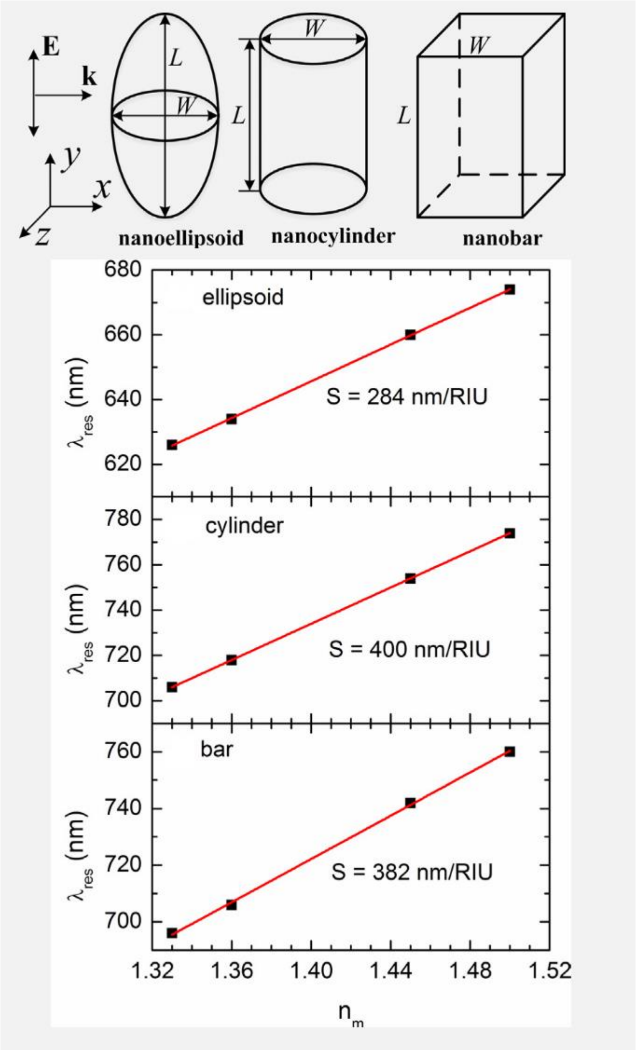

Fig. 41. Shift of the LSPR peak caused by the surrounding medium refractive index change for nanoellipsoids, nanocylinders and nanobars, calculated by the Discrete Dipole Approximation (DDA). Reprinted from [176].

One of the wide fields of absorption-based sensing is biosensing. A simple example is an AuNPs-based pregnancy test:[177] human chorionic gonadotropin from urine was the reason for the gold nanoparticles' suspension to turn pink, meanwhile the pregnancy-negative mixture remained gray. Namely, binding between positively charged nanoparticles and negatively charged gonadotropin caused aggregation.

Gold nanoparticles-based colorimetric sensing is also known in food safety.[107] Namely, they can serve as detection means of hazardous agents, toxins, pesticide drugs, veterinary drugs or heavy metals.[178] Presence of different analytes induces changes in the close vicinity of gold nanoparticles, and in particular their aggregation, which is visible in the UV-Vis spectroscopy. The detection of heavy metal ions will be described in Section 5.3., with focus on copper (II) ions.

As in Figure 40, the second group of sensing application is based on SERS. Surface-Enhanced Raman Scattering SERS has received attention for sensing purposes, which can be ameliorated thanks to gold nanoparticles:[179] Figure 42 shows the enhancement of Raman Scattering by use of AuNPs.

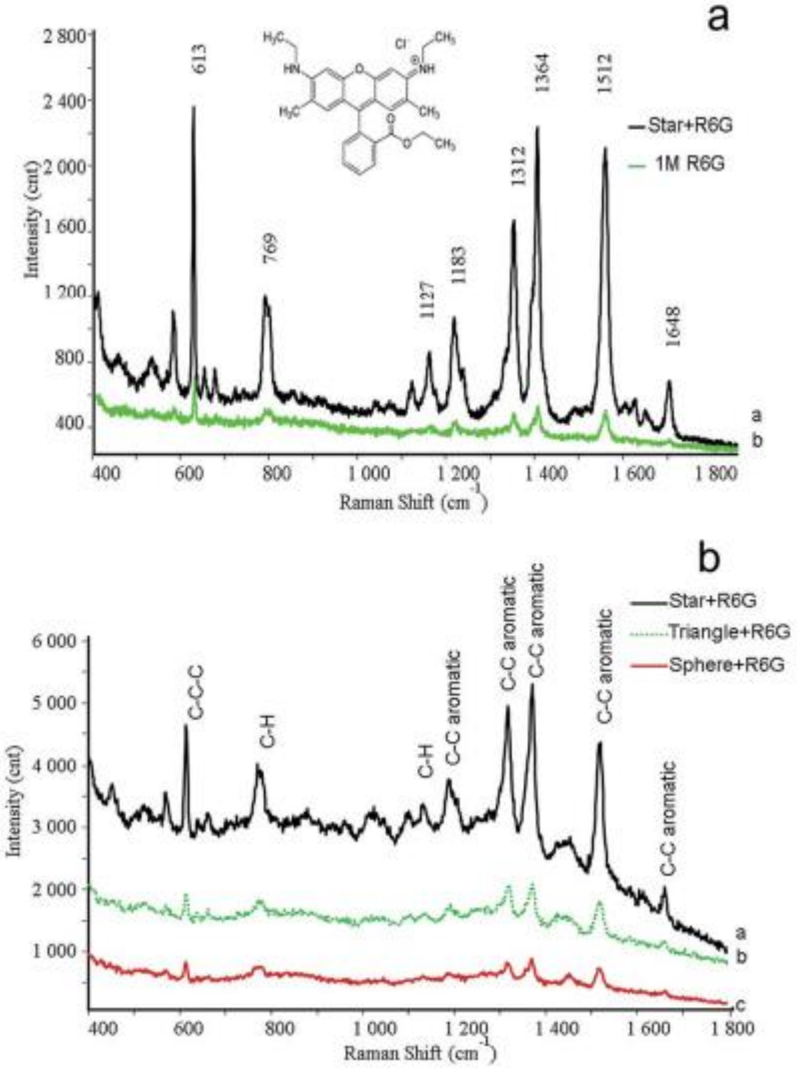

Fig. 42. SERS spectra of gold nanoparticles of different shapes (stars, triangles and spheres) coupled with Rhodamine 6G. (a) Comparison of performance of rhodamine 6G only and rhodamine 6G with gold nanostars. (b) Comparison of performance of rhodamine 6G with gold nanoparticles of different shapes. Reprinted from [179].

Moreover, fluorescence of gold nanoparticles or Förster Resonance Energy Transfer FRET are good tools for sensing applications,[165] as in the third group in Figure 40. However, fluorescence sensing can be also applied where gold nanoparticles quench emission of an another compound: for instance, rhodamine B molecules are adsorbed on nanoparticles' surface, but in the presence of mercury ions, the dye is released from AuNPs' surface, which effects in increased fluorescence.[180] A similar behaviour was described for thiols detection in living cells.[181]

Chemical flexibility of AuNPs, namely the variety of stabilizing agents and relative simplicity of conjugation with different compounds is advantageous for sensing in bionanotechnology,[182] including cancer diagnostics[183] or detection of proteins and nucleic acids.[182, 184-185]

5. Results and discussion

This part of the thesis includes three publications, where Krzysztof Nadolski is the first author: *Adverse Role of Shape and Size in Second-Harmonic Scattering from Gold Nanoprisms* (The Journal of Physical Chemistry C, 2020, 124, p. 14797-14803),[151] *Sensitivity of Gold Nanoparticles Second Harmonic Scattering to Surrounding Medium Change* (Journal of Molecular Liquids, 2023, 388, 122704)[186] and *Sensing Copper (II) Ions with Hyper Rayleigh Scattering from Gold Nanoparticles* (The Journal of Physical Chemistry C, 2023, 127, p. 13097-13104).[187] First of all, in Chapter 5.1. the author declared his contribution to each publication. Chapters 5.2, 5.3 and 5.4 are dedicated to one publication each. Prior to every publication, it synopsis is included.

5.1. PhD candidate statement about the substantive contribution to the presented publications

All of the presented studies were supervised by prof. Katarzyna Matczyszyn and prof. Pierre-Francois Brevet, which included conceptualization, acquiring funds and planning the study.

In the case of *Adverse Role of Shape and Size in Second-Harmonic Scattering from Gold Nanoprisms* the author contributions have been also mentioned in the publication. Namely, Krzysztof Nadolski conducted the measurements with assistance of Emmanuel Benichou and Christian Jonin. The sample characterization was performed by Andrzej Żak and Nina Tarnowicz-Staniak, however the PhD candidate described the outcome and performed the calculations regarding nanoparticle size and shape. Krzysztof Nadolski took lead in writing the manuscript with the assistance of Prof. Pierre-Francois Brevet.

For the study of *Sensitivity of Gold Nanoparticles Second Harmonic Scattering to Surrounding Medium Change*, the samples were prepared and characterized by Krzysztof Nadolski. The idea originators of the research were Krzysztof Nadolski, Prof. Katarzyna Matczyszyn and Prof. Pierre-Francois Brevet. Krzysztof Nadolski also performed and analyzed the HRS experiments, with the help of Christian Jonin, Estelle Salmon and Zacharie Behel. Prof. Pierre-Francois Brevet and Krzysztof Nadolski did the theoretical calculations. The manuscript was mainly written by Krzysztof Nadolski and Prof. Pierre-Francois Brevet.

The article *Sensing Copper (II) Ions with Hyper Rayleigh Scattering from Gold Nanoparticles* was written mainly by Krzysztof Nadolski and Prof. Pierre-Francois Brevet. Krzysztof Nadolski prepared the samples and performed UV-Vis spectroscopic measurements. Prof. Tomasz Goszczyński performed and preliminarily analyzed DLS and Zeta-potential studies, which were further described by Krzysztof Nadolski. The TEM pictures were commercially performed at the Polish Academy of Sciences in Wrocław, Poland, and then analyzed by Krzysztof Nadolski. The HRS measurements were performed and analyzed by Krzysztof Nadolski, with the assistance of Fabien Rondepierre and Christian Jonin. Theoretical adjustment of the obtained data was performed by Prof. Pierre-Francois Brevet and Krzysztof Nadolski.

The PhD candidate declares that the three presented articles were performed within the PhD thesis preparation and will not be a part of any other thesis in the future. The study was predominantly performed by Krzysztof Nadolski, with the assistance of other researchers.

5.2. Adverse Role of Shape and Size in Second-Harmonic Scattering from Gold Nanoprisms

5.2.1 Synopsis of the publication

The publication “Adverse Role of Shape and Size in Second-Harmonic Scattering from Gold Nanoprisms” was published in 2020 in The Journal of Physical Chemistry C.[151] The aim of this work was to study HRS of non-centrosymmetrical nanoparticles, in particular gold nanotriangles, also called gold nanoprisms or triangular gold nanoplates.

The main part of the article is divided in 4 parts: Introduction, Experimental Section, Results and Discussion and Conclusions.

Within the Introduction part, the authors briefly described the Localized Surface Plasmon Resonance phenomenon, and then shortly characterized the Second Harmonic Generation and Hyper Rayleigh Scattering of metallic nanoparticles. It has been stressed that until that moment, only centrosymmetrical nanoparticles had been studied, with an exception of gold nanodecahedra[148], which turned out to have five-fold symmetry, and thus behaved like centrosymmetrically-shaped nanoparticles.

The Experimental Section introduces the outcome of synthesis and characterization, which is described in more detail in the Supporting Information file, included in this thesis directly after the article itself. Namely, nanotriangles of mean edge length 26, 61, 78 and 87 nm were obtained in an own synthesis protocol, based on protocols by Chen[188], Jones[189] and Nikoobakht[190]. They were then characterized by UV-Vis spectrometry and Transmission Electron Microscopy.

It is worth noting that the studied samples contained also a lot of nanospheres, namely up to 58% (see Table 1), which is also a novel approach, since until then, only samples containing one nanoparticle type (in particular: shape) had been studied.

The Results and Discussion part has been divided into sub-chapters: First Hyperpolarizability, Polarization Analysis and Theoretical Simulations.

The First Hyperpolarizability part includes the protocol used to obtain the first hyperpolarizability value. The normalized HRS intensity vs gold nanoparticles’ concentration graph has been divided into two separate figures, namely Figure 1a and 1b for improved clarity. In fact, the synthesis protocol for the 26 nm sample was different, thus the nanoparticle concentration was also much higher compared to other samples.

The first hyperpolarizabilities were then calculated, with a proposition how to deal with different shapes within the samples, see Equations (2) and (3). Then, the first hyperpolarizability of nanospheres and nanotriangles were presented in Tables 2 and 3. Surprisingly, the values were significantly lower, compared to values of nanoparticles' of centrosymmetrical shapes, reported previously in the literature. Furthermore, calculating first hyperpolarizability per surface unit resulted in a constant value for all sizes, which proved that the behaviour scales with nanoparticles' surface, as opposed to centrosymmetrical nanoparticles, where it would scale with nanoparticles' volume for large nanoparticles, e.g. bigger than 50 nm.

For further investigation of the HRS nature of gold nanoprisms, polarization-resolved measurements were performed, as described in the Polarization Analysis section. Firstly, the theory and protocol of such measurements was described. Then, the parameters for quantification of such measurements were introduced, see Equations (6), (7) and (8). The polar plot of #26 sample can be found in Figure 2, whereas the remaining graphs are included in the Supporting Information file, see Figure S4. All calculated parameters are shown in Table 4. First of all, the depolarization ratio value of around 0.44 is far from 0.2, expected for one-fold symmetry[140], yielding to 0.67, which is a value expected for one-point three-fold symmetry[139]. Furthermore, the two retardation parameters are significantly lower in the case of nanoprisms, as compared to centrosymmetrical nanoparticles.

In the Theoretical Simulations part, a simple model was proposed. Assuming a two-dimensional triangular gold-nanoplates with vanishingly small thickness, it was confirmed that the ζ^V parameter remains far from 1, as opposed to nanospheres of diameter over 50 nm. The depolarization ratio was in this case very close to the theoretical value of a point-like three-fold structure, i.e. 0.67.

The study was summarized in the Conclusions part. It was underlined that the noncentrosymmetrical shape may be disadvantageous for sensing applications, due to relatively low first hyperpolarizability, however on the other hand its low signal retardation level and the presence of sharp tips may be profitable.

The final parts of the publication are Associated Content, describing the Supporting Information File, Author Information, including authors' affiliations and a description of author contributions to the study, Acknowledgements and References.

5.2.2 Publication

THE JOURNAL OF PHYSICAL CHEMISTRY C

pubs.acs.org/JPCC

Article

Adverse Role of Shape and Size in Second-Harmonic Scattering from Gold Nanoprisms

Krzysztof Nadolski, Emmanuel Benichou, Nina Tarnowicz-Staniak, Andrzej Żak, Christian Jonin, Katarzyna Matczyszyn,* and Pierre-François Brevet*

Cite This: *J. Phys. Chem. C* 2020, 124, 14797−14803

Read Online

ACCESS | Metrics & More | Article Recommendations | Supporting Information

ABSTRACT: Gold nanoparticles are widely used in different fields. They are currently under extensive investigation with regard to their linear and nonlinear optical properties. So far, nanoparticles with centrosymmetrical shapes, such as nanospheres or nanorods, have received the main attention. In this work, the properties of gold nanoprisms exhibiting a highly noncentrosymmetrical threefold symmetry are investigated with hyper-Rayleigh scattering (HRS). Aqueous solutions of gold nanospheres and nanoprisms with different sizes were synthesized. The first hyperpolarizability magnitudes of both the nanospheres and nanoprisms were determined separately with the assumption of a surface origin of the nonlinearity. Using polarization-resolved HRS, retardation is shown to be largely underdeveloped for the nanoprisms as opposed to the nanospheres. The nanoprism shape noncentrosymmetry has therefore a leading role in the HRS response although it is also shown that surface defects induce deviations from the ideal threefold symmetry.

■ INTRODUCTION

Metallic nano-objects, such as gold, silver, or platinum nanoparticles with a size of the order of 100 nanometers or smaller, have been gaining growing interest over the last few years driven by the potential applications envisaged. They exhibit localized surface plasmon resonances (LSPR) due to the oscillation of their conduction band electrons within a small volume yielding enhanced electromagnetic fields in their immediate vicinity providing unique optical properties.[1] LSPR can be adjusted by factors such as size, shape, material, morphology, or environments. Hence, metallic nanoparticles offer a large range of capabilities, and many applications have been proposed and realized based on these properties, from nanoantennas for sensing[2,3] to bioimaging[4,5] or drug delivery.[6] Their linear optical properties based on the LSPR are now well understood and documented.[7,8] However, this ability to enhance electromagnetic fields in a small volume has also sparked deep interest in their nonlinear optical response that can benefit as well from this feature through enhanced cross-sections.

Second-harmonic generation (SHG), the simplest of the nonlinear optical phenomena involving the conversion of two photons at a fundamental frequency into a single photon at the harmonic one, has been at the center of intense research efforts.[9,10] At the nanoscale, where phase matching becomes irrelevant, this conversion phenomenon is extremely sensitive to the symmetry of the nano-object shape.[11] It is therefore crucial to perform experiments in the absence of any supporting substrates to ensure that the SHG response is solely due to the nanoparticles and is not affected by the substrate. This condition can be attained with second-harmonic scattering, also known as hyper-Rayleigh scattering (HRS),[12] that has now become the main method for the determination of the first hyperpolarizability of molecules and nanoparticles dispersed in liquid solutions.[13]

The determination of the first hyperpolarizability of a large variety of metallic nanoparticles has already been reported. Those studies have shown that the origin of the HRS response essentially stems from the nanoparticle surface, being effectively a local electric dipole contribution at the first order owing to the centrosymmetry of the crystal lattice with weaker contributions from higher orders like field gradients. Shape is therefore critical in determining the absolute value of first hyperpolarizabilities although size must also be accounted for. Nanospheres,[14] nanorods,[15] or nanocubes[16] have thus been extensively studied in the past few decades. In addition, deviation from the perfect geometrical shape caused by the nonideality of the nanoparticle surface due to roughness or shape defects like faceting or tip rounding is also essential in determining the HRS response.[17] Nevertheless, a crucial issue that still remains is dealing with the competition between the relative influence of shape and size. Indeed, retardation, or the variation of the spatial phase of the electromagnetic fields over distances equal to the size of the nanoparticles, dramatically modifies the HRS response for gold nanoparticles having sizes larger than 50 nm and even smaller sizes for silver nanoparticles. Retardation indeed favors the electric quadru-

Received: April 20, 2020
Revised: June 9, 2020
Published: June 15, 2020

ACS Publications

14797

https://dx.doi.org/10.1021/acs.jpcc.0c03489
J. Phys. Chem. C 2020, 124, 14797−14803

pole contribution in particular and higher multipole orders as well.[16,18] In order to fully understand the HRS response from all these nanoparticles, many different approaches have been proposed.[19−24] Recently, a simple model based on nonpolarizable nonlinear dipoles has also been proposed to investigate this question.[25] In this approach, the nanoparticles are described with a small set of nonlinear dipoles. For nanocubes, this number is reduced to eight and corresponds to the eight corners acting as localized regions where the electromagnetic field enhancements are the largest.

Experiments on noncentrosymmetrical plasmonic nanoparticles have been reported for gold nanodecahedra.[26] Although decahedra have no symmetry center, they behave like centrosymmetrical nanoparticles due to the accidental cancellation of the response associated with a symmetry-five stemming from the two back-to-back pentagonal pyramids. In order to go further into this direction, we investigate here the case of gold nanoprisms, also known as nanotriangles or triangular nanoplates. These nanoparticles are noncentrosymmetric due to their intrinsic threefold symmetry. First hyperpolarizabilities have already been reported[27,28] but here, we wish to discuss the signal contribution of shape noncentrosymmetry versus size retardation from an experimental point of view as this has not been performed before. In addition, the question of the presence of nanospheres in non-negligible amounts among the nanoprisms must be addressed. We therefore discuss initially the determination of the absolute first hyperpolarizabilities of both the gold nanoprisms and nanospheres. Then, polarization-resolved HRS experiments are presented to provide a quantitative analysis of the competition between the relative influence of centrosymmetry and retardation.

EXPERIMENTAL SECTION

Four different aqueous solutions of gold nanoparticles were obtained, as presented in Table 1. The edge length corresponds to the nanospheres, since the solutions were mixtures of nanoprisms and nanospheres. Synthesis and characterization of the nanoparticles, as well as the optical setup, are described in the Supporting Information.

Table 1. Nanoprism Solution Content, Nanoprism Average Edge Length, and Nanosphere Average Diameter in the Obtained Samples as Determined from TEM Images

sample	nanoprism content (%)	edge length (nm)	diameter (nm)
#26	42	26 ± 8	23 ± 6
#61	47	61 ± 15	44 ± 21
#78	74	78 ± 21	57 ± 22
#87	66	87 ± 21	63 ± 30

RESULTS AND DISCUSSION

First Hyperpolarizability. The first hyperpolarizability values were obtained by the standard technique of HRS. It has been previously shown that plotting the HRS intensity as a function of the solution nanoparticle concentration yields a line whose slope p is related to the first hyperpolarizability as

$$p = \frac{<\beta_s^2>}{N_w < \beta_w^2>} \quad (1)$$

In eq 1, $<\beta_s^2>$ and $<\beta_w^2>$ are the squares of the first hyperpolarizabilities of the nanoparticles and the solvent molecules, here water, in the laboratory frame averaged over all orientations, and N_w is the number of solvent molecules per unit volume. The sample concentrations were determined from their gold atom content calculated from the 400 nm absorbance where surface plasmon resonances do not play any role[29] and the nanoparticle size obtained from the TEM pictures. The crystal structure of gold was assumed to be *fcc* with a unit cell size of 0.408 nm.[30] The first hyperpolarizability value of water was taken as 0.087×10^{-30} esu and used as the internal reference as reported by Duboisset et al.[31]

The plots of the HRS intensity as a function of the nanoparticle concentration normalized to the neat solvent intensity are presented in Figure 1a,b. Since sample #26 was obtained by a separate synthesis protocol, its initial nanoparticle concentration is notably higher and is therefore presented on a separate graph for improved clarity. Uncertainties were calculated by applying simple counting statistics methods. The first hyperpolarizability values as given by eq 1 and reported in Table 2 where β stands for $\sqrt{<\beta_s^2>}$ must be attributed to the mixture of nanoprisms and nanospheres. Because the HRS intensity is additive, we have

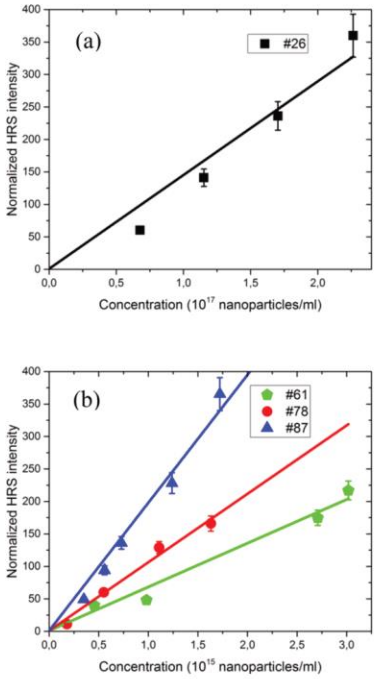

Figure 1. Solvent normalized HRS intensity for samples (a) #26, (b) #61, #78, and #87 as a function of the nanoparticle concentration. Solid lines are the corresponding linear fits with the intercept set to unity.

$$<\beta_{s}^{2}> = \alpha < \beta_{nP}^{2} > + (1 - \alpha) < \beta_{nS}^{2}> \tag{2}$$

Table 2. First Hyperpolarizability β and First Hyperpolarizability per Unit Surface β_0 for the Nanospheres in all Samples

sample	β (esu)	β_0 (esu/nm^2)
#26	0.5×10^{-27}	3.3×10^{-31}
#61	4.0×10^{-27}	6.6×10^{-31}
#78	5.0×10^{-27}	4.9×10^{-31}
#87	6.8×10^{-27}	5.4×10^{-31}

by introducing the first hyperpolarizability of nanoprisms $<\beta_{nP}^{2}>$ and nanospheres $<\beta_{nS}^{2}>$. In eq 2, α is the solution content in nanoprisms as given in Table 1. The independent determination of the first hyperpolarizability of the nanoprisms and nanospheres however requires a complementary assumption.

The latter can be based on the surface origin of the first hyperpolarizability of gold nanoparticles in the size range used here where retardation is weak. In this size range, the first hyperpolarizability has been shown to scale with the surface area of the nanoparticles.[18,24] Therefore, if we apply this principle in the present case, with symmetry cancellation of the opposing top and bottom surface for the nanoprisms, we get

$$\sqrt{<\beta_{nP}^{2}>} = \varepsilon \sqrt{<\beta_{nS}^{2}>} \tag{3}$$

where the parameter $\varepsilon = \varepsilon_{nS}/\varepsilon_{nP}$ is the ratio of the HRS active surface area for the nanoprisms and nanospheres formally introduced through

$$\sqrt{<\beta_{I}^{2}>} = \int \beta_0 \mathrm{d}A_I = \beta_0 \int \mathrm{d}A_I = \varepsilon_I \beta_0 \tag{4}$$

where the subscript I stands for nS or nP. The integral is performed over the closed surface of the nanosphere or nanoprism, whereas β_0 stands for hyperpolarizability per unit surface. In eq 4, cancellation of terms in the integral occurs due to symmetry. Therefore, ε_I may not be equal to the geometrical surface.

Using eqs 2 and 3, we can provide the first hyperpolarizability of the nanoprisms and nanospheres for all samples, see Tables 2 and 3.

Table 3. First Hyperpolarizability β and First Hyperpolarizability per Unit Surface β_0 for the Nanoprisms in all Samples

sample	β (esu)	β_0 (esu/nm^2)
#26	0.4×10^{-27}	2.7×10^{-31}
#61	3.8×10^{-27}	4.4×10^{-31}
#78	4.7×10^{-27}	3.3×10^{-31}
#87	6.5×10^{-27}	3.6×10^{-31}

From a general standpoint, the first hyperpolarizability magnitudes determined for the gold nanospheres contained in the aqueous solution samples are much smaller than what can be obtained from the citrate reduction of the metallic salt. This feature further demonstrates the extreme sensitivity of the nanoparticle surface to the synthesis and therefore exact composition and morphology. Indeed, El Harfouch et al.[15] reported first hyperpolarizability values for gold nanospheres and nanorods in the range of 10^{-25}–10^{-24} esu, about 2 orders of magnitude higher than those for the present gold nanoprisms, in line with data obtained for other plasmonic nanoparticles.[16,32]

In order to further support the surface origin of the nonlinearity, the first hyperpolarizabilities were normalized per unit surface area, see Table 2. The value of about $(5 \pm 2) \times 10^{-31}$ esu/nm^2 is obtained. This value is constant once normalized to the nanoparticle surface area, as expected. Of note, a slightly weaker value is obtained for sample #26, possibly due to the nonresonant character of the conditions. A tentative normalization by the nanoparticle volume, data not shown, identical to a normalization by the number of atoms present in the nanoparticles, does not lead to a constant normalized first hyperpolarizability, demonstrating the effectiveness of the surface origin of the nonlinearity.

A similar analysis was then performed for the nanoprisms, and the data are reported in Table 3. The first hyperpolarizability per unit surface area for the nanoprisms is found to be $(3 \pm 2) \times 10^{-31}$ esu/nm^2 and, as expected, similar to that of the nanospheres, since the synthesis is identical. Considering the UV−vis absorption spectra, a non-negligible contribution from the surface plasmon resonance at a fundamental wavelength of 800 nm may be present. This is perhaps the reason for the weaker value observed for sample #26 that is off resonance at both the fundamental and the harmonic wavelengths.

Polarization Analysis. As it has been demonstrated in the past,[15,16] increasing the size of centrosymmetrical plasmonic nanoparticles introduces a significant contribution of retardation in the total signal, observable in the polarization analysis of the HRS intensity. In this case, a clear quadrupole contribution is observed through the appearance of four lobes on the vertically polarized HRS intensity as a function of the input polarization angle. Since gold nanoprisms are noncentrosymmetrical owing to their threefold symmetry, their response is expected to noticeably deviate from this behavior. To perform this polarization-resolved study, an analyzer was placed before the spectrometer. The polar plot of sample #26 is presented in Figure 2, and the polar plots for the other samples are provided in the Supporting Information. They are all very similar irrespective of the nanoprism edge length.

All obtained polar graphs were then adjusted with the following expression[33] following the standard procedure:

$$I^{X} = a^{X}\cos^{4}\gamma + b^{X}\cos^{2}\gamma\,\sin^{2}\gamma + c^{X}\sin^{4}\gamma \tag{5}$$

where X corresponds to the vertical V or horizontal H output polarization selection, and a^X, b^X, and c^X are three intensity parameters, whereas γ is the input fundamental polarization angle. From these parameters and following previous works, three parameters were determined from eq 5. The first one is known as the depolarization ratio defined as

$$D^{V} = c^{V}/a^{V} \tag{6}$$

The two other parameters are termed the retardation parameters for the V and H polarized intensity and are defined as[15,34]

$$\zeta^{V} = (b^{V} - a^{V} - c^{V})/b^{V} \tag{7}$$

$$\zeta^{H} = (a^{H} - c^{H})/(a^{H} + c^{H}) \tag{8}$$

The experimentally determined depolarization and retardation parameters are presented in Table 4. Both parameters ζ^V

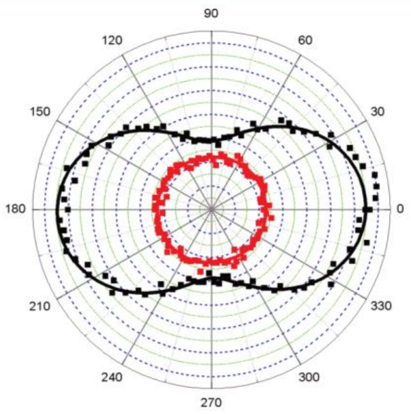

Figure 2. Polar plots of sample #26. The black curve represents vertically polarized HRS intensity, and the red curve represents horizontally polarized HRS intensity.

Table 4. Retardation Parameters ζ^V and ζ^H and Depolarization Ratio D^V for All Samples

sample	ζ^V	ζ^H	D^V
#26	0.04	0.02	0.44
#61	0.05	0.04	0.47
#78	0.11	0.10	0.42
#87	0.09	0.10	0.42

and ζ^H grow with the nanoparticle size as expected for retardation with somewhat saturation for samples #78 and #87. However, the discussion of the size evolution of these two parameters must be performed in light of the significant nanosphere content in the samples. Indeed, this increase can be attributed to the nanospheres, as it is known that these two parameters increase with their diameter. Introducing the nanoprism content of the nanoparticle solutions, eq 5 yields

$$\zeta^X = \alpha\zeta^X_{nP} + (1-\alpha)\zeta^X_{nS} \tag{9}$$

In principle, for perfect nanospheres, it has been shown previously that $\zeta^V_{nS} = 1$ and $\zeta^H_{nS} = 0$, namely; they exhibit a pure quadrupole response. However, in most cases, nanospheres are not perfect geometrical spheres, and shape defects induce a much reduced ζ^V_{nS} value, whereas ζ^H_{nS} remains close to zero. Because these retardation parameters do not depend on the first hyperpolarizability itself as they are effectively intensity ratios, previously reported retardation parameters can be used. Values between 0 and 0.2 have been reported for the ζ^V_{nS} retardation parameter for gold nanospheres.[16] With the nanoprism contents given in Table 1, it appears that ζ^V_{nP} and ζ^H_{nP} values must vanish altogether within experimental error. Hence, despite a non-negligible size and therefore non-negligible spatial extension, nanoprisms do not exhibit significant retardation. This property results from the threefold noncentrosymmetry of their shape as opposed to the centrosymmetric nanospheres.

We now turn to the depolarization ratio D^V. A theoretical value $D^V = 0.67$ is expected for a pointlike planar threefold geometry. An archetypal system with this geometry is represented by crystal violet. On the opposite, a value $D^V = 0.2$ is expected for a pointlike onefold system.[35,36] The samples investigated in this study contained a significant amount of nanospheres that alters to a notable extent the assignment of this parameter to the nanoprisms only. In addition, nanoprisms are not pointlike structures. Nevertheless, the measured depolarization ratios all have values around 0.45, see Table 4, weaker than the 2/3 expected for the pure threefold symmetry but significantly different from the onefold 0.2 value. This value emphasizes the nature of the nanoparticle HRS response that arises from a spatially distributed nonlinearity. Hence, since nanospheres possess a depolarization ratio of this magnitude,[37] nanoprisms also exhibit depolarization ratios of 0.45. This value differs significantly from the perfect planar threefold symmetry, indicating that the nanoprism nonlinearity cannot be fully associated with such a perfect geometry. Shape defects like morphologically induced differences in the local field enhancements at the tips of the prism nanostructure must play some role.

Theoretical Simulations. In order to provide a deeper understanding of the experimental data and to unravel the origin of the HRS signals from nanoprisms, theoretical simulations were performed using a discrete nonpolarizable nonlinear dipole model.[38] A D_{3h} symmetry for equilateral triangles with a defined edge length was assumed, see Figure 3.

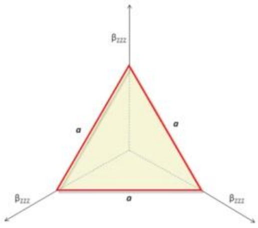

Figure 3. Schematics of the nanoprism D_{3h} symmetry assumed in the theoretical simulations.

It is interesting to note that in the case of equilateral prisms, a nonlinear response stemming from the edge surface area behaves similarly to the one arising from the three sharp tips of the nanostructure. Following the previous work reported for nanocubes, the nanoprism HRS response was assumed to stem from these three sharp tips of the structure, to which a single hyperpolarizability component β_{zzz} nonlinear dipole was attributed. Tips are known to provide large electromagnetic field enhancements and therefore are the siege of enhanced HRS. The absence of contribution from the top and bottom faces is therefore in line with the above postulated assumptions.

Using this arrangement of the three equal nonlinear dipoles, the depolarization ratio D^V, along with the two retardation parameters ζ^V and ζ^H, was simulated with respect to the nanoprism edge length, see Figure 4. The corresponding polarization-resolved HRS intensity plots for small (vanishing edge length, i.e., the three nonlinear dipoles are co-located) gold nanoprisms are given in Figure 5, meanwhile plots for large (100 nm edge length) gold nanoprisms are included in the Supporting Information. For small nanoprisms, we do not observe any retardation as expected, and the response is similar

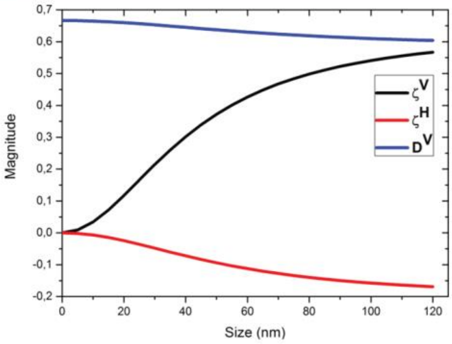

Figure 4. Simulated retardation $\zeta_{\mathrm{nP}}^{\mathrm{V}}$ and $\zeta_{\mathrm{nP}}^{\mathrm{H}}$ and the depolarization ratio D^{V} as a function of the gold nanotriangle edge length.

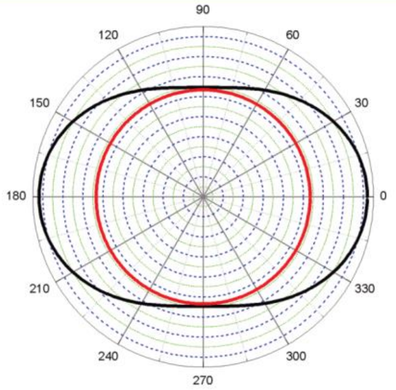

Figure 5. Polar plots for vanishingly small edge length nanoprisms. The black curve represents vertically polarized HRS intensity, and the red curve represents horizontally polarized HRS intensity.

to that of molecules with the same symmetry like crystal violet.[36] The polar plot of small edge length nanoprisms corresponds well to the experimentally obtained graph for sample #26, see Figure 2, i.e., showing a very low level of retardation. On the opposite, for large nanoprisms, retardation is significant. Theoretically calculated retardation parameters for the large 100 nm edge length nanoprisms are respectively $\zeta_{\mathrm{nP}}^{\mathrm{V}} = 0.54$ and $\zeta_{\mathrm{nP}}^{\mathrm{H}} = -0.16$, whereas the depolarization ratio has only weakly evolved from $D^{\mathrm{V}} = 2/3$, its value for vanishing edge length, to $D^{\mathrm{V}} = 0.61$.

Theoretical simulations provide a deeper insight into the experimental data. A similar approach was performed for silver nanocubes, as reported by Russier-Antoine et al.,[16] where the simulated graphs exhibited significantly higher retardation due to the centrosymmetry of the nanocubes. For the nanoprisms, the simulations performed assuming a perfect threefold symmetry yield rather high values of the parameter ζ^{V} as compared to the experimental data. Introducing three unbalanced nonlinear dipoles disposed at the three tips of the nanoprisms provides lower ζ^{V} values, in agreement with the experimental observations. This breaking of the perfect threefold symmetry is also seen through the depolarization ratio measured, which is weaker than the theoretical one.

CONCLUSIONS

Aqueous suspensions of gold nanoprisms with an average edge length ranging from 26 to 87 nm were successfully synthesized combining various synthesis protocols known in the literature and investigated with polarization-resolved HRS. The determined first hyperpolarizabilities are rather low as compared to the values reported in the literature for other plasmonic nanoparticle shapes, such as rods or spheres. This feature emphasizes the sensitivity of this parameter to the nature of the nanoparticle surface and must be taken into account when selecting nanostructures with an efficient HRS response. The polarization analysis supports an origin of the response stemming from the nanoparticle surface, without significant retardation contributions, although this property can also be understood similarly as stemming from the three nanoprism tips. The depolarization ratio complements this analysis and underlines the potential deviation of the nanoprism exact shape from that of perfect equilateral prisms. All these results can be rationalized with a simple model involving three nonlinear dipoles simulating the three sharp tips of the nanoprisms. Finally, it is interesting to note that this in-depth analysis of the nanoprisms is performed in the presence of nanospheres produced during the same synthesis providing evidence for information extraction from nanoparticle mixtures.

Surprisingly, the noncentrosymmetrical shape of the nanoprisms may be a disadvantage for applications like sensing, since the first hyperpolarizabilities are not as high as expected considering their noncentrosymmetric shape. This feature may result in a lower sensitivity required to probe external medium changes. This may remain to be confirmed, though the three tips may be sufficiently sensitive. In any case, the weak contribution of retardation may be profitably used, especially for the largest nanoparticles, where the first hyperpolarizability will only stem from the surface without significant contribution from the volume, a clear asset in sensing for example.

ASSOCIATED CONTENT

Supporting Information

The Supporting Information is available free of charge at https://pubs.acs.org/doi/10.1021/acs.jpcc.0c03489.

Detailed synthesis description, sample characterization methods, and a supplemental polar graph of theoretically simulated polarization-resolved HRS signal of big (100 nm edge length) gold nanoprisms followed by experimentally obtained polar plots of samples #61, #78, and #87 (PDF)

AUTHOR INFORMATION

Corresponding Authors

Katarzyna Matczyszyn − *Advanced Materials Engineering and Modelling Group, Wroclaw University of Science and Technology, Wroclaw, Poland;* orcid.org/0000-0001-8578-8340; Email: katarzyna.matczyszyn@pwr.edu.pl

Pierre-François Brevet − *Institut Lumière Matière, University of Lyon, UMR 5306 CNRS and Université Claude Bernard*

Lyon 1, Villeurbanne, France; orcid.org/0000-0002-9097-0187; Email: pfbrevet@univ-lyon1.fr

Authors

Krzysztof Nadolski – *Institut Lumière Matière, University of Lyon, UMR 5306 CNRS and Université Claude Bernard Lyon 1, Villeurbanne, France; Advanced Materials Engineering and Modelling Group, Wroclaw University of Science and Technology, Wroclaw, Poland*

Emmanuel Benichou – *Institut Lumière Matière, University of Lyon, UMR 5306 CNRS and Université Claude Bernard Lyon 1, Villeurbanne, France;* orcid.org/0000-0003-0590-6998

Nina Tarnowicz-Staniak – *Advanced Materials Engineering and Modelling Group, Wroclaw University of Science and Technology, Wroclaw, Poland*

Andrzej Żak – *Electron Microscopy Laboratory, Faculty of Mechanical Engineering, Wroclaw University of Science and Technology, Wroclaw, Poland*

Christian Jonin – *Institut Lumière Matière, University of Lyon, UMR 5306 CNRS and Université Claude Bernard Lyon 1, Villeurbanne, France*

Complete contact information is available at:
https://pubs.acs.org/10.1021/acs.jpcc.0c03489

Author Contributions

K.M. and P.F.B. conceived and coordinated the project. K.N., E.B., and C.J. conducted the measurements. N.T-S. synthesized the nanoparticles. N.T-S. and A.Ż. characterized the samples. P.F.B. performed the simulations. K.N. and P.F.B. took the lead in writing the manuscript. All authors provided critical feedback and helped to shape the research, analysis, and manuscript.

Notes

The authors declare no competing financial interest.

ACKNOWLEDGMENTS

E.B., C.J., and P.F.B. thank the French Agence nationale pour la Recherche (ANR) for funding under contract number CE24-2017-RACINE. K.M, K.N., and N.T.-S. acknowledge funding from the Polish National Science Centre for support under Harmonia project UMO-2016/22/M/ST4/00275. K. M., P.F.B., K.N., N.T-S., and C.J. thank Campus France and The Polish National Agency for Academic Exchange for financial support under PHC Polonium "NanoSHG" project PPN/BFR/2019/1/00030. K.N. thanks GDR Or-nano for a subvention for academic stay at ILM, Lyon, France. A.Ż. gratefully acknowledges funding from the National Science Centre (PL) under "Miniatura" grant number 2019/03/X/NZ3/02100. The authors thank Ms. Marta Piksa for assistance regarding the visual part of this work.

REFERENCES

(1) Louis, C.; Pluchery, O., *Gold Nanoparticles for Physics, Chemistry, and Biology*. Imperial College Press: 2012, DOI: 10.1142/p815.

(2) Saha, K.; Agasti, S. S.; Kim, C.; Li, X.; Rotello, V. M. Gold nanoparticles in chemical and biological sensing. *Chem. Rev.* **2012**, *112*, 2739–2779.

(3) Stipe, B. C.; Strand, T. C.; Poon, C. C.; Balamane, H.; Boone, T. D.; Katine, J. A.; Li, J.-L.; Rawat, V.; Nemoto, H.; Hirotsune, A.; et al. Magnetic recording at 1.5 Pb m−2 using an integrated plasmonic antenna. *Nat. Photonics.* **2010**, *4*, 484–488.

(4) Brach, K.; Olesiak-Banska, J.; Waszkielewicz, M.; Samoc, M.; Matczyszyn, K. DNA liquid crystals doped with AuAg nanoclusters: One-photon and two-photon imaging. *J. Mol. Liq.* **2018**, *259*, 82–87.

(5) Olesiak-Banska, J.; Gordel, M.; Matczyszyn, K.; Shynkar, V.; Zyss, J.; Samoc, M. Gold nanorods as multifunctional probes in a liquid crystalline DNA matrix. *Nanoscale.* **2013**, *5*, 10975–10981.

(6) Visaria, R. K.; Griffin, R. J.; Williams, B. W.; Ebbini, E. S.; Paciotti, G. F.; Song, C. W.; Bischof, J. C. Enhancement of tumor thermal therapy using gold nanoparticle-assisted tumor necrosis factor-alpha delivery. *Mol. Cancer. Ther.* **2006**, *5*, 1014–1020.

(7) Amendola, V.; Pilot, R.; Frasconi, M.; Marago, O. M.; Iati, M. A. Surface plasmon resonance in gold nanoparticles: a review. *J. Phy. Condens. Matter.* **2017**, *29*, 203002.

(8) Garcia, M. A. Surface plasmons in metallic nanoparticles: fundamentals and applications. *J. Phys. D: Appl. Phys.* **2011**, *44*, 283001.

(9) Butet, J.; Brevet, P.-F.; Martin, O. J. F. Optical Second Harmonic Generation in Plasmonic Nanostructures: From Fundamental Principles to Advanced Applications. *ACS. Nano.* **2015**, *9*, 10545–10562.

(10) Deska, R.; Olesiak-Banska, J.; Glowacki, E.; Samoc, M.; Matczyszyn, K. Two-photon excited luminescence and second-harmonic generation in quinacridone microstructures. *Dyes. Pigm.* **2020**, *177*, 108628.

(11) Boyd, G. T.; Rasing, T.; Leite, J. R. R.; Shen, Y. R. Local-field enhancement on rough surfaces of metals, semimetals, and semiconductors with the use of optical second-harmonic generation. *Phys. Rev. B.* **1984**, *30*, 519–526.

(12) Maker, P. D.; Terhune, R. W.; Nisenoff, M.; Savage, C. M. Effects of Dispersion and Focusing on the Production of Optical Harmonics. *Phys. Rev. Lett.* **1962**, *8*, 21–22.

(13) Clays, K.; Persoons, A. Hyper-Rayleigh Scattering in Solution. *Phys. Rev. Lett.* **1991**, *66*, 2980–2983.

(14) Hao, E. C.; Schatz, G. C.; Johnson, R. C.; Hupp, J. T. Hyper-Rayleigh scattering from silver nanoparticles. *J. Chem. Phys.* **2002**, *117*, 5963–5966.

(15) El Harfouch, Y.; Benichou, E.; Bertorelle, F.; Russier-Antoine, I.; Jonin, C.; Lascoux, N.; Brevet, P.-F. Hyper-Rayleigh Scattering from Gold Nanorods. *J. Phys. Chem. C.* **2014**, *118*, 609–616.

(16) Russier-Antoine, I.; Lee, H. J.; Wark, A. W.; Butet, J.; Benichou, E.; Jonin, C.; Martin, O. J. F.; Brevet, P.-F. Second Harmonic Scattering from Silver Nanocubes. *J. Phys. Chem. C.* **2018**, *122*, 17447–17455.

(17) Russier-Antoine, I.; McLintock, A.; Wark, A. W.; Bertorelle, F.; Benichou, E.; Bergman, E.; Bruyere, A.; Jonin, C.; Brevet, P.-F. Hyper Rayleigh Scattering from Gold Nanorods: The Shape Effect for Centrosymmetric Nanoparticles. *J. Phys. Chem. C.* **2014**, *8984*, 609–616.

(18) Russier-Antoine, I.; Benichou, E.; Bachelier, G.; Jonin, C.; Brevet, P.-F. Multipolar Contributions of the Second Harmonic Generation from Silver and Gold Nanoparticles. *J. Phys. Chem. C* **2007**, *111*, 9044–9048.

(19) Agarwal, G. S.; Jha, S. S. Theory of second harmonic generation at a metal surface with surface plasmon excitation. *Solid. State. Commun.* **1982**, *41*, 499–501.

(20) Hua, X. M.; Gersten, J. I. Theory of second-harmonic generation by small metal spheres. *Phys. Rev. B.* **1986**, *33*, 3756–3764.

(21) Östling, D.; Stampfli, P.; Bennemann, K. H. Theory of nonlinear optical properties of small metallic spheres. *J. Phys. D. Atom. Mol. Clusters.* **1993**, *28*, 169–175.

(22) Martorell, J.; Vilaseca, R.; Corbalán, R. Second harmonic generation in a photonic crystal. *Appl. Phys. Lett.* **1997**, *70*, 702–704.

(23) Dadap, J. I.; Shan, J.; Eisenthal, K. B.; Heinz, T. F. Second-Harmonic Rayleigh Scattering from a Sphere of Centrosymmetric Material. *Phys. Rev. Lett.* **1999**, *83*, 4045–4048.

(24) Bachelier, G.; Russier-Antoine, I.; Benichou, E.; Jonin, C.; Brevet, P.-F. Multipolar second-harmonic generation in noble metal nanoparticles. *J. Opt. Soc. Am. B.* **2008**, *25*, 955–960.

(25) Duboisset, J.; Brevet, P.-F. Second Harmonic Scattering Defined Topological Classes for Nano-Objects. *J. Phys. Chem. C.* **2019**, *123*, 25303−25308.

(26) Russier-Antoine, I.; Duboisset, J.; Bachelier, G.; Benichou, E.; Jonin, C.; Del Fatti, N.; Vallee, F.; Sanchez-Inglesias, A.; Pastoriza-Santos, I.; Liz-Marzan, L. M.; Brevert, P. F.; et al. Symmetry Cancellations in the Quadratic Hyperpolarizability of Non-Centrosymmetric Gold Decahedra. *J. Phys. Chem. Lett.* **2010**, *1*, 874−880.

(27) Singh, A. K.; Senapati, D.; Neely, A.; Kolawole, G.; Hawker, C.; Ray, P. C. Nonlinear optical properties of triangular silver nanomaterials. *Chem. Phys. Lett.* **2009**, *481*, 94−98.

(28) Jain, B.; Srivastava, A. K.; Uppal, A.; Gupta, P. K.; Das, K. NIR Femtosecond Laser Induced Hyper-Rayleigh Scattering and Luminescence from Silver Nanoprisms. *J. Nanosci. Nanotechnol.* **2010**, *10*, 5826−5830.

(29) Hendel, T.; Wuithschick, M.; Kettemann, F.; Birnbaum, A.; Rademann, K.; Polte, J. In Situ Determination of Colloidal Gold Concentrations with UV-Vis Spectroscopy: Limitation and Perspectives. *Anal. Chem.* **2014**, *86*, 11115−11124.

(30) Olesiak-Banska, J.; Gordel, M.; Kolkowski, R.; Matczyszyn, K.; Samoc, M. Third-Order Nonlinear Optical Properties of Colloidal Gold Nanorods. *J. Phys. Chem. C.* **2012**, *116*, 13731−13737.

(31) Duboisset, J.; Matar, G.; Russier-Antoine, I.; Benichou, E.; Bachelier, G.; Jonin, C.; Ficheux, D.; Besson, F.; Brevet, P.-F. First Hyperpolarizability of the Natural Aromatic Amino Acids Tryptophan, Tyrosine, and Phenylalanine and the Tripeptide Lysine-Tryptophan-Lysine Determined by Hyper-Rayleigh Scattering. *J. Phys. Chem. B.* **2010**, *114*, 13861−13865.

(32) Minh Ngo, H.; Diep Lai, N.; Ledoux-Rak, I. High second-order nonlinear response of platinum nanoflowers: the role of surface corrugation. *Nanoscale.* **2016**, *8*, 3489−3495.

(33) Nappa, J.; Revillod, G.; Russier-Antoine, I.; Benichou, E.; Jonin, C.; Brevet, P.-F. Electric dipole origin of the second harmonic generation of small metallic particles. *Phys. Rev. B.* **2005**, *71*, 165407.

(34) Butet, J.; Bachelier, G.; Russier-Antoine, I.; Jonin, C.; Benichou, E.; Brevet, P.-F. Interference between Selected Dipoles and Octupoles in the Optical Second-Harmonic Generation from Spherical Gold Nanoparticles. *Phys. Rev. Lett.* **2010**, *105*, 077401.

(35) Revillod, G.; Russier-Antoine, I.; Benichou, E.; Jonin, C.; Brevet, P.-F. Investigating the Interaction of Crystal Violet Probe Molecules on Sodium Dodecyl Sulfate Micelles with Hyper-Rayleigh Scattering. *J. Phys. Chem. B.* **2005**, *109*, 5383−5387.

(36) Brasselet, S.; Zyss, J. Multipolar molecules and multipolar fields: probing and controlling the tensorial nature of nonlinear molecular media. *J. Opt. Soc. Am. B.* **1998**, *15*, 257−288.

(37) Nappa, J.; Russier-Antoine, I.; Benichou, E.; Jonin, C.; Brevet, P.-F. Second harmonic generation from small gold metallic particles: From the dipolar to the quadrupolar response. *J. Chem. Phys.* **2006**, *125*, 184712.

(38) Balla, N. K.; Yew, E. Y. S.; Sheppard, C. J. R.; So, P. T. C. Coupled and uncoupled dipole models of nonlinear scattering. *Opt. Express.* **2012**, *20*, 25834−25842.

Adverse Role of Shape and Size in Second Harmonic Scattering from Gold Nanoprisms

SUPPORTING INFORMATION

Krzysztof Nadolski[1,2], Emmanuel Benichou[1], Nina Tarnowicz-Staniak[2], Andrzej Żak[3], Christian Jonin[1], Katarzyna Matczyszyn[2,*], Pierre-François Brevet[1,*]

[1]Institut Lumière Matière, University of Lyon, UMR 5306 CNRS and Université Claude Bernard Lyon 1, Villeurbanne, France.

[2]Advanced Materials Engineering and Modelling Group, Wroclaw University of Science and Technology, Wroclaw, Poland.

[3]Electron Microscopy Laboratory, Faculty of Mechanical Engineering, Wroclaw University of Science and Technology, Wroclaw, Poland.

* corresponding authors: katarzyna.matczyszyn@pwr.edu.pl, pfbrevet@univ-lyon1.fr

Synthesis and characterization. *Chemicals.* All chemicals were commercially available and used without further purification. Gold(III) chloride trihydrate ($HAuCl_4 \cdot 3H_2O$), cetyltrimethylammonium chloride (CTAC), cetyltrimethylammonium bromide (CTAB), sodium borohydride ($NaBH_4$), L-Ascorbic acid (AA), sodium hydroxide (NaOH), potassium iodide (KI) and sodium iodide (NaI) were purchased from Sigma-Aldrich. Deionized water (Millipore Milli-Q grade, MQ) with resistivity of 18.2 MΩ·cm was used in all experiments.

Synthesis. Gold nanoprisms (sample #26, average edge length of 26 nm) were synthesized according to the literature protocol. [1] Briefly, to the solution containing 1.6 ml of 0.1 M CTAC, 8 ml of MQ and 0.075 ml of 0.01 M KI, 0.08 ml of 25.4 mM $HAuCl_4$ was added, followed by addition of 0.0203 ml of 0.1 M NaOH. The solution exhibited pale yellow color. Subsequently 0.08 ml of 0.064 M AA was injected and the mixture was moderately shaken, resulting in a colorless solution. Finally, 0.01 ml of 0.1 M NaOH was added, followed by quick shaking for 1-2 s. Within 10 min, the colorless solution turned red, purple and then blue.

Gold nanoprisms (samples #61, #78 and #87 with average edge lengths of 61, 78 and 87 nm respectively) were synthesized according to a modified literature protocol. [2] Briefly, the seed solutions typically used for the synthesis of gold nanorods [3] were prepared by reduction of 0.025 ml of 0.05 M $HAuCl_4$ with 0.3 ml of 0.01 M ice-cold $NaBH_4$ in 4.7 ml an aqueous 0.1 M CTAB solution under vigorous stirring. The mixture was left for 30 min under mild stirring. Subsequently, the growth solution was prepared according to, [2] namely to 9 ml of the aqueous solution containing 0.05 M CTAB and 0.050 mM NaI, 0.250 ml of 0.01M $HAuCl_4$, 0.050 ml 0.1 M NaOH and 0.050 ml 0.1M AA were added and the solution was gently mixed resulting in a color change from orange to colorless. Finally, the seed solution was added according to the nanoprisms average edge length targeted. The seed concentration in the growth solution was used as described in [2] to obtain nanoprisms with desired geometrical parameters.

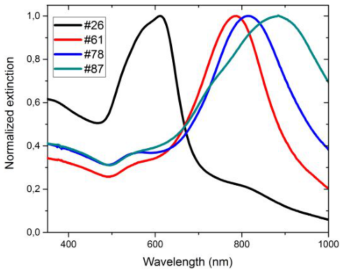

Figure S1. Normalized UV-Vis spectra of all samples.

Samples characterization. The samples were characterized by UV-Vis absorption spectroscopy and Transmission Electron Microscopy (TEM), see Figures S1 and S2(a-d) where all UV-Vis spectra and TEM images are presented.

The average values of the nanoprisms edge length were obtained from the TEM images as well as the nanoprisms content of the solutions that varied from 42% to 74% as shown in Table 1 in the manuscript, the remaining nanoparticles being assimilated as nanospheres. All data were corrected for linear absorption. Also, except for sample #26 for which the conditions are non-resonant, samples #61, #78 and #87 were performed with resonant conditions at the fundamental wavelength and non-resonant conditions at the harmonic wavelength where here resonance is considered with respect to the LSPR.

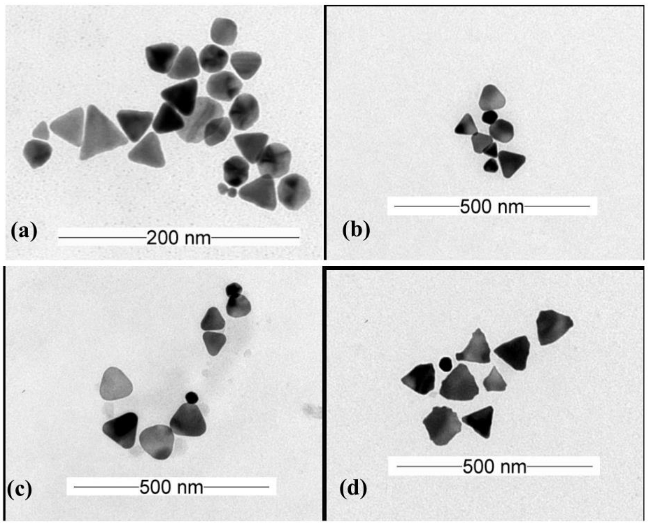

Figure S2(a-d). Transmission Electron Microscopy (TEM) pictures of samples #26 (a), #61 (b), #78 (c) and #87 (d). The deformation of edges of sample #87 is due to the surfactant centrifugation process performed prior to the screening.

Optical setup. The HRS arrangement was based on a Ti:Sapphire femtosecond laser operating at the wavelength of 800 nm with pulse length of 140 fs and repetition rate of 80 MHz. The average power was not exceeding 150 mW to avoid any sample damage. The beam was spectrally cleansed with a long-pass filter placed before it was gently focused into a fused silica cell containing the aqueous solution of nanoparticles with X10 magnification objective. The HRS intensity was collected at right angle by a single photon counting photomultiplier tube coupled with a spectrometer. A short-pass filter was inserted in the harmonic beam path in order to avoid detecting spurious light. For polarization analysis of the HRS intensity, a half-wave plate before the long-pass filter in front of the cell and an analyzer after the short-pass filter were installed on the set-up.

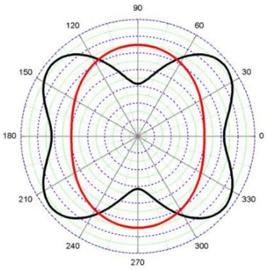

Figure S3. Theoretically simulated polar plots for 100nm edge length nanoprisms. Black represents vertically and red horizontally polarized HRS intensity respectively.

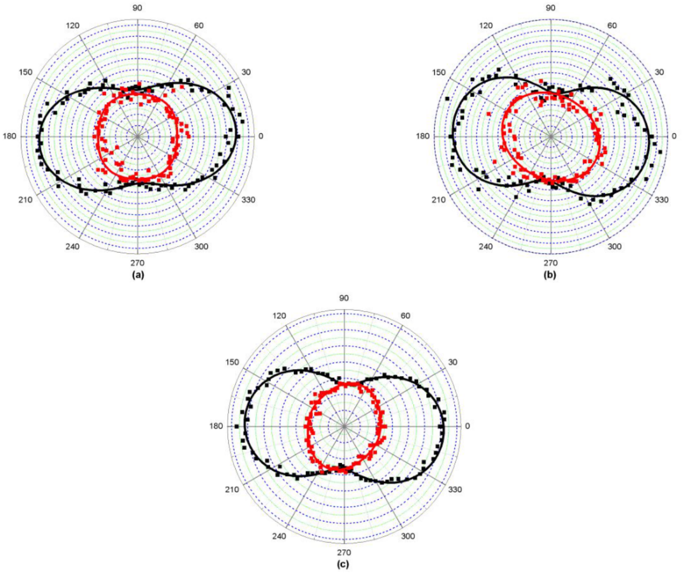

Figure S4(a-c). Polar plots of the polarization resolved HRS intensity for samples #61 (a), #78 (b) and #87 (c) and their fits using Eq.(2). Black represents vertically and red horizontally polarized HRS intensity respectively.

REFERENCES

(1) L. Chen, F. Ji, Y. Xu, L. He, Y. Mi, F. Bao, B. Sun, X. Zhang, Q. Zhang. High-Yield Seedless Synthesis of Triangular Gold Nanoplates through Oxidative Etching. *Nano Letters* **2014,** 14, (12), 7201-7206.

(2) M. R. Jones, C. A. Mirkin. Bypassing the Limitations of Classical Chemical Purification with DNA-Programmable Nanoparticle Recrystallization. *Angewandte Chemie International Edition* **2013,** 52, (10), 2886-2891.

(3) B. Nikoobakht, M. A. El-Sayed. Preparation and Growth Mechanism of Gold Nanorods (NRs) using Seed-Mediated Growth Method. *Chemistry of Materials* **2003,** 15, (10), 1957-1962.

5.3. Sensitivity of Gold Nanoparticles Second Harmonic Scattering to Surrounding Medium Change

5.3.1. Synopsis of the publication

This work was published in 2023 in the Journal of Molecular Liquids[186]. It has been divided into four parts: Introduction, Experimental, Results and Discussion and Conclusions.

In the Introduction, the authors mention the importance of gold nanoparticles in LSPR-based sensing, as well as its theoretical fundamentals. It has been mentioned, that due to the signal vs incident light intensity dependence of higher powers, the NLO is promising for sensing purposes, as had been already described in several publications. Furthermore, the HRS scattering of metallic nanoparticles has been briefly introduced. Some propositions of defining a Figure of Merit were also mentioned.

The Experimental chapter of this article describes sample preparation, UV-Vis spectroscopy and HRS setups.

Commercially available gold nanospheres of mean diameter of 40 and 100 nm were used as received, and then added different amounts of glycerol to change the surrounding medium refractive index. The study was performed for 790 and 820 nm fundamental wavelength. Since there were no significant differences, only the results for 820 nm wavelength are presented in the publication, whereas the graphs for 790 nm excitation wavelength were included in the Supporting Information file, which can be found directly after the publication in the Chapter 5.3.2.

The Results and Discussion part starts with UV-Vis spectra of pure gold nanoparticles of both sizes. Then the authors move to the HRS Intensity. The method of choice for sensing was HRS signal as such. For both nanoparticle sizes, there was a significant signal drop for the smallest addition of glycerol, whereas higher glycerol concentration resulted in minor signal changes. It was then shown, that the LSPR peak shift or, in general, any volume-dependent phenomena cannot be seen as the origin of the observed HRS signal changes, as they should be steadily decreasing then. Also the primary drop cannot be addressed to this phenomenon, since the change was much more abrupt than it could be expected in such a case. It was proposed that the signal changes are caused by changes in the vicinity of nanoparticles' surface. Next, a relatively simple model was proposed, where for small glycerol additions the first hyperpolarizability (thus, the HRS signal) exponentially decreases with the surrounding medium change, whereas for high glycerol content, it was proposed that aggregation dominates, which may be well explained by a mixture of monomers and dimers.

This was further supported by polarization-resolved HRS measurements. After a short introduction to the theoretical fundamentals, the authors showed that the depolarization ratio and retardation parameters do not exhibit any major changes, thus there are no significant symmetry changes or retardation within the sample, which additionally excludes the prevalence of volume-dependent phenomena. Note that all polar graphs were presented in the Supporting Information file. To sum up, the HRS response is highly modified after an addition of low glycerol amounts due to changes in the vicinity of gold nanoparticles' surface. Further glycerol additions do not affect the outcome very much, when the aggregation dominates. Finally, a Figure of Merit was proposed for the method of choice, i.e. HRS signal.

In the Conclusions section, it was underlined that the HRS signal-based sensing allowed for a better detection limit, compared to the UV-Vis spectroscopic methods. It was also mentioned that even though 100 nm nanoparticles also remain suitable, smaller sizes should be of preference.

Last parts of the publications include the Declaration of Competing Interest, Acknowledgements and References.

5.3.2. Publication

Journal of Molecular Liquids 388 (2023) 122704

Contents lists available at ScienceDirect

Journal of Molecular Liquids

journal homepage: www.elsevier.com/locate/molliq

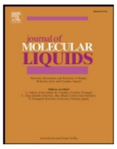

Sensitivity of gold nanoparticles Second Harmonic scattering to surrounding medium change

Krzysztof Nadolski [a,b], Christian Jonin [a], Estelle Salmon [a], Zacharie Behel [a], Katarzyna Matczyszyn [b,*], Pierre-François Brevet [a,*]

[a] *Institut Lumière Matière, Université Claude Bernard Lyon 1, CNRS UMR 5306, Villeurbanne, France*
[b] *Institute of Advanced Materials, Wroclaw University of Science and Technology, Wroclaw, Poland*

ARTICLE INFO

Keywords:
Gold nanoparticles
Nonlinear optics
Second harmonic scattering
Refractive index
Sensing

ABSTRACT

Gold nanoparticles are widely used in sensing, notably in colorimetry-based methods, where a color change is associated to the Surface Plasmon Resonance peak shift due to a binding event or an environment modification in the vicinity of the nanoparticles. In this work, we explore the sensitivity of the Second Harmonic response from gold nanoparticles of two different diameters as this response stems principally from the nanoparticle surface at small sizes as opposed to the whole volume of the nanoparticle at larger sizes. The origin of this response is therefore different from that involved in the colorimetric response, the latter being of volume origin. Upon addition of Glycerol to an aqueous solution of nanoparticles, Surface Plasmon Resonance peak shifts are first observed but they cannot fully explain the Second Harmonic intensity changes recorded. Hence, in order to gain further insights into the origin of the changes observed in the experimental data, polarization-resolved Second Harmonic measurements are performed. A mechanism where first a modification of the first hyperpolarizability of the nanoparticles due to the presence of glycerol occurs followed by nanoparticle aggregation is then proposed. The potential alternative use of this nonlinear optical method of Second Harmonic scattering for sensing purposes is then discussed in light of a figure of merit proposed to describe the sensing sensitivity observed.

1. Introduction

Sensitive and quantitative detection of chemical or biological compounds is currently of utmost importance in many applications, from biomedical or forensic sciences to environmental studies. Among the diverse methods available to date, gold nanoparticles (AuNPs) based sensors are attracting a lot of attention due in particular to the AuNPs properties like high surface-to-volume ratio or tunable optical properties [1–3]. These properties can be easily tailored through changes of the AuNPs size or shape in view of the sensor applications targeted [4,5]. Among the different methods involving AuNPs, optical ones have retained a lot of attention as they enable simple experimental designs. AuNPs exhibit Localized Surface Plasmon Resonances (LSPR) resulting from the interaction of the incident light with the conduction band electrons [6]. Hence, colorimetric methods based on linear optical extinction have been proposed with success [7–10]. Such LSPR based sensing methods rely on the spectral properties of the LSPR and the ability to modify them through the sensing process, in particular through a change of the surrounding medium refractive index [11].

Within this context of sensing, nonlinear optics based sensors are promising owing to the dependence of the sensor response to higher powers of the incident light intensity as opposed to the above described linear optical methods like extinction and scattering, where the response is linear with the incident light intensity [12]. For instance, Third Harmonic Generation (THG), namely the conversion of three photons into a single photon at the sum energy, has yielded in simple plasmonic antennas limits of detection of the order of $\Delta n \approx 10^{-3}$ where Δn is the surrounding medium refractive index change [13,14]. Also, the nonlinear optical response stems from the surface as opposed to the volume for even order nonlinear processes. A greater sensitivity is thus expected along with better limits of detection in the latter case. Therefore, Second Harmonic Generation (SHG), the quadratic nonlinear optical phenomenon whereby two incident photons are annihilated and a single photon at the sum energy emitted is attracting interest due to its inherent surface origin when performed with gold nanoparticles (AuNPs) [14,15]. In its most simple design, the SHG signal is scattered

---

* Corresponding authors.
E-mail addresses: katarzyna.matczyszyn@pwr.edu.pl (K. Matczyszyn), pfbrevet@univ-lyon1.fr (P.-F. Brevet).

https://doi.org/10.1016/j.molliq.2023.122704
Received 21 April 2023; Received in revised form 16 July 2023; Accepted 27 July 2023

from an AuNPs aqueous suspension, a phenomenon called Hyper Rayleigh Scattering (HRS). It has been widely described for Au spheres, rods or prisms [16–18] for NPs sizes ranging from 150 nm down to 2.5 nm and Au nanoclusters where the LSPR vanishes due to the loss of the metallic character [19]. However, it is though of utmost importance to assess the exact origin of the HRS response because competing processes may dominate instead of the expected surface response. This is the case of aggregation that can occur when the stability of the nanoparticles suspension is broken. Similarly to colorimetric methods, HRS sensing can still be based on the LSPR spectral shift. In this case, the gain lies in the power dependence of the observed intensity with the LSPR spectral shift. The HRS intensity remains nevertheless weak. A possibility is thus to define a figure-of-merit (FoM) less prone to intensity fluctuations [3,20]. The latter can be defined as the ratio between the sensitivity, namely the LSPR shift in nanometers divided by the refractive index change and the full width at half maximum (FWHM) as proposed by Sherry et al. [21]. It has been shown that sensing based on multipolar LSPR resonant SHG can already enhance the sensitivity but that the above defined FoM allows to identify an optimal size for the spherical nanoparticles depending on the material, gold or silver for instance [22].

In the present work, the potential for sensing of AuNPs in the context of HRS is investigated further using a water-glycerol mixture as the surrounding medium. The standard right-angle HRS configuration is used and the study is devoted to the intensity and polarization analysis of the response. The first part of our study focuses on the mechanisms involved as glycerol is introduced into an aqueous suspension of gold nanoparticles and the origin of the response is assessed. In particular, the role of nanoparticle surface changes and aggregation are discussed as well as the role of the LSPR spectra shift in the HRS intensity and polarization changes. In the second part, the sensitivity to the refractive index change is discussed in view of sensing purposes. Two gold nanoparticle sizes were selected, namely 40 nm and 100 nm diameter nanoparticles. The smaller 40 nm nanoparticles are expected to possess a nonlinearity of surface origin whereas the larger 100 nm ones are expected to have a dominant volume origin for their nonlinearity [14,18].

2. Experimental

Citrate stabilized AuNPs with a mean diameter of 40 and 100 nm were purchased (BBI Solutions) and used as received. To change the refractive index, water-glycerol mixtures were prepared from ultra-pure water (MilliQ Millipore, resistivity 18 MΩ) and glycerol (Archem Sp. z o. o.). The solution refractive index was measured on an Abbe refractometer for the sodium D-line at $\lambda = 589$ nm. The UV–Visible extinction spectra were measured on a standard spectrophotometer (Jasco, model V670).

The Hyper Rayleigh Scattering setup has been described elsewhere [14]. Briefly, the laser beam of a Ti:Sapphire femtosecond laser operating at the wavelength of 820 nm with pulse length of about 140 fs and repetition rate of 80 MHz was gently focused with a X16 objective into the fused silica cell. A low bandpass filter was placed prior to the objective to remove any unwanted SHG light generated prior to the cell. The average input power was kept at about 300 mW. The SHG intensity was collected at right angle with a CCD camera placed after a spectrometer. Polarization analysis was performed with a half-wave plate and a cube polarizer to select the polarization of the scattered harmonic light, either vertically or horizontally linearly polarized, while preserving the polarization of the detected light and a second half-wave plate was placed on the fundamental beam path to select the linear input polarization angle. Long bandpass filters were placed right after the cell to remove any unwanted spurious fundamental scattered light. Absorbances were always kept low enough in order to avoid any spurious higher order nonlinear effects.

3. Results and discussion

Spherical AuNPs with two different sizes, namely 40 and 100 nm diameter, were studied to investigate the role of the NP size. Here, we have focused on spherical nanoparticles in order to perform through the two different sizes a comparison of the surface to volume origin of the nonlinearity. Other shapes are possible but would further complexify the present analysis. Different amounts of glycerol were added to the AuNPs aqueous solutions resulting in samples containing from 0 up to 75 vol% of glycerol. Because the solutions were purchased as aqueous suspensions and to prevent a too large dilution of the nanoparticles, 75 vol% of glycerol was chosen as the upper limit for the glycerol content. A simple analysis of the optical index as a function of the glycerol content with the Lorentz-Lorenz equation underlined the ideality of the mixed water-glycerol system within the range of glycerol volume content studied, see Figure S1 in Supplementary File [23]. The UV–Visible extinction spectra were collected to observe the red-shift of the LSPR peak along with the extinction increase on the red side of the spectra as the glycerol content increases, resulting in a change of the solvent refractive index, see Fig. 1(a),(b). As expected, the position of the LSPR peak red-shifted linearly with increasing glycerol content as the refractive index of the solution increased, see Figures S2(a)–(d). Also, for the 40 nm diameter gold nanoparticles, aggregation is observed through the increase of the extinction cross-section at 800 nm, a feature not so prominent for 100 nm diameter gold nanoparticles due to the broadening of the LSPR for this nanoparticle size hiding this phenomenon. No change in cross-section is observed at the harmonic wavelength, neither 395 nm nor 410 nm, for 40 nm diameter gold nanoparticles whereas a weak change occurs for 100 nm diameter ones, a small decrease around 400 nm and a small increase at the fundamental wavelength of 800 nm.

The HRS intensity from the different AuNPs sample solutions was then collected for the 790 nm and 820 nm fundamental wavelengths, resulting in an HRS wavelength at 395 nm and 410 nm respectively, see Fig. 2(a),(b) for the two nanoparticle diameters of 40 nm and 100 nm. The intensity was renormalized for the nanoparticle content as glycerol addition into the aqueous AuNPs solutions leads to dilution. This renormalization procedure did not signficantly affect the observed features in Fig. 2(a),(b) but was deemed necessary for further quantitative analysis. No significant differences in intensity behaviour were observed between the two 790 nm and 820 nm fundamental wavelengths. Results at 820 nm are therefore exhibited below, see Supplementary Information file Figures S3(a),(b), for data collected at 790 nm fundamental wavelength.

From the observed HRS intensity, three main features are observed. First, a sharp decrease of the HRS intensity is observed at extremely small glycerol content followed by a recovery as the glycerol content increases. These two features are observed for both the 40 nm and 100 nm diameter gold nanoparticles whereas a third feature is observed for 100 nm diameter nanoparticles, namely a decrease of the HRS intensity when the glycerol volume fraction gets larger than that of water. To rationalize these features into physical mechanisms, the role of the LSPR peak shift must be discussed beforehand. The SHG response from small metallic nanoparticles like gold or silver nanoparticles can be described within the Mie theory. In this context, the response essentially stems from the nanoparticle surface but local fields and their associated Mie resonances must be taken into account. Electric dipole E1 and quadrupole E2 resonances associated to the corresponding modes must be considered [22–25]. The pure electric dipole and quadrupole responses, respectively I_D and I_Q, are of the following form [25]:

$$I_D = \kappa|\beta_D|^2\left[\frac{1}{\varepsilon_{Au}(410nm) + 2\varepsilon_s}\right]^2\left[\frac{1}{\varepsilon_{Au}(820nm) + 2\varepsilon_s}\right]^4 \tag{1a}$$

$$I_Q = \kappa|\beta_Q|^2\left[\frac{1}{2\varepsilon_{Au}(410nm) + 3\varepsilon_s}\right]^2\left[\frac{1}{\varepsilon_{Au}(820nm) + 2\varepsilon_s}\right]^4 \tag{1b}$$

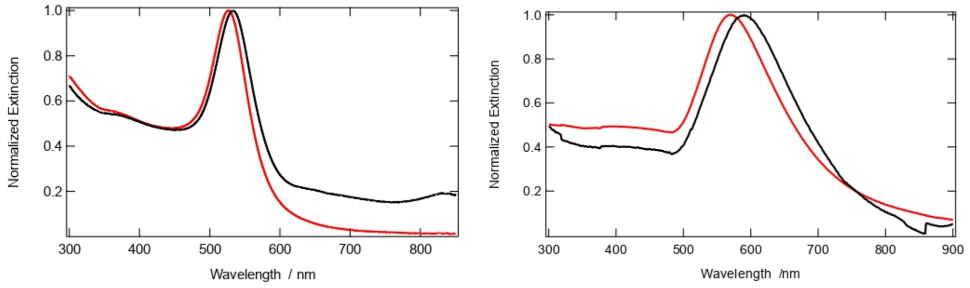

(a) (b)

Fig. 1. Normalized UV–Visible extinction spectra for (a) 40 nm and (b) 100 nm AuNPs nanosphere diameter for two different glycerol percent fraction, (red) pure water solution, (black) 2/3 glycerol volume fraction.

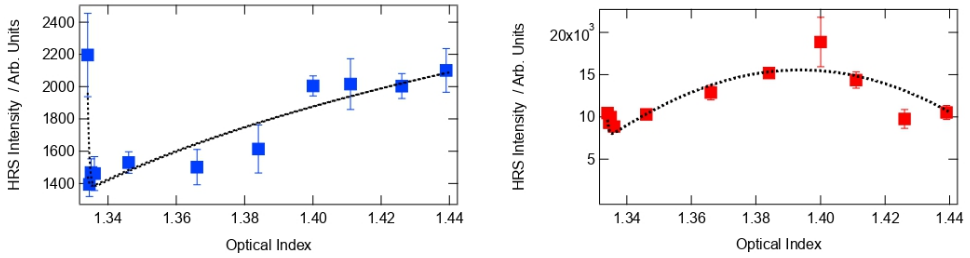

(a) **(b)**

Fig. 2. HRS intensity measured at 820 nm fundamental wavelength for (a) 40 nm and (b) 100 nm spherical AuNPs dispersed in water-glycerol mixtures with different glycerol additions. HRS intensities are renormalized for nanoparticles concentration. (Black dashed): adjusted curve using the model described below.

where β_D and β_Q are two parameters scaling the nanoparticle surface response and ε_{Au} and ε_s are the dielectric constants of gold [26] and the water-glycerol solvent. The constant κ accounts for all other parameters except the local field factors, strongly refractive index dependent, that are made explicit. In principle, β_D and β_Q are identical, both stemming from the AuNPs surface response. Note that in Eq. (1b), only the quadrupole response at the harmonic frequency is considered as the latter is susceptible to resonance enhancement due to the proximity of the harmonic wavelength with the electric quadrupole resonance wavelength. Fig. 3 shows the evolution of the dipolar and quadrupolar responses I_D and I_Q with respect to the refractive index of the surrounding medium, plotted according to Eqs. (1a),(1b). It appears that both I_D and I_Q intensities are slowly decreasing over the whole range of the glycerol-water mixture refractive index whereas the HRS experiments exhibit the reverse, see Fig. 2, and at least partially for the 100 nm diameter AuNPs. Thus, it is concluded that the change of the refractive index of the surrounding medium is not responsible for the observed experimental behaviour, except possibly for the 100 nm diameter AuNPs at refractive indices larger than 1.40. It is also noted that at very low glycerol contents, the drop in HRS intensity is abrupt as opposed to the general behaviour observed over the whole range of the refractive index change. The latter drop is therefore not related to the refractive index change either.

Hence, to explain the behaviour observed experimentally, the following mechanisms are introduced, in line with previous works [27]. First, at very low glycerol content, it is expected that the surface

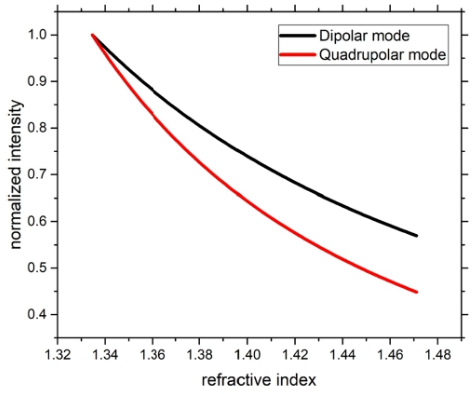

Fig. 3. Normalized theoretical (black) dipolar and (red) quadrupolar response to the SHG intensity as a function of the refractive index change of the mixed water-glycerol solvent.

hyperpolarizability of the nanoparticles is modified according to the following law:

$$\beta_m = \beta_{0m} + \Delta\beta e^{-\alpha|n-n_W|} \tag{2}$$

where the second term is the change of the surface hyperpolarizability with the glycerol content through the solution optical index n, whereas that of neat water is n_W, and β_{0m} and $\beta_{0m} + \Delta\beta$ are the first hyperpolarizability of a gold nanoparticle in glycerol and water respectively. An exponential decrease scaling with the parameter α is introduced in an ad-hoc fashion in order to distinguish the local changes at the nanoparticle surface at very low glycerol content as compared to the solvent optical index changes effectively accounted for with the above Eqs. (1a),(1b) and Fig. 3. The local glycerol interaction with the nanoparticle surface saturates at high enough glycerol content. Second, and in agreement with the increase of extinction for the 40 nm diameter nanoparticles around 800 nm, see Fig. 1(a), slow aggregation is observed. The latter phenomenon is described with an equilibrium constant between nanoparticle monomers and dimers with an equilibrium constant, the scaling of which is linearized with respect to the solution optical index due to the rather weak aggregation strength. As a result, the HRS intensity is given by:

$$I_{HRS} = G\left[N_m\langle\beta_m^2\rangle + N_d\langle\beta_d^2\rangle\right] \tag{3}$$

In Eq. (3), N_m and N_d are the monomer and dimer concentrations and $\langle\beta_m^2\rangle$ and $\langle\beta_d^2\rangle$ the square of their first hyperpolarizability averaged over all orientations and G is a general parameter incorporating all other physical constants. We underline here the fact that these nanoparticles cannot be considered as perfect sphere and therefore the orientational averaging is required. Furthermore, the $\langle\beta_d^2\rangle$ dimer hyperpolarizability is assumed constant because the local interactions with glycerol only occur at very low glycerol content when aggregation is negligible. Finally, the total number of nanoparticles is taken constant. With this rather simple model, the experimental data are well described, see adjusted curves in Fig. 2(a),(b), except at high glycerol content for the 100 nm diameter nanoparticles. In this range of glycerol content, it is expected that aggregation further proceeds towards larger aggregates with the net result of the HRS intensity decrease. This feature suggests that larger aggregates have a much smaller hyperpolarizability as compared to smaller ones, once normalized per nanoparticle in the aggregate. Saturation of this hyperpolarizability has already been observed in pyridine induced aggregation [28]. Note that considering the monomer–dimer and larger aggregates equilibria only greatly simplifies a problem where multiple nanoparticle aggregates equilibria are certainly involved.

To get a deeper insight into the HRS response of the AuNPs with respect to the surrounding medium change, polarization-resolved measurements were also conducted. To perform these studies, an analyzer was placed prior to the detection system. All polar plots are included in the Supporting Information file, see Figures S4 and S5 for the 40 nm and 100 nm diameter respectively. A full analysis was performed in order to extract a quantitative analysis from the data. The graphs were adjusted with the following expression for the HRS intensity I^X [14,29]:

$$I^X = a^X\cos^4\gamma + b^X\cos^2\gamma\sin^2\gamma + c^X\sin^4\gamma \tag{4}$$

where X stands for H (horizontal, i.e. parallel to the plane of scattering) or V (vertical, i.e. perpendicular to the plane of scattering) output polarization, a^X, b^X and c^X are three intensity parameters and γ is the polarization angle of the fundamental wavelength field. All intensity parameters are of the form of Eq. (3) where distinct hyperpolarizability tensor elements have to be considered depending on the output polarization and the fundamental input polarization angle γ. Analysis of the polarization plots allows to introduce specific parameters, using the intensity parameters obtained with the adjustment procedure of the two perpendicular polarization experimental data with Eq. (4). The depolarization ratio, D^V, is defined as [14]:

$$D^V = c^V/a^V \tag{5}$$

whereas the retardation parameters ζ^V and ζ^H are introduced as follows [18,29,30]:

$$\zeta^V = \left(b^V - a^V - c^V\right)/b^V \tag{6a}$$

$$\zeta^H = \left(a^H - c^H\right)/\left(a^H + c^H\right) \tag{6b}$$

The depolarization ratio provides an insight into the nature of the HRS response of the NPs as it weights the dipolar and octupolar contributions to the HRS response within the context of the irreducible representation of the first hyperpolarizability tensor [31]. On the opposite, the two ζ^V and ζ^H parameters provide a measure of the extent of retardation in the response. Retardation describes the evolution of the spatial phase over the nanoparticle size. Hence, size will lead to values of these parameters deviating from zero whereas deviation from a centrosymmetric shape decreases these parameters as it enhances the surface local nonlinearity. The dependence of these three parameters with the refractive index is depicted in Fig. 4(a)–(f). Uncertainties were calculated by the exact differential method using uncertainties from the adjustment of the experimental data with Eq. (4). Polar graphs and their fits to Eq. (4) are provided in the Supporting Information file, Figures S4 (a)–(j), S5(a)–(v).

For the 40 nm diameter AuNPs, the depolarization ratio D^V remains in the range 0.30–0.40 indicating a rather similar contribution from the dipolar and octupolar irreducible tensor contributions [27]. These values are rather similar to what has been observed for AuNPs with similar sizes. Adjustment of the experimental depolarization ratio D^V is then achieved with the above model for the HRS intensity as a function of the glycerol-water mixture optical index, with account of the selection of the hyperpolarizability tensor elements of the monomers and aggregates with the output polarization selection. On the opposite, the 100 nm diameter AuNPs exhibit an almost purely octupolar response with a D^V coefficient close to 2/3. Retardation parameters ζ^V and ζ^H do not take large values for 40 nm diameter AuNPs as expected, only for the 100 nm diameter ones do they take large values, also in line with previous works [28]. As a result, marked changes only appear at small glycerol additions on the HRS intensity and are more visible for the 40 nm diameter AuNPs. For larger glycerol additions, changes in the parameters are rather smooth and weak. Similar behaviour was observed for 790 nm excitation wavelength, see Supplementary Information file, Figures S6(a), (b). It appears therefore that glycerol at very low content is sufficient to modify the HRS response at the surface of the AuNPs. This effect is more prominent for the smallest nanoparticles and is clearly seen on the HRS intensity plots as well as the characteristic parameters of the response. For the larger 100 nm diameter AuNPs, larger retardation contribution occurs, as seen from the larger retardation parameters. Being of higher order, this contribution scales with the size of the nanoparticles, i.e. their volume, and the surface effect is lost. The nonlinear optical surface response is therefore modified in strength and nature with the incorporation of small amounts of glycerol. The decrease of HRS intensity with almost constant depolarization coefficient indicates a change of the surface nonlinearity with minimal changes in symmetry as seen from the dipolar to octupolar contributions ratio in the context of the irreducible tensorial representation of the hyperpolarizability. This feature in particular suggests that the AuNPs surface probes localized changes. Homogeneity of the refractive index is however recovered at much larger glycerol contents [31]. The present results therefore indicate that the LSPR peak shift with the refractive index in HRS measurements from AuNPs do not play any major role in this study. Rather, the HRS response at small glycerol addition is driven by the surface contribution, especially for the smallest AuNPs. The sensitivity to the localized surface changes indicates that sensing using AuNPs in HRS measurements should be attractive especially at low refractive index changes and small AuNPs sizes. At larger glycerol content, the localized surface changes

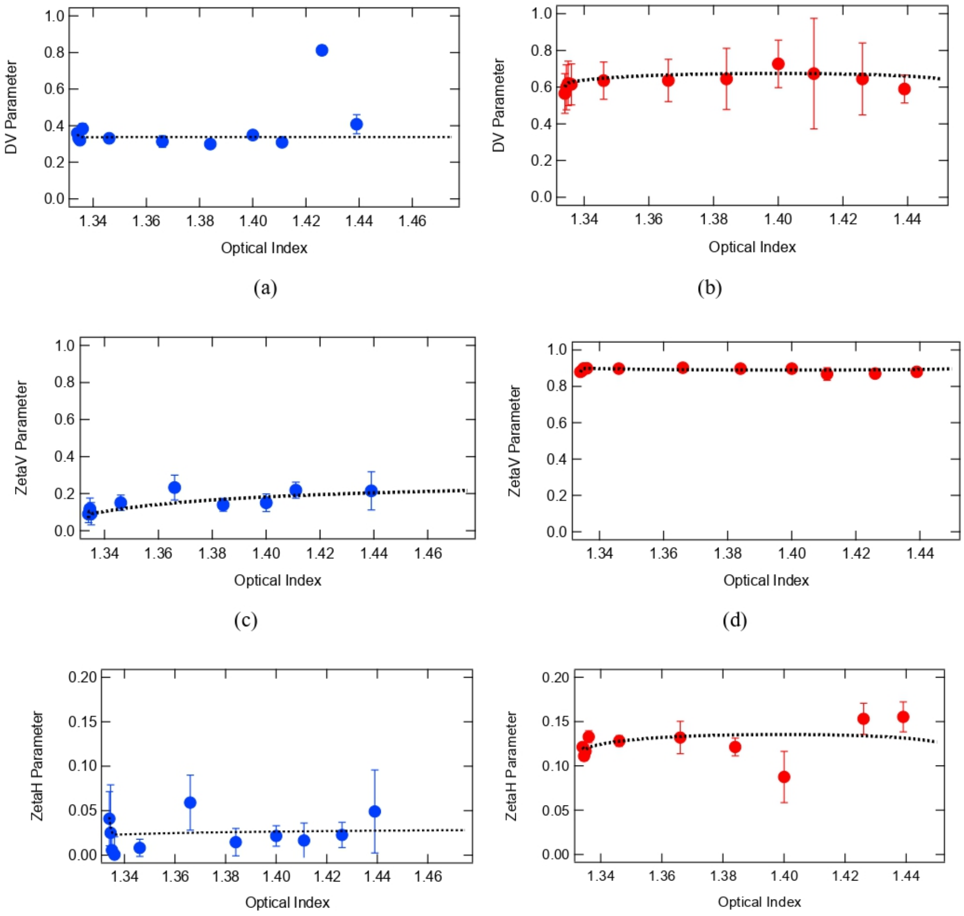

(a) (b) (c) (d) (e) (f)

Fig. 4. (a,b) Depolarization ratio and (c-d) retardation parameters for Vertically and (e-f) Horizontally polarized HRS intensity with respect to the surrounding medium refractive index for (blue; a, c, e) 40 nm and (red; b, d, f) 100 nm diameter AuNPs.

saturate and aggregation takes place with smooth increase of the HRS intensity. However, as suggested by the extinction spectra, see Fig. 1, aggregation is rather weak and therefore the retardation parameters ζ^V and ζ^H are weakly affected because aggregates remain small for 40 nm diameter nanoparticles. For 100 nm diameter nanoparticles, retardation is already too much developed with values close to 0.9 to observe clear changes.

In this respect, this study indicates that sensing with gold nanoparticles must be performed with the smaller gold nanoparticles where surface sensitivity is achieved as compared to larger 100 nm diameter ones. A FoM can thus be defined as opposed to the LSPR peak shift that may not be as adapted as expected. Rather, a FoM based on the change in the HRS intensity should be better suited. A FoM of the form $(\Delta I/I)/RIU$, free from intensity fluctuations with renormalization, may then be built where *RIU* stands for *Refractive Index Unit.* From Fig. 2(a), and using the above model adjusted on the experimental data with a first order expansion of Eq. (2) with the optical index change $n - n_W$, this *FoM* is given by:

$$FoM = \frac{(\Delta I/I)}{RIU} = 2\alpha\Delta\beta \tag{7}$$

the value of which is about 4000 considering the numerical values obtained from the model adjusted to the data. Such a *FoM* value suggests a sensitivity of the order of less than 1% in glycerol volume content considering Figure S1 linking the optical index to the volume fraction of glycerol. This analysis therefore provides a quantitative assessment of the sensing ability of smaller gold nanoparticles HRS towards small refractive index changes.

4. Conclusions

The HRS intensity of AuNPs with a 40 nm and 100 nm mean diameter dispersed in water was studied after addition of different amounts of glycerol. Marked changes are exhibited at the lowest glycerol additions before an intensity recovery, features attributed to initial local surface changes of the nanoparticle first hyperpolarizability followed by a weak aggregation. Polarization-resolved studies are performed to assess the origin and nature of the nonlinear response. For larger glycerol additions, changes are not so pronounced and rather smooth. These features are more prominent for the 40 nm diameter nanoparticles as opposed to the 100 nm diameter ones.

UV–Visible extinction based colorimetric measurements do not allow to attribute the changes at very low glycerol contents, namely below 1 vol%, to the linear wavelength shift of the SPR peak. For this purpose, the HRS method is more advantageous as it exhibits more pronounced signal changes. This property of the HRS method is due to the origin of the response stemming from the AuNPs surface at for small diameter nanoparticles as opposed to nanoparticles with larger diameter. Combined with the simplicity of the geometrical arrangements for these measurements, HRS scattering from AuNP solutions is a promising method for sensing applications. This work further indicates that rather small diameter nanoparticles must be used to avoid the detrimental contribution from retardation, still keeping large intensities, and to use the normalized HRS intensity change as a figure of merit. Further works involving more refined platforms to perform sensing have also appeared [32] but HRS remains rather simple into its development.

CRediT authorship contribution statement

Krzysztof Nadolski: Methodology, Formal analysis, Investigation, Data curation, Writing – original draft. **Christian Jonin:** Software, Investigation. **Estelle Salmon:** Software, Investigation. **Zacharie Behel:** Software, Formal analysis, Data curation. **Katarzyna Matczyszyn:** Conceptualization, Supervision, Funding acquisition. **Pierre-François Brevet:** Conceptualization, Methodology, Formal analysis, Data curation, Writing – review & editing, Supervision.

Declaration of Competing Interest

The authors declare that they have no known competing financial interests or personal relationships that could have appeared to influence the work reported in this paper.

Data availability

Data will be made available on request.

Acknowledgements

K.N. and K.M. acknowledge funding from the National Science Centre in Poland within the Harmonia DEC/2016/22/M/ST4/00275 project and funding from the National Science Centre in Poland within the Opus UMO-2019/35/B/ST4/03280 project. All authors acknowledge funding from the PPN/BFT/2019/1/00030/U/0001 PHC POLONIUM project, cofunded by the Polish National Agency For Academic Exchange and Campus France.

Appendix A. Supplementary material

Supplementary data to this article can be found online at https://doi.org/10.1016/j.molliq.2023.122704.

References

[1] L. Tessaro, A. Aquino, A.P. Azevedo de Carvalho, C.A. Conte-Junior, A systematic review on gold nanoparticles based-optical biosensors for Influenza virus detection, Sens. Actuators Rep. 3 (2021), 100060.

[2] E. Priyadarshini, N. Pradhan, Gold nanoparticles as efficient sensors in colorimetric detection of toxic metal ions: A review, Sens. Actuators B 238 (2017) 888–902.

[3] G. Liu, M. Lu, X. Huang, T. Li, D. Xu, Application of gold-nanoparticle colorimetric sensing to rapid food safety screening, Sensors 18 (12) (2018).

[4] K. Saha, S.S. Agasti, C. Kim, X. Li, V.M. Rotello, Gold nanoparticles in chemical and biological sensing, Chem. Rev. 112 (5) (2012) 2739–2779.

[5] A. Moores, F. Goettmann, The plasmon band in noble metal nanoparticles: an introduction to theory and applications, New J. Chem. 30 (2006) 1121–1132.

[6] E. Petryayeva, U.J. Krull, Localized surface plasmon resonance: nanostructures, bioassays and biosensing - a review, Anal. Chim. Acta 1 (706) (2011) 8–24.

[7] J.N. Anker, W.P. Hall, O. Lyandres, N.C. Shah, J. Zhao, R.P. Van Duyne, Biosensing with plasmonic nanosensors, Nat. Mater. 7 (2008) 442–453.

[8] C. Xie, F. Xu, X. Huang, C. Dong, J. Ren, Single gold nanoparticles counter: An ultrasensitive detection platform for one-step homogeneous immunoassays and DNA hybridization assays, J. Am. Chem. Soc. 131 (35) (2009) 12763–12770.

[9] N. Nath, A. Chilkoti, A colorimetric gold nanoparticle sensor to interrogate biomolecular interactions in real time on a surface, Anal. Chem. 74 (3) (2002) 504–509.

[10] C.-C. Chang, C.-P. Chen, T.-H. Wu, C.-H. Yang, C.-W. Lin, C.-Y. Chen, Gold nanoparticle-based colorimetric strategies for chemical and biological sensing applications, Nanomaterials 9 (6) (2019).

[11] A.A. Dormeny, P.A. Sohi, M. Kahrizi, Design and simulation of a refractive index sensor based on SPR and LSPR using gold nanostructures, Results Phys. 16 (2020).

[12] L. Bonacina, P.-F. Brevet, M. Finazzi, M. Celebrano, Harmonic generation at the nanoscale, J. Appl. Phys. 127 (2020), 230901.

[13] M. Mesch, B. Metzger, M. Hentschel, H. Giessen, Nonlinear plasmonic sensing, Nano Lett. 16 (5) (2016) 3155–3159.

[14] J. Nappa, G. Revillod, I. Russier-Antoine, E. Benichou, C. Jonin, P.F. Brevet, Electric dipole origin of the second harmonic generation of small metallic particles, Phys. Rev. B 71 (2005), 165407.

[15] L. Ghirardini, A.-L. Baudrion, M. Monticelli, D. Petti, P. Biagioni, L. Duo, G. Pellegrini, P.-M. Adam, M. Finazzi, M. Celebrano, Plasmon-enhanced second harmonic scattering, J. Phys. Chem. C 122 (21) (2018) 11475–11481.

[16] Y. El Harfouch, E. Benichou, F. Bertorelle, I. Russier-Antoine, C. Jonin, N. Lascoux, P.-F. Brevet, Hyper-Rayleigh scattering from gold nanorods, J. Phys. Chem. C 118 (2014) 609–616.

[17] E.C. Hao, G.C. Schatz, R.C. Johnson, J.T. Hupp, Hyper-Rayleigh scattering from silver nanoparticles, J. Chem. Phys. 117 (2002) 5963.

[18] K. Nadolski, E. Benichou, N. Tarnowicz-Staniak, A. Żak, C. Jonin, K. Matczyszyn, P.-F. Brevet, Adverse role of shape and size in second-harmonic scattering from gold nanoprisms, J. Phys. Chem. C 124 (2020) 14797–14803.

[19] R. Jin, C. Zeng, M. Zhou, Y. Chen, Atomically precise colloidal metal nanoclusters and nanoparticles: Fundamentals and opportunities, Chem. Rev. 116 (18) (2016) 10346–10413.

[20] S. Unser, I. Bruzas, J. He, L. Sagle, Localized surface plasmon resonance biosensing: Current challenges and approaches, Sensors 15 (2015) 15684–15716.

[21] L.J. Sherry, S.-H. Chang, G.C. Schatz, R.P. Van Duyne, B.J. Wiley, Y. Xia, Localized surface plasmonc resonance spectroscopy of single silver nanocubes, Nano Lett. 5 (10) (2005) 2034–2038.

[22] J. Butet, I. Russier-Antoine, C. Jonin, N. Lascoux, E. Benichou, P.-F. Brevet, Sensing with multipolar second harmonic generation from spherical metallic nanoparticles, Nano Lett. 12 (3) (2012) 1697–1701.

[23] J.I. Dadap, J. Shan, K.B. Eisenthal, T.F. Heinz, Second-harmonic Rayleigh scattering from a sphere of centrosymmetric material, Phys. Rev. Lett. 83 (1999) 4045.

[24] J.I. Dadap, J. Shan, T.F. Heinz, Theory of optical second-harmonic generation from a sphere of centrosymmetric material: small-particle limit, J. Opt. Soc. Am. B 21 (7) (2004) 1328–1347.

[25] J. Nappa, I. Russier-Antoine, E. Benichou, C. Jonin, P.-F. Brevet, Wavelength dependence of the retardation effects in silver nanoparticles followed by polarization resolved hyper Rayleigh scattering, Chem. Phys. Lett. 415 (2005) 246–250.

[26] P.B. Johnson, R.W. Christy, Optical constants of the noble metals, Phys. Rev. B 6 (1972) 4370.

[27] S. Brasselet, J. Zyss, Multipolar molecules and multipolar fields: probing and controlling the tensorial nature of nonlinear molecular media, J. Opt. Soc. Am. B 15 (1) (1998) 257–288.

[28] I. Russier-Antoine, E. Benichou, G. Bachelier, C. Jonin, P.-F. Brevet, Multipolar contributions of the second harmonic generation from silver and gold nanoparticles, J. Phys. Chem. C 111 (26) (2007) 9044–9048.

[29] J. Butet, G. Bachelier, I. Russier-Antoine, C. Jonin, E. Benichou, P.-F. Brevet, Interference between selected dipoles and octupoles in the optical second-harmonic generation from spherical gold nanoparticles, Phys. Rev. Lett. 105 (2010), 077401.

[30] J. Nappa, I. Russier-Antoine, E. Benichou, C. Jonin, P.-F. Brevet, Second harmonic generation from small gold metallic particles: From the dipolar to the quadrupolar response, J. Chem. Phys. 125 (2006).
[31] J. Duboisset, P.-F. Brevet, Second-harmonic scattering-defined topological classes for nano-objects, J. Phys. Chem. C 123 (41) (2019) 25303–25308.
[32] G.-C. Li, D. Lei, M. Qiu, W. Jin, S. Lan, A.V. Zayats, Light-induced symmetry breaking for enhancing second-harmonic generation from an ultrathin plasmonic nanocavity, Nat. Commun. (2021) 12.

Supplementary Information

Sensitivity of Gold Nanoparticles Second Harmonic Scattering to Surrounding Medium Change

Krzysztof Nadolski,[1,2] Christian Jonin,[1] Estelle Salmon,[1] Zacharie Behel,[1]
Katarzyna Matczyszyn,[2] Pierre-François Brevet[1*]*

[1]Institut Lumière Matière, Université Claude Bernard Lyon 1, CNRS UMR 5306, Villeurbanne, France.

[2]Institute of Advanced Materials, Faculty of Chemistry, Wroclaw University of Science and Technology, Wroclaw, Poland.

* Corresponding authors: katarzyna.matczyszyn@pwr.edu.pl, pfbrevet@univ-lyon1.fr

1. Optical Index of Water-Glycerol mixture with Glycerol content

The optical index of the different water-glycerol solutions were recorded for the sodium D-line at 589 nm and adjusted with the Lorentz-Lorenz formula, see Eq.(S1), for comparison to ideal mixing, see Figure S1.

$$\frac{n^2-1}{n^2+2} = \sum_i \phi_i \frac{n_i^2-1}{n_i^2+2} \qquad \text{(S1)}$$

where ϕ_i and n_i are the volume percent and the optical index of the components entering the mixture and n the optical index of the mixture.

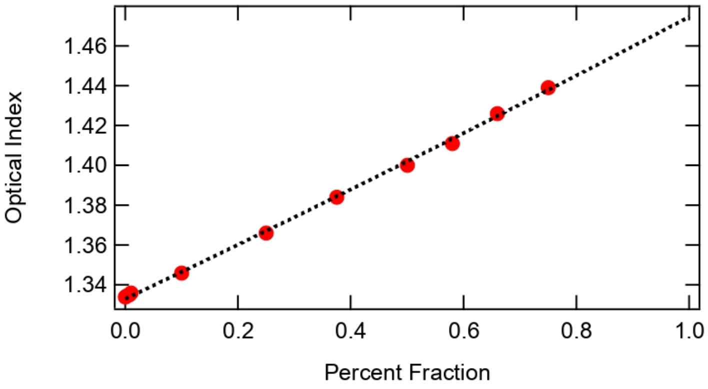

Figure S1 : Optical index of the mixed water – glycerol solvent as a function of the glycerol volume percent fraction (red disks) experimental data, (black dashed) adjustment to Eq.S1.

2. Extinction spectra of Water-Glycerol mixture with Glycerol content

Extinction spectra provided in main text where further scrutinized to analyze first the localized surface plasmon resonance (LSPR) peak wavelength shift as a function of the glycerol content.

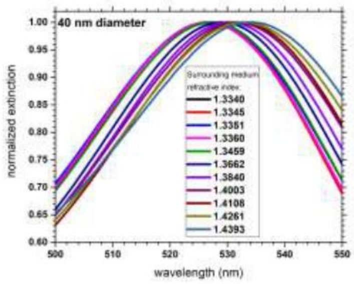

(a)

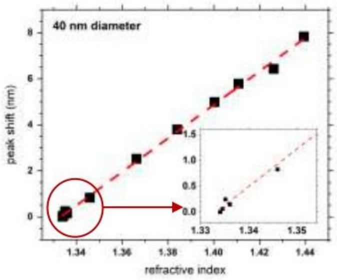

(b)

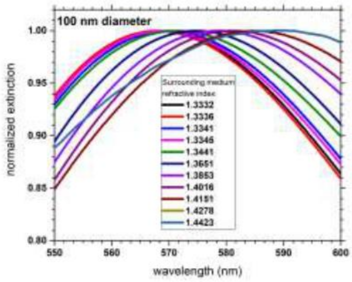

(c)

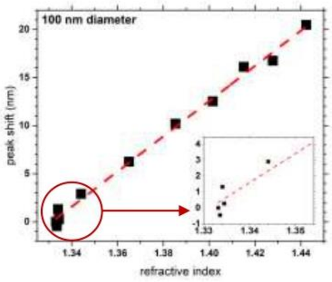

(d)

Figure S2: Change of the AuNPs water-glycerol normalized UV-Visible extinction spectra in the vicinity of the LSPR peak for (a) 40 nm and (c) 100 nm AuNPs nanosphere diameter and corresponding plots with linear adjustments of the LSPR peak shift as a function of the refractive index of the water-glycerol solutions for (b) 40 nm and (d) 100 nm AuNPs nanosphere diameter, (inserts) blow-up view at the low glycerol contents.

3. HRS Intensity measurements at 790 nm

Besides measurements performed at the 820 nm fundamental wavelength, see Figures 2 (a)-(b) main file, measurements at 790 nm were also performed and are shown below. Similar results to those recorded at 820 nm fundamental wavelength were obtained.

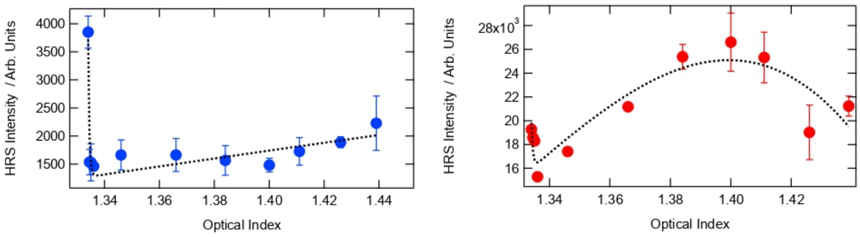

(a) (b)

Figure S3 : HRS intensity measured at 790 nm excitation for (a) 40 nm and (b) 100 nm diameter spherical AuNPs dispersed in water-glycerol mixtures with different glycerol additions. The intensities are renormalized for nanoparticles concentration. (black dashed) adjusted curve using the model described in main text.

4. Polarization resolved HRS Intensity measurements at 820 nm

Polarization resolved plots of the HRS response of the AuNPs with respect to the surrounding medium change, are presented below, see Figures S4 and S5 for the 40 nm and 100 nm diameter AuNPs respectively.

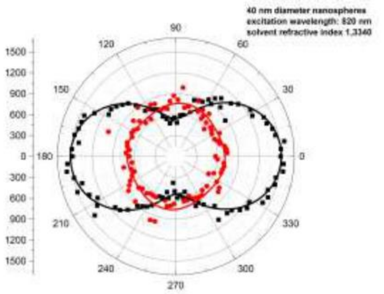

(a)

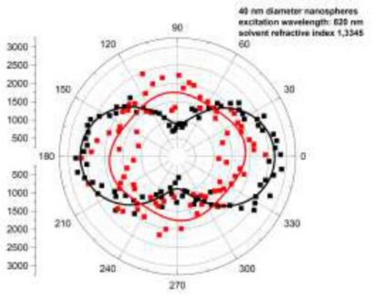

(b)

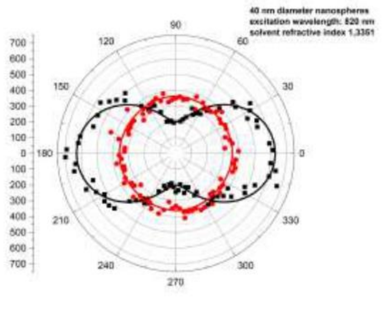

(c)

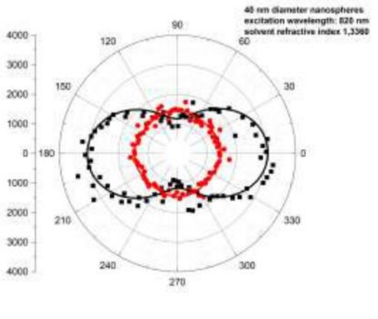

(d)

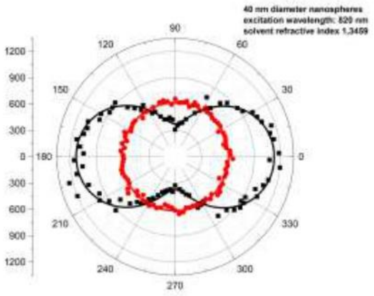
40 nm diameter nanospheres
excitation wavelength: 820 nm
solvent refractive index 1,3459
1200
900
600
300
0
300
600
900
1200
90
60
30
0
330
300
270
240
210
180
150
120

(e)

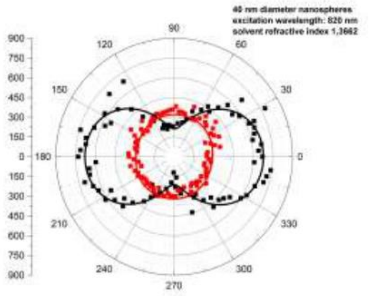
40 nm diameter nanospheres
excitation wavelength: 820 nm
solvent refractive index 1,3662
900
750
600
450
300
150
0
150
300
450
600
750
900
90
60
30
0
330
300
270
240
210
180
150
120

(f)

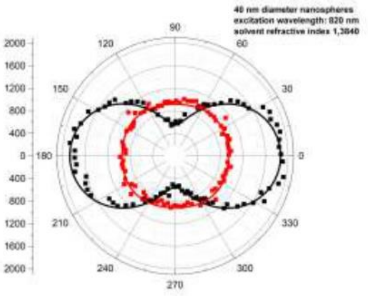
40 nm diameter nanospheres
excitation wavelength: 820 nm
solvent refractive index 1,3840
2000
1600
1200
800
400
0
400
800
1200
1600
2000
90
60
30
0
330
300
270
240
210
180
150
120

(g)

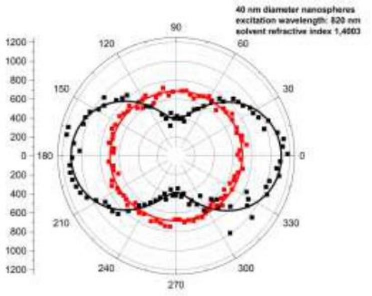
40 nm diameter nanospheres
excitation wavelength: 820 nm
solvent refractive index 1,4003
1200
1000
800
600
400
200
0
200
400
600
800
1000
1200
90
60
30
0
330
300
270
240
210
180
150
120

(h)

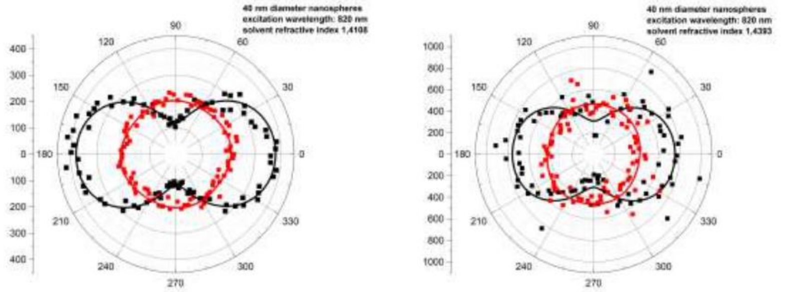

(i) (j)

Figure S4(a)-(j): Polarization-resolved graphs and their fits from Eq.(4), main text, for 40 nm mean diameter gold nanospheres. The solvent refractive indices are indicated in the graphs. (Black) vertically polarized HRS intensity, (red) horizontally polarized HRS intensity.

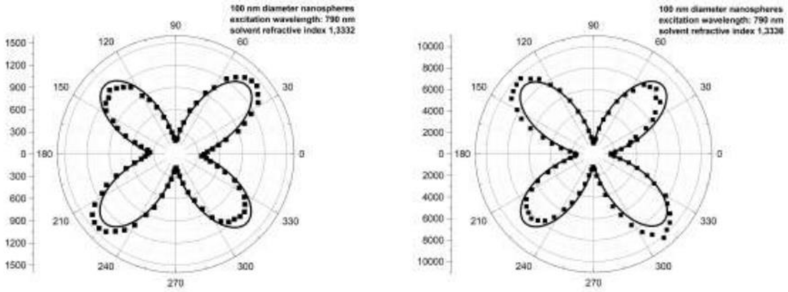

(a) (b)

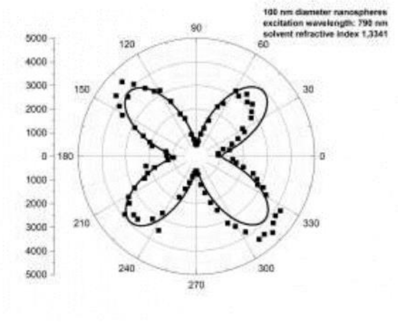
100 nm diameter nanospheres
excitation wavelength: 790 nm
solvent refractive index 1,3341
5000
4000
3000
2000
1000
0
90
60
30
0
330
300
270
240
210
180
150
120

(c)

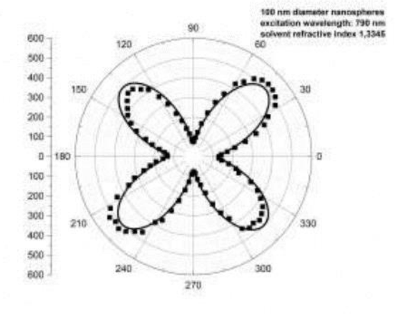
100 nm diameter nanospheres
excitation wavelength: 790 nm
solvent refractive index 1,3345
600
500
400
300
200
100
0
90
60
30
0
330
300
270
240
210
180
150
120

(d)

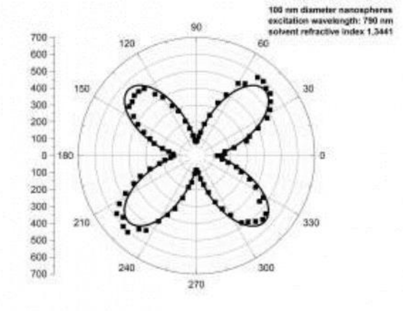
100 nm diameter nanospheres
excitation wavelength: 790 nm
solvent refractive index 1,3441
700
600
500
400
300
200
100
0
90
60
30
0
330
300
270
240
210
180
150
120

(e)

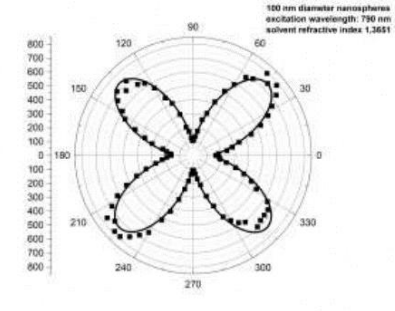
100 nm diameter nanospheres
excitation wavelength: 790 nm
solvent refractive index 1,3651
800
700
600
500
400
300
200
100
0
90
60
30
0
330
300
270
240
210
180
150
120

(f)

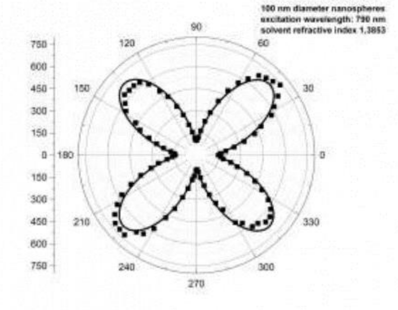
100 nm diameter nanospheres
excitation wavelength: 790 nm
solvent refractive index 1,3853
750
600
450
300
150
0
90
60
30
0
330
300
270
240
210
180
150
120

(g)

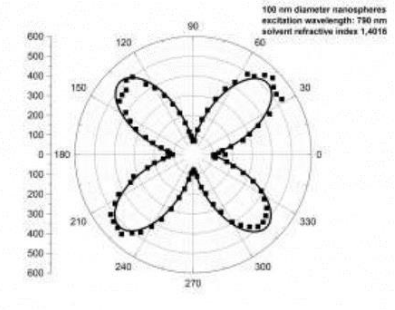
100 nm diameter nanospheres
excitation wavelength: 790 nm
solvent refractive index 1,4016
600
500
400
300
200
100
0
90
60
30
0
330
300
270
240
210
180
150
120

(h)

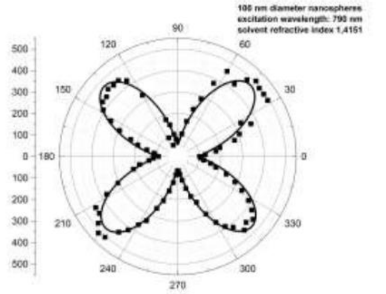
100 nm diameter nanospheres
excitation wavelength: 790 nm
solvent refractive index 1,4151
90
120
60
150
30
180
0
210
330
240
300
270
500
400
300
200
100
0
100
200
300
400
500

(i)

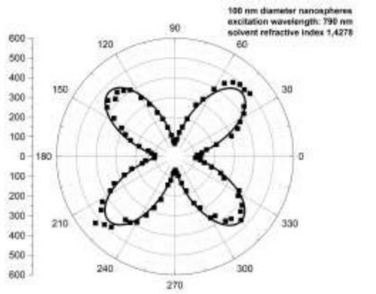
100 nm diameter nanospheres
excitation wavelength: 790 nm
solvent refractive index 1,4278
90
120
60
150
30
180
0
210
330
240
300
270
600
500
400
300
200
100
0
100
200
300
400
500
600

(j)

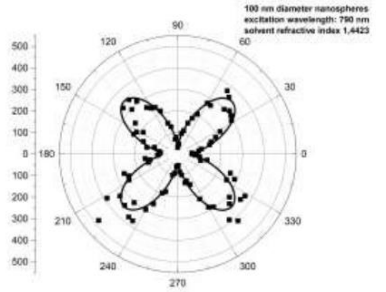
100 nm diameter nanospheres
excitation wavelength: 790 nm
solvent refractive index 1,4423
90
120
60
150
30
180
0
210
330
240
300
270
500
400
300
200
100
0
100
200
300
400
500

(k)

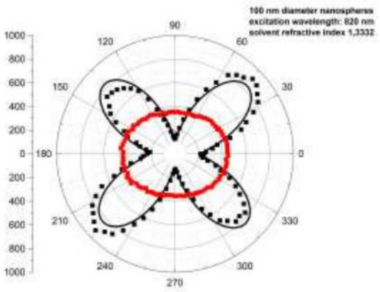
100 nm diameter nanospheres
excitation wavelength: 820 nm
solvent refractive index 1,3332
90
120
60
150
30
180
0
210
330
240
300
270
1000
800
600
400
200
0
200
400
600
800
1000

(l)

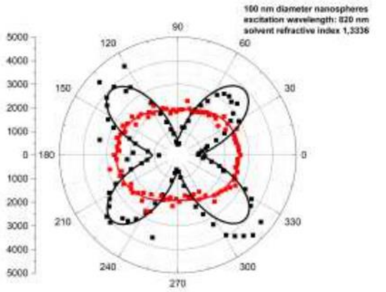
100 nm diameter nanospheres
excitation wavelength: 820 nm
solvent refractive index 1,3336
90
120
60
150
30
180
0
210
330
240
300
270
5000
4000
3000
2000
1000
0
1000
2000
3000
4000
5000

(m)

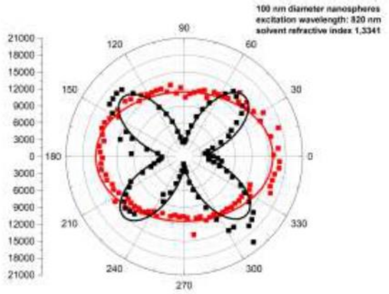
100 nm diameter nanospheres
excitation wavelength: 820 nm
solvent refractive index 1,3341
90
120
60
150
30
180
0
210
330
240
300
270
21000
18000
15000
12000
9000
6000
3000
0
3000
6000
9000
12000
15000
18000
21000

(n)

9

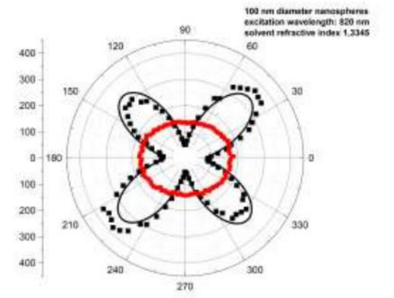
100 nm diameter nanospheres
excitation wavelength: 820 nm
solvent refractive index 1,3345
90
120
60
150
30
180
0
210
330
240
300
270
400
300
200
100
0
100
200
300
400

(o)

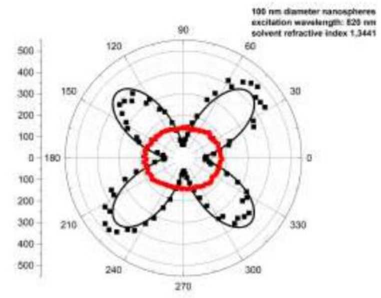
100 nm diameter nanospheres
excitation wavelength: 820 nm
solvent refractive index 1,3441
90
120
60
150
30
180
0
210
330
240
300
270
500
400
300
200
100
0
100
200
300
400
500

(p)

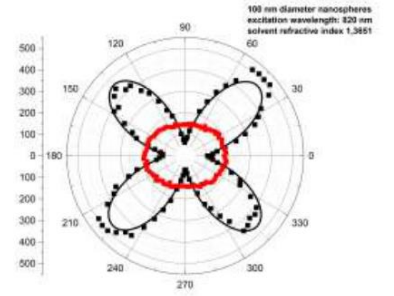
100 nm diameter nanospheres
excitation wavelength: 820 nm
solvent refractive index 1,3651
90
120
60
150
30
180
0
210
330
240
300
270
500
400
300
200
100
0
100
200
300
400
500

(q)

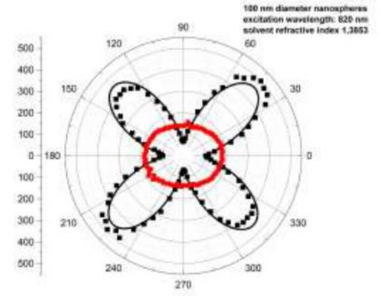
100 nm diameter nanospheres
excitation wavelength: 820 nm
solvent refractive index 1,3853
90
120
60
150
30
180
0
210
330
240
300
270
500
400
300
200
100
0
100
200
300
400
500

(r)

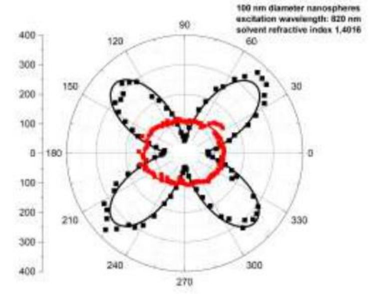
100 nm diameter nanospheres
excitation wavelength: 820 nm
solvent refractive index 1,4016
90
120
60
150
30
180
0
210
330
240
300
270
400
300
200
100
0
100
200
300
400

(s)

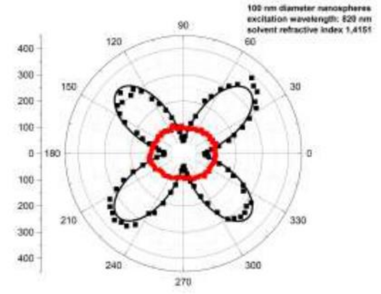
100 nm diameter nanospheres
excitation wavelength: 820 nm
solvent refractive index 1,4151
90
120
60
150
30
180
0
210
330
240
300
270
400
300
200
100
0
100
200
300
400

(t)

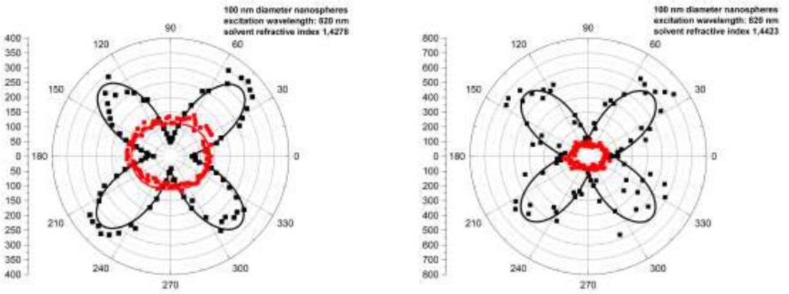

(u) (v)

Figure S5(a)-(v): Polarization-resolved graphs and their fits from Eq. (4) for 100 nm mean diameter nanospheres. The excitation wavelength and solvent refractive indices are indicated in the graphs. (Black) vertically polarized HRS intensity, (red) horizontally polarized HRS intensity.

5. Parameters of the polarization resolved HRS Intensity measurements at 790 nm fundamental wavelength

Depolarization ratio and retardation parameters were calculated (see Eqs. 5, 6(a)-(b), main text). The obtained results with respect to the surrounding medium refractive index are plotted in Figure 4 (a)-(f) for 820 nm in main text and Figure S5 (a)-(b) for 790 nm excitation wavelength, vertically-polarized signal.

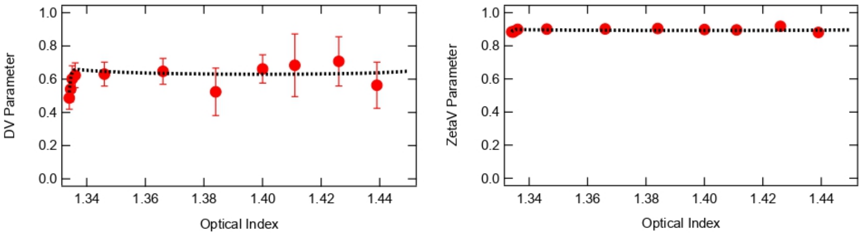

(a) (b)

Figure S6: (a) Depolarization ratio D^V and (b) retardation parameter ζ^V, as defined through Eqs. (4)-(5) obtained for 100 nm mean nanosphere diameter at excitation wavelength of 790 nm, (inserts) blow-up view at low glycerol contents.

6. Power Dependance of HRS intensity from Gold Nanoparticles

The linear dependence of the gold nanoparticles solution with the fundamental intensity was controlled. Figure S1 provides the obtained result for the smallest nanoparticles.

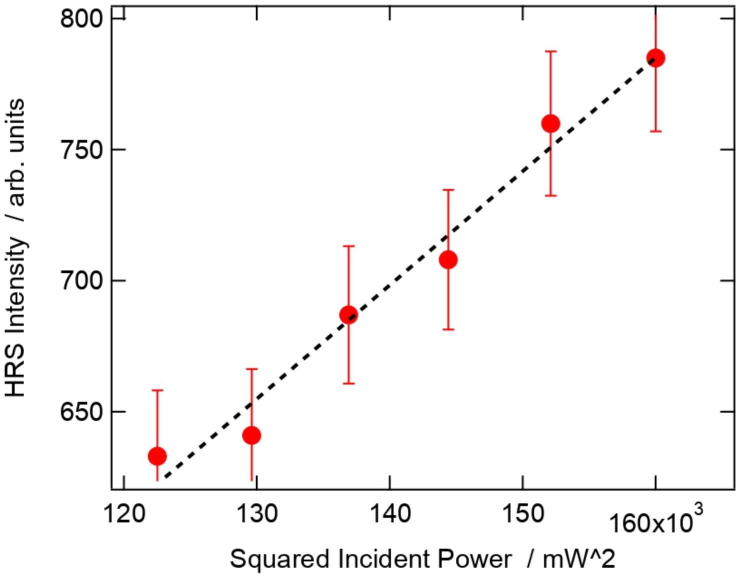

Figure S7: Dependence of the gold nanoparticles solution with the square of the fundamental intensity.

5.4. Sensing Copper (II) Ions with Hyper Rayleigh Scattering from Gold Nanoparticles

5.4.1. Synopsis of the publication

This study was published in 2023 in The Journal of Physical Chemistry C.[187] It is composed of 4 parts: Introduction, Materials and Methods, Results and Discussion and Conclusion. It concerns the application of HRS for sensing of copper (II) ions with the use of 50 nm diameter gold nanospheres.

In the Introduction part, it was shown that the detection of copper ions is crucial for different purposes, such as medicine or food safety. Then, the well-known colorimetry-based sensing method was described.

The Materials and Methods section includes a description of sample preparation. Furthermore, the setups for UV-Vis spectroscopy, DLS, Zeta potential, TEM microscopy and HRS were described.

The Results and Discussion part starts with UV-Vis spectroscopy, as a reference method. Spectra of gold nanoparticles containing from 0 to 25 mM $CuBr_2$ were presented, and the observed changes were seen in terms of primary peak shift, primary peak intensity change, as well as an appearance of additional extinction peak around 780 nm. It was shown that regardless of the considered phenomenon, the UV-Vis spectroscopy is not an appropriate method for detection of the lowest copper addition, which was 1 μM in this case.

It is followed by DLS and Zeta potential measurements, which proved that the outcome may be divided into to parts, i.e. below and over 1 mM. Below that value, changes in the vicinity of nanoparticle surface take the lead, where corona-like structures are formed, i.e. nanoparticles' surface interacts and is surrounded by copper (II) ions, forming a spherical shape. Above this value, aggregation dominates.

The HRS signal appears to abruptly drop for low copper ion addition, and then steadily grow above 1mM copper (II) bromide concentration. Results for high copper content required self-extinction correction, since the appearance of aggregates caused significant extinction at 800 nm. As can be observed from TEM microscopy pictures, included in the Supporting Information file, which can be found directly after the article in Chapter 5.4.2, "aggregation" means in fact dimer, or rarely trimer formation. Introducing some theoretical simulations for a mixture of monomers and dimers provided good consistency with experimental data.

To further understand the origin of HRS signal, polarization-resolved measurements were performed. See Figure 5 for one exemplary polar plot, whereas the remaining graphs were included in the Supporting Information file. It turned out, that the behaviour of gold nanoparticles can be again divided into two regimes: below and over 1 mM. Over this value, no significant changes of the depolarization ratio were observed. Meanwhile, below 1mM the ζ^V value steadily increases, which is in line with the DLS outcome, i.e. increasing effective diameter, causing an increase of signal retardation. The ζ^H parameter remains vanishingly small. Since the HRS signal measurement is the quickest and the simplest, it was chosen as the method of choice for sensing, and a Figure of Merit was proposed.

In the Conclusions section it was underlined that all performed measurements lead to a consistent conclusion of corona-like structure induced surface response under 1mM and the lead of aggregates formation above this value. A brief discussion about the Figure of Merit was followed by the selectivity issue, which was not discussed in detail. However, the Supporting Information file includes UV-Vis extinction spectra of gold nanoparticles with addition of copper (II) chloride, showing a similar behaviour, but with different change velocity, suggesting that it should be possible to distinguish different copper salts. This should be addressed to various bonding energies.

5.4.2. Publication

THE JOURNAL OF PHYSICAL CHEMISTRY C
A JOURNAL OF THE AMERICAN CHEMICAL SOCIETY

pubs.acs.org/JPCC Article

Sensing Copper(II) Ions with Hyper Rayleigh Scattering from Gold Nanoparticles

Krzysztof Nadolski, Fabien Rondepierre, Christian Jonin, Tomasz Marek Goszczyński, Katarzyna Matczyszyn,* and Pierre-François Brevet*

Cite This: *J. Phys. Chem. C* 2023, 127, 13097−13104 Read Online

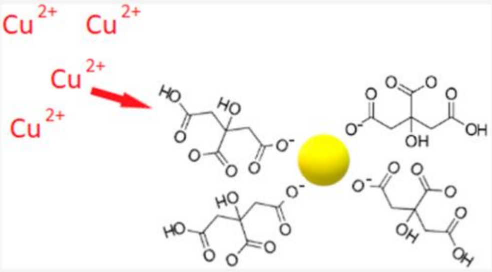

ABSTRACT: Incoherent Second Harmonic Generation (SHG) from gold nanoparticles, also known as hyper-Rayleigh scattering (HRS), is proposed as a sensing method for copper(II) ions. As opposed to colorimetry-based methods relying on the shift of the localized surface plasmon resonance with the copper(II) concentration, which effectively scales with the nanoparticle volume due to the origin of the absorption phenomenon, SHG relies on the surface origin of the response for sufficiently small nanoparticles. As a result, differences can be expected that could be potentially turned into advantages such as improved Limit of Detection and shorter detection response time. The present study demonstrates that the SHG light scattered from aqueous suspensions of gold nanoparticles in the presence of copper(II) ions is indeed sensitive to the copper(II) ion concentration changes. A first approach based on intensity changes shows that there is a competition between the formation of corona-like structures centered around the gold nanoparticles due to the ionic interaction between copper(II) ions and the negatively charged citrate-coated nanoparticles on one side and, on the other side, aggregation of nanoparticles due to charge screening as the copper(II) bromide concentration increases. The former process dominates at low copper(II) concentrations, whereas aggregation takes over above 1 mM copper(II) concentrations. A figure of merit is thus designed in order to provide a quantitative assessment of the sensing performance. In a further analysis, a polarization resolved study of the SHG light scattered from the gold nanoparticles allows the determination of other figures of merit. The first one based on the depolarization ratio seems appropriate, as it is based on the surface origin of the SHG response from gold nanoparticles, whereas the second one, based on the retardation parameter, should not perform better than those derived from colorimetry methods.

■ INTRODUCTION

Detection of copper(II) ions is crucial in various fields, from medicine[1,2] to food safety[3] and environmental pollution. For example, the maximum allowed level of copper in drinking water has been set to about 20 μM.[4] However, due to significant copper(II) ion intake coming from, say, plumbing pipes, the recommended daily intake may be fulfilled from drinking water only.[5] Meanwhile, overdoses may lead to oxidative stress and interfere with the homeostasis of other elements, such as Ca, Fe, or Mn.[6] Copper(II) homeostasis itself is responsible for pathologies associated with neurodegenerative diseases including Menkes and Wilson's disease, Alzheimer's, or Parkinson's.[7] Consequently, a proposal for quick, simple, and cost-efficient detection procedures should be of great help. An important class of sensing methods is based on optical phenomena and, more precisely, on changes in the optical properties of the sensing device in the presence of copper(II) ions.[8] A possibility is offered by gold nanoparticles (AuNPs) that exhibit a high sensitivity to surrounding medium changes,[9] resulting in colorimetric sensing possibilities due to the shift of the Localized Surface Plasmon Resonance (LSPR) through either surrounding solvent changes or surface chemical binding.[9] Aggregation and deaggregation of gold nanoparticles have also been proposed as the basis of copper(II) ions sensing. For example, after aggregation of polyvinylpyrrolidone (PVP)-stabilized AuNPs with 2-mercaptobenzimidazole (MBI), binding of copper(II) ions with MBI induces AuNPs redispersion.[10] Color changes, simply observed by the naked eye, indicated a 0.5 μM detection limit using UV−visible spectroscopy. As opposed to deaggregation, aggregation of citrate-stabilized AuNPs is induced with copper−citrate interaction.[11] In this case, a limit of detection of 5.0 mM was reported.

Received: March 14, 2023
Revised: May 26, 2023
Published: July 3, 2023

https://doi.org/10.1021/acs.jpcc.3c01713
J. Phys. Chem. C 2023, 127, 13097−13104

AuNPs colorimetric sensing methods are based on the change of AuNPs extinction, a linear optical phenomenon depending on the volume dependent absorption and scattering cross sections of AuNPs.[12] Hence, because the recognition step occurs at the AuNPs surface, faster methods with improved Limit of Detection (LoD) may be expected if based on surface-dependent properties. This possibility is offered by some nonlinear optical phenomena that have consequently attracted attention. Second Harmonic Generation (SHG), the phenomenon where two photons at a fundamental frequency are converted into a single photon at the double frequency, is highly sensitive to centrosymmetry breaking and thus appears as a potential candidate for surface sensing.[13]

In this report, Hyper Rayleigh Scattering (HRS), the incoherent scattering of SHG light, is investigated for an aqueous suspension of 50 nm diameter AuNPs to assess the sensing potential toward copper(II) ions.[14−16] The study entails the use of intensity and light polarization analysis of the scattered SHG intensity. Although the method in its details requires a close scrutiny of the nonlinear optical phenomenon, it appears that its setup into a sensing method remains accessible for a simple operation.

■ MATERIALS AND METHODS

The 50 nm diameter citrate-stabilized gold nanospheres, as well as copper(II) bromide, were purchased from Merck and used as received. Various concentrations of aqueous copper(II) bromide solutions were prepared using neat water (Millipore MilliQ 18 MΩ·cm). The addition of the copper(II) bromide salt solutions to the gold nanosphere solutions was performed for different volumetric ratios. After 30 min, the HRS measurements were conducted.

UV−visible spectra were recorded for all samples (Jasco, model V-730). The hydrodynamic diameter and zeta potential for all samples were determined by dynamic light scattering (DLS; Malvern, model Zetasizer Nano ZS). The sample solution was illuminated with a 633 nm laser, and the light intensity scattered at an angle of 173° was measured. At least six consecutive measurements were carried out for each sample. The time-dependent autocorrelation function of the photocurrent was acquired every 10 s with 15 acquisitions for each measurement. The experimental AuNPs average diameter was determined with measurements at 25 °C in water (viscosity 0.8872 mPa·s) using disposable folded capillary cells (DTS, model DTS1070). Electrophoretic mobilities were converted into zeta potential using Smoluchowski's formula.[17] DLS data were analyzed by using DTS 8.02 software (Malvern Instruments).

The structure and morphology of the samples were studied using a JEOL F-200 transmission electron microscope (JEOL Ltd., Tokyo, Japan) at an accelerating voltage of 80 kV. A total of 5 μL of the sample was placed on the copper grids with amorphous carbon, and next the sample was left until dry. The TVIPS camera (Germany) was used to determine the shape of the dispersed phase.

The HRS setup has been described elsewhere.[18] Briefly, the samples were excited by a femtosecond laser beam (Coherent, model Verdi X pumping a Mira 900) at a fundamental wavelength of 800 nm with pulse length of 140 fs and 80 MHz repetition rate, that was gently focused with a 10× objective in a configuration where excitation and collection directions are at right-angle. The harmonic intensity was collected with a CCD camera connected to a spectrometer, preceded by a high bandpass filter. For polarization-resolved studies, the angle of polarization of the linearly polarized input beam was set with a half-wave plate and analyzed with a half-wave plate and a cube polarizer in order to preserve the detected polarization. The average input power was around 250 mW.

■ RESULTS AND DISCUSSION

AuNPs samples with copper(II) bromide concentrations ranging from 0 to 25 mM were prepared. Their UV−visible spectra were then recorded, see Figure 1. The behavior of the extinction spectra can be described in terms of three phenomena: a red-shift of the LSPR peak, see Figure 2a, where this peak located at 525 nm is attributed to the localized surface plasmon resonance (LSPR) of the individual 50 nm diameter AuNPs, a change of this peak amplitude, see Figure 2b, and the appearance of a new band with a maximum around 780 nm, see Figure 2c.

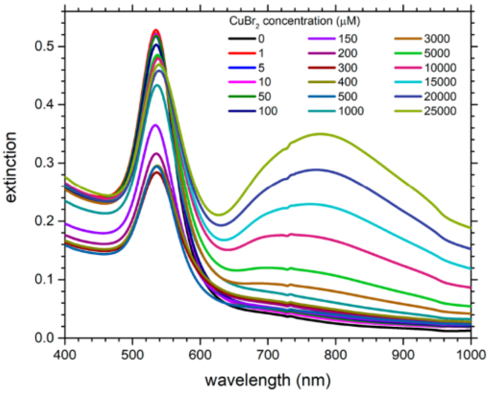

Figure 1. UV−visible extinction spectra of gold nanoparticle−copper(II) bromide mixtures. The color code is provided on the graph.

The graphs exhibit two main regimes, with the behavior being rather different below and above the 1 mM copper(II) bromide limit. Below this concentration, the redshift of the band associated with the LSPR of individual AuNP evolves rapidly with copper(II) bromide concentration. Above this limit, the increase continues, but the dependence is not so rapid anymore. Meanwhile, the LSPR peak amplitude drops rapidly below the 1 mM copper(II) bromide limit before stabilizing above this limit. Finally, the 780 nm extinction value also increases rapidly below the limit, whereas it continues to increase with copper(II) bromide concentration, but more slowly after the limit. Values shown in Figure 2a−c are calculated from five separate measurements on different sample preparations, hence, the relatively high uncertainties. From these UV−visible extinction spectra, the following Figures of Merit (FoM) with respect to copper(II) bromide concentration may be defined, namely, $\Delta\lambda/\Delta c$ = 0.30 ± 0.30 nm·μM^{-1} and $(\Delta\lambda/\lambda)/\Delta c = (5.55 \pm 4.83) \times 10^{-4}$ μM^{-1} for a relative shift of the LSPR peak wavelength. Based on the relative extinction change for this same LSPR peak, one can define similarly $(\Delta A/A)/\Delta c = (5.10 \pm 5.13) \times 10^{-2}$ μM^{-1} and for the absorbance at 780 nm $((\Delta A/A)/\Delta c = (1.03 \pm 52.49)$

$\times 10^{-2}\ \mu M^{-1}$. The uncertainty of the FoM based on the 780 nm is huge compared to the FoM value itself, a feature due to the very low extinction observed for low copper(II) bromide content, close to the detection limit of typical UV−visible spectrometers. Similar features are observed for the LSPR peak-based FoM value, which is lower or equal to its uncertainty. Only the relative change in the spectral position of the LSPR peak may thus be considered for sensing purposes at such small copper concentrations. In any case, considering the above FoM along their large uncertainties, and although linear optics based methods are much simpler to put up in practice, more appropriate methods are required, possibly based on more advanced optical processes.

Complementary to the UV−visible extinction spectra, zeta potential, Dynamic Light Scattering (DLS), and Transmission Electronic Microscopy (TEM) measurements were performed; see Figures 3a,b, S3a−d, and S4a−d. For samples with low copper(II) bromide content, only minor changes in the hydrodynamic diameter are observed, with a small decrease, followed by a steady increase above this limit. For the zeta

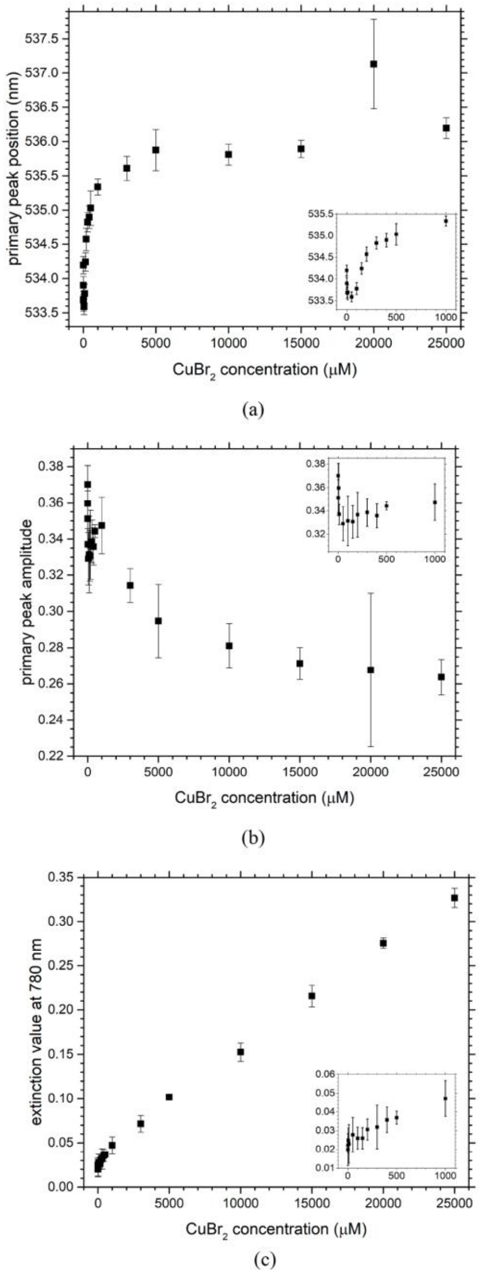

(a)

(b)

(c)

Figure 2. (a) Individual LSPR AuNP peak position and (b) amplitude as well as (c) extinction value at 780 nm derived from the UV−visible spectra reported in Figure 1 as a function of the copper(II) bromide concentration. (Insets) Zoomed views at low concentrations.

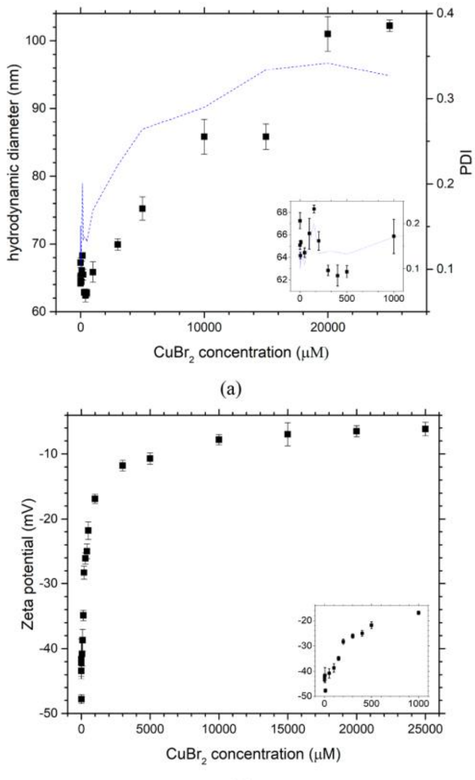

(a)

(b)

Figure 3. (a) Hydrodynamic diameter along with the polydispersity index (PDI) (blue dashed line) and (b) zeta potential of the studied samples as a function of the copper(II) bromide concentration. (Insets) Zoomed views at low concentrations.

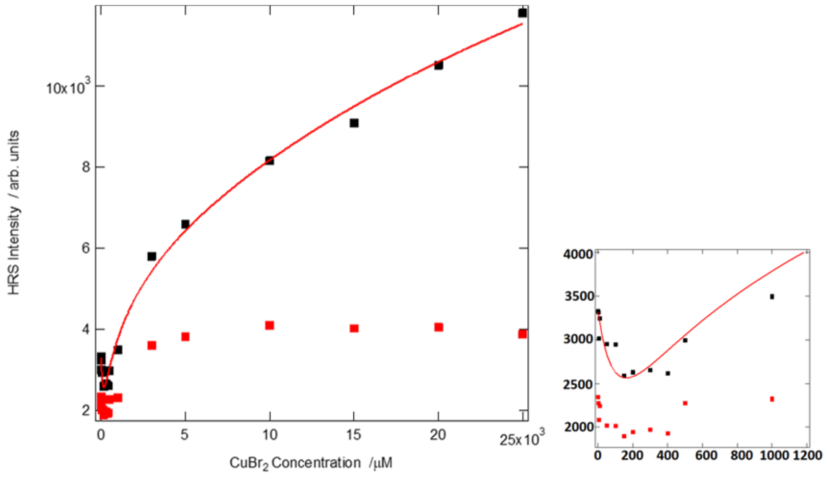

(main) (inset)

Figure 4. (Main) Hyper Rayleigh Scattering (HRS) intensity as a function of copper(II) bromide concentration, (red squares) HRS intensity uncorrected for self-extinction, (black squares) HRS intensity corrected for self-extinction, (red line) adjustment with the model; see text, (inset) zoomed view of the same graph at low concentrations.

potential, a rapid increase is observed before a plateau is reached after the 1 mM copper(II) bromide limit.

All of these observations may be rationalized with two main processes: a weak interaction between copper(II) ions and citrate dominating below the 1 mM copper(II) bromide limit followed by AuNPs aggregation dominating above this limit. The redshift of the primary extinction peak is probably caused by the formation of positively charged copper(II) ions corona-like structures around the negatively charged citrate-capped AuNPs.[19] This ionic interaction may be responsible for a weak shrinkage of the hydrodynamic diameter observed in Figure 3a at low copper(II) bromide concentrations. This ionic association between copper(II) ions and citrate has already been reported in the literature at low copper concentrations below 30 μM.[19] The possibility that the citrate anions would be replaced to some extent by bromide anions would not modify the formation of the copper (II) ion corona, as the latter likely stems from electrostatic interactions. Note nevertheless that a change of bromide for chloride provides a similar response, see Figure S1. On the opposite, AuNPs aggregation is known to occur at copper concentrations above 1 mM.[11] In fact, the two processes of weak ionic interactions and aggregation occur simultaneously. Below 1 mM, weak ionic interactions dominate, leading to a weak decrease of the hydrodynamic diameter with rapid changes in the zeta potential. When aggregation dominates, as indicated by the steady increase in the hydrodynamic diameter, the zeta potential reaches a plateau value. Moreover, the increase in the Polydispersity Index is in line with the appearance of aggregates, the size distribution of which is typically rather large.

Hyper Rayleigh Scattering experiments at 800 nm excitation were thus conducted on the above described samples; see Figure 4. The process of HRS is highly sensitive to the nanoparticle surface changes and, therefore, to the changes of the immediate surrounding of the nanoparticles, and indeed, the HRS intensity lowers immediately with small copper(II) bromide additions. Nevertheless, at a concentration of about 400 μM, the HRS intensity starts to rise steadily. Interestingly, the absorbance maximum recorded at 780 nm, close to 800 nm, which is the fundamental wavelength of the measurements, remains extremely weak at low copper content below about 400 μM, corresponding to an extinction below 0.05, see Figure 1. It must be, however, noted that the appearance of the peak around 780 nm is associated also with the appearance of copper(II) bromide, see Figure S2a in the Supporting Information. However, taking into consideration Figure S2b with subtracted copper(II) bromide influence, the tendency remains similar. An important factor that significantly affects the HRS behavior at higher copper contents is reabsorption; see Figure 4 where the uncorrected and extinction-corrected HRS intensities as a function of copper(II) bromide concentration are provided. The correction for self-extinction was obtained using the following expression:

$$I_{\mathrm{HRS}} = I_{0,\mathrm{HRS}} \cdot 10^{(2A_{800}+A_{400})/2} \tag{1}$$

where I_{HRS} is the corrected HRS intensity, $I_{0,\mathrm{HRS}}$ stands for HRS intensity before correction, and A_{800} and A_{400} are extinction values at 800 and 400 nm, respectively. The factor 1/2 is introduced to account for the difference in the path length between UV−visible extinction and HRS measurements. The extinction-corrected HRS intensity was then modeled using a simple model involving the first hyperpolarizability tensor $\boldsymbol{\beta}_{\mathrm{m}}$ for the gold nanoparticles and $\boldsymbol{\beta}_{\mathrm{d}}$ for the nanoparticle dimers. The total HRS intensity has the following expression:

$$I_{\mathrm{HRS}} = G[N_{\mathrm{m}}\langle\beta_{\mathrm{m}}^2\rangle + N_{\mathrm{d}}\langle\beta_{\mathrm{d}}^2\rangle] \tag{2}$$

where N_i stands for the monomer and dimer concentrations and the ⟨⟩ bracket stands for orientational averaging. G is a general constant. It is important to underline here that the model is simplified to a unique monomer−dimer equilibrium, whereas it is possible to introduce larger aggregates. However, introducing the possibility of the formation of larger aggregates involving three or more gold nanoparticles would only bring further complexity to the model with new but unnecessary parameters. The first hyperpolarizabilities were of the following form:

$$\boldsymbol{\beta}_i = \boldsymbol{\beta}_{i0} + \Delta\boldsymbol{\beta}\ \exp[-\alpha_i C] \tag{3}$$

where $\boldsymbol{\beta}_i$ is the first hyperpolarizability of the monomer or dimer with i = m,d, $\boldsymbol{\beta}_{i0}$ is the first hyperpolarizability of the monomer or dimer at large copper(II) ion concentration, $\Delta\boldsymbol{\beta}$ is the change in first hyperpolarizability due to copper(II) ion concentration, and α_i is the scaling parameter determining the first hyperpolarizability dependence with copper(II) ions concentration C. Bold characters are used to indicate tensors in eq 3, applying for any tensor element, whereas nonbold characters are used in eq 2 because tensor elements are selected by the polarization configuration. Finally, the monomer−dimer equilibrium is defined through an equilibrium constant itself dependent on the copper(II) ion concentration. Adjustment of the model to the experimental data is given in Figure 4, providing a correct description of the behavior of the HRS intensity as a function of the copper(II) ion concentration. This simple model, once linearized at very low copper(II) ion concentration, provided the following FoM defined as the relative HRS intensity change as a function of copper(II) ion concentration, namely, $[(\Delta I_{\mathrm{HRS}}/I_{\mathrm{HRS}})/C]_{C=0} = -(5 \pm 2) \times 10^{-3}\ \mu\mathrm{M}^{-1}$. Note that this FoM is negative due to the initial HRS intensity decrease and that it may be preferable to redefine it as its absolute value, hence, reporting this FoM as $[|\Delta I_{\mathrm{HRS}}/I_{\mathrm{HRS}}|/C]_{C=0} = (5 \pm 2) \times 10^{-3}\ \mu\mathrm{M}^{-1}$. The concentration range over which that FoM was determined is, however, limited to the 0−150 μM range. This resulting FoM provides a LoD well below 1 mM, reaching about 100 μM, with possibilities of improvement by lengthening the acquisition time.

To further investigate the sensing potential of the method, polarization-resolved measurements were performed as a function of the copper(II) bromide concentration. The resulting experimental data, gathered in Figure 5 (sample without copper(II) bromide) and in the Supporting Information (see Figures S5a−h for the remaining samples), were fitted with the following expression:[20]

$$I_{\mathrm{HRS}}^{X} = a^{X}\cos^{4}\gamma + b^{X}\cos^{2}\gamma\sin^{2}\gamma + c^{X}\sin^{4}\gamma \tag{4}$$

where I_{HRS}^{X} indicates polarization-resolved HRS intensity, a^X, b^X, and c^X are polarized intensity parameters, X stands for either vertically (V) or horizontally (H) polarized output harmonic intensity, and γ is the angle of polarization of the linearly polarized fundamental beam. In order to provide a deep insight into the response, three parameters were further computed:

$$D^{\mathrm{V}} = c^{\mathrm{V}}/a^{\mathrm{V}} \tag{5a}$$

$$\zeta^{\mathrm{V}} = (b^{\mathrm{V}} - a^{\mathrm{V}} - c^{\mathrm{V}})/b^{\mathrm{V}} \tag{5b}$$

$$\zeta^{\mathrm{H}} = (a^{\mathrm{H}} - c^{\mathrm{H}})/(a^{\mathrm{H}} + c^{\mathrm{H}}) \tag{5c}$$

where D^{V} is the depolarization ratio[18] and ζ^{V} and ζ^{H} are the so-called retardation parameters.[20,21] All three parameters are autonormalized, as they result from ratios of the HRS intensity collected for specific fundamental and harmonic angles of polarization. The depolarization ratio D^{V} provides insight into the symmetry of the nonlinear response within the irreducible susceptibility spherical tensor description, with a value ranging from 1/9 for a pure dipolar symmetry to 2/3 for an octupolar symmetry within the Kleinmann approximation. The retardation parameters ζ^{V} and ζ^{H} are related to the size through the phase retardation occurring within the nanoparticles. Hence, they vanish for small nanoparticles, i.e., for sizes below about 40 nm in the case of gold nanoparticles and can reach about unity for the largest spherical nanoparticles, beyond 150 nm diameter or so. The depolarization ratio D^{V} increases with the copper(II) bromide concentration from an initial value of about 0.3, a standard value for gold nanoparticles, before reaching a plateau value of about 0.46 at a concentration of 5 mM; see Figure 6a. This value in the range between 0.3 and 0.4 indicates a similar contribution from dipolar and octupolar irreducible tensor contributions.[22] This parameter increase from 0.3 up to 0.44 indicates that the presence of copper(II) corona-like structures established around the nanoparticles favors the octupolar response against the dipolar one. This may be explained through corona-like structures somehow passivating the initial surface response of the nanoparticle and leading to a nonlinearity better distributed around the nanoparticle surface, still in a noncentrosymmetric manner.[23] At higher copper(II) concentrations, this depolarization ratio reaches a plateau value determined by the nanoparticle aggregates. Their geometry therefore favors nonlinearity with octupolar symmetry, probably due to the random spatial arrangement of the gold nanoparticles within the aggregates.

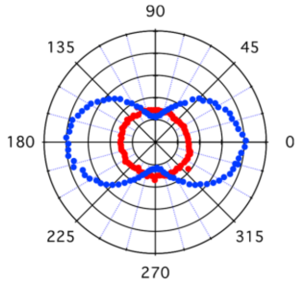

Figure 5. Polar plot of the polarization-resolved normalized HRS intensity as a function of the angle of polarization of the fundamental beam: (blue) vertically polarized HRS intensity and (red) horizontally polarized HRS intensity. The presented result is of pure nanoparticles, i.e., without copper(II) bromide. The remaining polar plots can be found in the Supporting Information, Figure S5a−h.

The retardation parameter, ζ^{V}, retains a nonvanishing value in the absence of copper(II) ions already for 50 nm diameter gold nanoparticles, in agreement with literature.[24] The second retardation parameter, ζ^{H}, retains a nonvanishing value, too, but the latter is rather small and then further decreases toward a vanishing value at the highest copper(II) concentrations. Their behavior is thus contrasted. Indeed, in contrast, the ζ^{V} parameter exhibits a strong increase, followed by a rapid decrease, and then a plateau value when aggregation takes place as the copper(II) concentration increases. The ζ^{V}

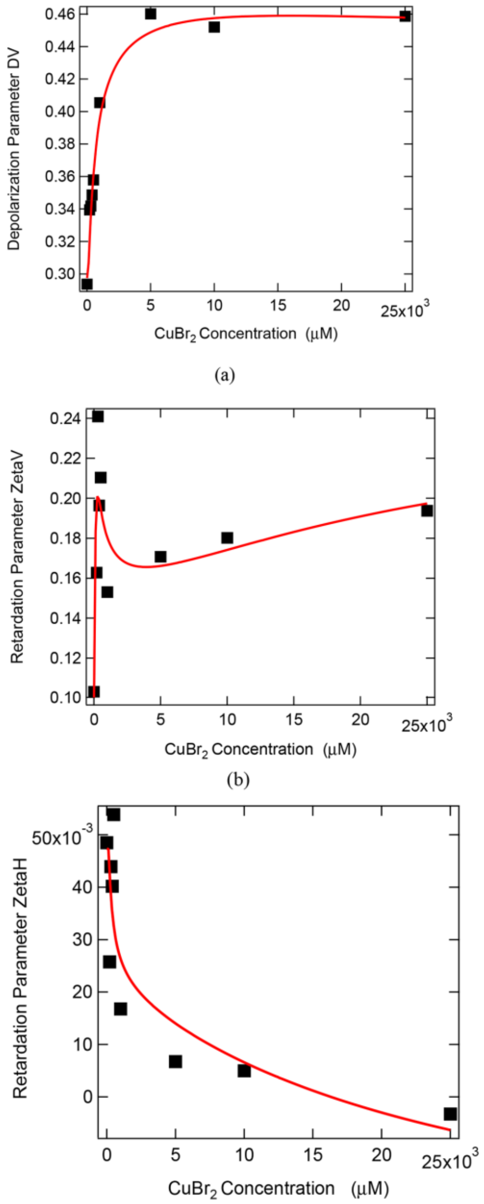

(a)

(b)

(c)

Figure 6. (a) Depolarization ratio D^V and retardation parameters (b) ζ^V and (c) ζ^H with respect to the copper(II) bromide concentration.

parameter presents a more reliable behavior with copper(II) bromide additions due to its larger value.[20,24] In the regime of low concentrations, as copper(II) ions form corona-like structures around the AuNPs, its rapid increase may relate to some extent to the weakening of the noncentrosymmetry of the gold nanoparticles due to a weakening of the surface contribution. However, it is interesting to note that, when the aggregation takes place, the parameter ζ^V quickly stabilizes.[22,23,25]

Because of its rather low value, the ζ^H parameter does not probably constitute a good FoM. It also switches from positive to negative values at large copper(II) ion concentration, and this is related to the dominating dimer hyperpolarizability over that of the monomers in this concentration region. All parameters resulting from the adjustment are reported in Table S1 in the Supporting Information.

In order to quantitatively assess the LoD of the method, figures of merit can be derived. From intensity measurements, one can simply derive as a figure of merit the ratio between the relative HRS intensity change ($\Delta I_{HRS}/I_{HRS}$ with respect to the concentration change C, see above). If polarization-resolved intensities are now used, then other figures of merit can be formed with the depolarization ratio D^V or the first retardation parameter ζ^V. Such FoM expressed as $[(\Delta D^V/D^V)/C]_{C=0}$ or $[(\Delta\zeta^V/\zeta^V)/C]_{C=0}$ may then be built either from the model or directly from the experimental data, with a linear adjustment at the origin. Both lead to similar values. Then, FoMs of the order of $1 \times 10^{-4}\ \mu M^{-1}$ are obtained. To our knowledge, no similar FoM has been proposed in the literature yet, as such figures of merit are rather unusual. It must be pointed out though that the $[(\Delta\zeta^V/\zeta^V)/C]_{C=0}$ figure of merit is based on retardation and therefore scales with the gold nanoparticle diameter (or size). Hence, this FoM should not be competitive compared to colorimetry-based sensing methods similarly based on size scaling as well. Hence, using larger diameter gold nanoparticles as compared to the present 50 nm diameter ones should not bring any improved LoD. On the opposite, the $[(\Delta D^V/D^V)/C]_{C=0}$ FoM, built from the polarization plots and the a^V and c^V parameters, the origin of which is surface-specific, fulfills the initial demand of a surface-specific FoM with an improved value as compared to the HRS intensity-based FoM $[[(\Delta I_{HRS}/I_{HRS}]/C]_{C=0}$. Note though that in principle the $[(\Delta D^V/D^V)/C]_{C=0}$ FoM requires twice as many measurements due to the HRS intensity ratio nature of the D^V parameter.

■ CONCLUSIONS

In this study, the potential of a sensing method based on the nonlinear optical process of SHG using gold nanoparticles is investigated. In addition to standard control based on UV−visible extinction spectroscopy, zeta potential, and DLS measurements, an intensity and polarization-based study of the changes of the HRS response with the copper(II) bromide concentration is performed. It appears that a competition between the formation of copper(II)-induced corona-like structures centered around the gold nanoparticles and the aggregation of the latter is taking place. The former process appears at low copper(II) bromide concentrations, well below 1 mM, whereas aggregation takes over above this limit. The HRS intensity analysis exhibits first an intensity decrease at low copper(II) bromide concentration, due to the corona-like structure formation, followed by an increase as aggregation takes place. Saturation of the intensity then occurs at the largest copper(II) bromide concentrations, precluding the use of HRS as a sensing method in this concentration range. Likewise, the polarization-resolved HRS analysis reveals a similar retardation behavior at high copper(II) bromide concentration for both the depolarization and the retardation parameters. Hence, at low concentrations, the HRS based method appears to present a useful approach for copper(II) sensing, with the highest FoM in the range of $(5 \pm 2) \times 10^{-3}$ μM^{-1} in the 0−150 μM $CuBr_2$ range, a clearly improved magnitude as compared to UV−visible extinction spectroscopy methods based on the relative spectral localization of the LSPR peak. In fact, as shown initially for comparison, the UV−visible spectroscopy measurement of the LSPR shift turns out to be unreliable for this copper(II) ion sensing experiment, as the uncertainty is very close to the obtained value.

In the case of polarization measurements, FoM based on the retardation parameter ζ^V that is nonzero for relatively large diameter gold nanoparticles due to a size scaling suggests that the FoM should not be better than those derived from colorimetry methods where the same scaling operates. On the opposite, a FoM of the form $[(\Delta D^V/D^V)/C]_{C=0}$ presents advantages with an improved value of the order of 1×10^{-4} μM^{-1}. On a final note, it is pointed out first that the nonlinear dependence of these two FoMs with a copper(II) bromide concentration may bring a further degree of complexity for the establishment of a sensing method, preferably based on linear dependencies, unless linearization is introduced at low copper(II) concentrations. Second, there remains the question of the selectivity and interference of the copper(II) ion sensing in the case of waters containing other ions. In this work, the origin of the interaction between copper(II) ions and negatively charged gold nanoparticles is likely of electrostatic origin. Hence, selectivity may not be achieved, and interference may occur with other ions. These two aspects will be investigated in further studies.

■ ASSOCIATED CONTENT

Supporting Information

The Supporting Information is available free of charge at https://pubs.acs.org/doi/10.1021/acs.jpcc.3c01713.

> Complementary data for UV−visible extinction spectroscopy, TEM, complete list of the adjusted parameters of the model, and polarization resolved HRS intensity plots of the studied samples (PDF)

■ AUTHOR INFORMATION

Corresponding Authors

Katarzyna Matczyszyn − *Institute of Advanced Materials, Faculty of Chemistry, Wroclaw University of Science and Technology, 50-370 Wroclaw, Poland;* orcid.org/0000-0001-8578-8340; Email: katarzyna.matczyszyn@pwr.edu.pl

Pierre-François Brevet − *Institut Lumière Matière, Université Claude Bernard Lyon 1, CNRS UMR 5306, 69100 Villeurbanne, France;* orcid.org/0000-0002-9097-0187; Email: pfbrevet@univ-lyon1.fr

Authors

Krzysztof Nadolski − *Institut Lumière Matière, Université Claude Bernard Lyon 1, CNRS UMR 5306, 69100 Villeurbanne, France; Institute of Advanced Materials, Faculty of Chemistry, Wroclaw University of Science and Technology, 50-370 Wroclaw, Poland;* orcid.org/0000-0002-6534-845X

Fabien Rondepierre − *Institut Lumière Matière, Université Claude Bernard Lyon 1, CNRS UMR 5306, 69100 Villeurbanne, France*

Christian Jonin − *Institut Lumière Matière, Université Claude Bernard Lyon 1, CNRS UMR 5306, 69100 Villeurbanne, France*

Tomasz Marek Goszczyński − *Laboratory of Biomedical Chemistry, Hirszfeld Institute of Immunology and Experimental Therapy, Polish Academy of Sciences, 53-114 Wroclaw, Poland;* orcid.org/0000-0002-9995-3260

Complete contact information is available at: https://pubs.acs.org/10.1021/acs.jpcc.3c01713

Notes

The authors declare no competing financial interest.

■ ACKNOWLEDGMENTS

K.N. and K.M. acknowledge funding from the National Science Centre in Poland within the Harmonia DEC/2016/22/M/ST4/00275 Project and funding from the National Science Centre in Poland within the Opus UMO-2019/35/B/ST4/03280 Project. All authors acknowledge funding from the PPN/BFT/2019/1/00030/U/0001 PHC POLONIUM Project, cofunded by the Polish National Agency For Academic Exchange and Campus France.

■ REFERENCES

(1) Desai, V.; Kaler, S. G. Role of copper in human neurological disorders. *Am. J. Clin. Nutr.* **2008**, *88*, 855S−858S.

(2) Lutsenko, S.; Barnes, N. L.; Bartee, M. Y.; Dmitriev, O. Y. Function and Regulation of Human Copper-Transporting ATPases. *Physiol. Rev.* **2007**, *87*, 1011−1046.

(3) Xiang, G.; Wen, S.; Jiang, X.; Liu, X.; He, L. Determination of Trace Copper(II) in Food Samples by Flame Atomic Absorption Spectrometry after Cloud Point Extraction. *Iran. J. Chem. Chem. Eng.* **2011**, *30*, 101−107.

(4) Liu, J.; Lu, Y. A DNAzyme Catalytic Beacon Sensor for Paramagnetic Cu^{2+} Ions in Aqueous Solution with High Sensitivity and Selectivity. *J. Am. Chem. Soc.* **2007**, *129*, 9838−9839.

(5) Wu, M.; Zhi, M.; Liu, Y.; Han, J.; Qin, Y. In situ analysis of copper speciation during in vitro digestion: Differences between copper in drinking water and food. *Food Chem.* **2022**, *371*, 131388.

(6) Witt, B.; Stiboller, M.; Raschke, S.; Friese, S.; Ebert, F.; Schwerdtle, T. Characterizing effects of excess copper levels in a human astrocytic cell line with focus on oxidative stress markers. *J. Trace Elem. Med. Biol.* **2021**, *65*, 126711.

(7) Scheiber, I. F.; Mercer, J. F. B.; Dringen, R. Metabolism and functions of copper in brain. *Prog. Neurobiol.* **2014**, *116*, 33−57.

(8) Udhayakumari, D.; Naha, S.; Velmathi, S. Colorimetric and fluorescent chemosensors for Cu^{2+}. A comprehensive review from the years 2013−15. *Anal. Methods* **2017**, *9*, 552−578.

(9) Hu, M.; Novo, C.; Funston, A.; Wang, H.; Staleva, H.; Zou, S.; Mulvaney, P.; Xia, Y.; Hartland, G. V. Dark-field microscopy studies of single metal nanoparticles: understanding the factos that influence the linewidth of the localized surface plasmon resonance. *J. Mater. Chem.* **2008**, *18*, 1949−1960.

(10) Ye, Y.; Lv, M.; Zhang, X.; Zhang, Y. Colorimetric determination of copper(II) ions using gold nanoparticles as a probe. *RSC Adv.* **2015**, *5*, 102311−102317.

(11) Salcedo, A. R. M.; Sevilla, F. B., III Citrate-Capped Gold Nanoparticles as Colorimetric Reagent for Copper (II) Ions. *Philipp. Sci. Lett.* **2013**, *6*, 90−96.

(12) Bohren, C. F.; Huffman, D. R. *Absorption and Scattering of Light by Small Particles*; John Wiley & Sons Inc.: New York, NY, U.S.A., 1983.

(13) Tran, R. J.; Sly, K. L.; Conboy, J. C. Applications of Surface Second Harmonic Generation in Biological Sensing. *Annu. Rev. Anal. Chem.* **2017**, *10*, 387−414.

(14) Hao, E. C.; Schatz, G. C.; Johnson, R. C.; Hupp, J. T. Hyper-Rayleigh scattering from silver nanoparticles. *J. Chem. Phys.* **2002**, *117*, 5963.

(15) Nadolski, K.; Benichou, E.; Tarnowicz-Staniak, N.; Żak, A.; Jonin, C.; Matczyszyn, K.; Brevet, P-F. Adverse Role of Shape and Size in Second-Harmonic Scattering from Gold Nanoprisms. *J. Phys. Chem. C* **2020**, *124*, 14797−14803.

(16) Ngo, H. M.; Lai, N. D.; Ledoux-Rak, I. High second-order nonlinear response of platinum nanoflowers: the role of surface corrugation. *Nanoscale* **2016**, *8*, 3489−3495.

(17) Sze, A.; Erickson, D.; Ren, L.; Li, D. Zeta-potential measurement using the Smoluchowski equation and the slope of the current−time relationship in electroosmotic flow. *J. Colloid Interface Sci.* **2003**, *261*, 402−410.

(18) Nappa, J.; Revillod, G.; Russier-Antoine, I.; Benichou, E.; Jonin, C.; Brevet, P-F. Electric dipole origin of the second harmonic generation of small metallic particles. *Phys. Rev. B* **2005**, *71*, 165407.

(19) Wang, N.; Dai, H.; Sai, L.; Ma, H.; Lin, M. Cooper ion-assisted gold nanoparticle aggregates for electrochemical signal amplification of lipopolysaccharide sensing. *Biosens. Bioelectron.* **2019**, *126*, 529−534.

(20) Butet, J.; Bachelier, G.; Russier-Antoine, I.; Jonin, C.; Benichou, E.; Brevet, P-F. Interference between Selected Dipoles and Octupoles in the Optical Second-Harmonic Generation from Spherical Gold Nanoparticles. *Phys. Rev. Lett.* **2010**, *105*, 077401.

(21) El Harfouch, Y.; Benichou, E.; Bertorelle, F.; Russier-Antoine, I.; Jonin, C.; Lascoux, N.; Brevet, P-F. Hyper-Rayleigh Scattering from Gold Nanorods. *J. Phys. Chem. C* **2014**, *118*, 609−616.

(22) Brasselet, S.; Zyss, J. Multipolar molecules and multipolar fields: probing and controlling the tensorial nature of nonlinear molecular media. *J. Opt. Soc. Am. B* **1998**, *15*, 257−288.

(23) Duboisset, J.; Brevet, P-F. Second-Harmonic Scattering-Defined Topological Classes for Nano-Objects. *J. Phys. Chem. C* **2019**, *123*, 25303−25308.

(24) Russier-Antoine, I.; Benichou, E.; Bachelier, G.; Jonin, C.; Brevet, P-F. Multipolar Contributions of the Second Harmonic Generation from Silver and Gold Nanoparticles. *J. Phys. Chem. C* **2007**, *111*, 9044−9048.

(25) Bachelier, G.; Russier-Antoine, I.; Benichou, E.; Jonin, C.; Brevet, P-F. Multipolar second-harmonic generation in noble metal nanoparticles. *J. Opt. Soc. Am. B* **2008**, *25*, 955−960.

Sensing Copper (II) Ions with Hyper Rayleigh Scattering from Gold Nanoparticles

SUPPORTING INFORMATION

Krzysztof Nadolski,[1,2] Fabien Rondepierre,[1] Christian Jonin,[1] Tomasz Marek Goszczyński,[3] Katarzyna Matczyszyn,[2] Pierre-François Brevet[1*]*

[1]Institut Lumière Matière, Université Claude Bernard Lyon 1, CNRS UMR 5306, 69100 Villeurbanne, France.

[2]Institute of Advanced Materials, Faculty of Chemistry, Wroclaw University of Science and Technology, 50-370 Wroclaw, Poland.

[3]Laboratory of Biomedical Chemistry, Hirszfeld Institute of Immunology and Experimental Therapy, Polish Academy of Sciences, 53-114 Wroclaw, Poland

1 UV-Visible extinction spectroscopy

In order to determine the influence of used anion, a comparison of copper (II) bromide and copper (II) chloride chosen UV-Vis extinction spectra can be observed in Figure S1.

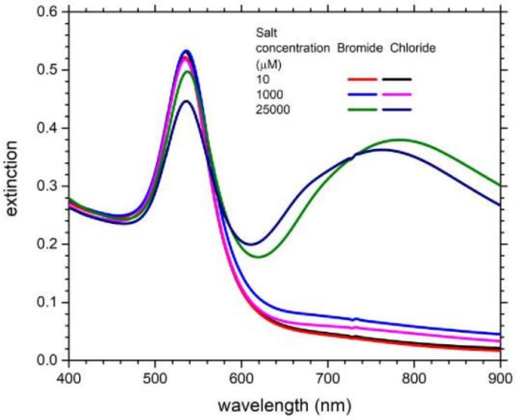

Figure S1. Comparison of UV-Vis extinction spectra with copper (II) chloride and copper (II) bromide for chosen salt concentrations, as indicated in the legend.

UV-Vis spectroscopy extinction spectrum of copper (II) bromide can be found below, see Figure S2 (a). For Figure S1 (b), namely copper (II) bromide extinction-corrected extinction value at 780 nm, correction means subtracting the value of salt absorption at this point.

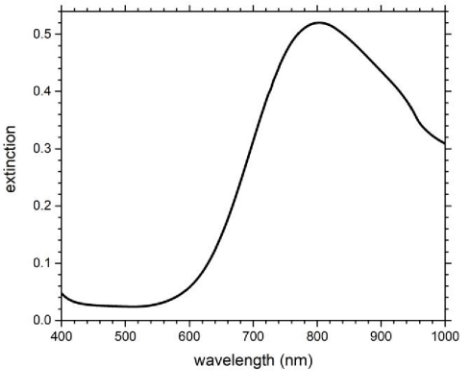

(a)

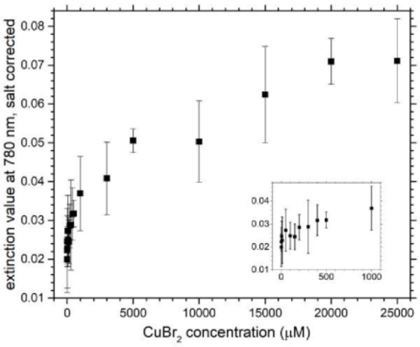

(b)

Figure S2: (a) UV-Vis extinction spectrum of 50 mM copper (II) bromide and (b) copper (II) bromide extinction-corrected extinction value at 780 nm for all samples. (Insert) blow-up views at low concentrations.

2 TEM Microscopy

TEM pictures of the pure nanoparticles (without copper (II) bromide addition) (Figure S1) and with the highest concentration of 25 mM $CuBr_2$ (Figure S2) can be found below. Normally, the samples should have the surplus surfactant removed prior to TEM imaging, however the procedure of centrifugation may significantly affect the aggregation, thus this step was skipped.

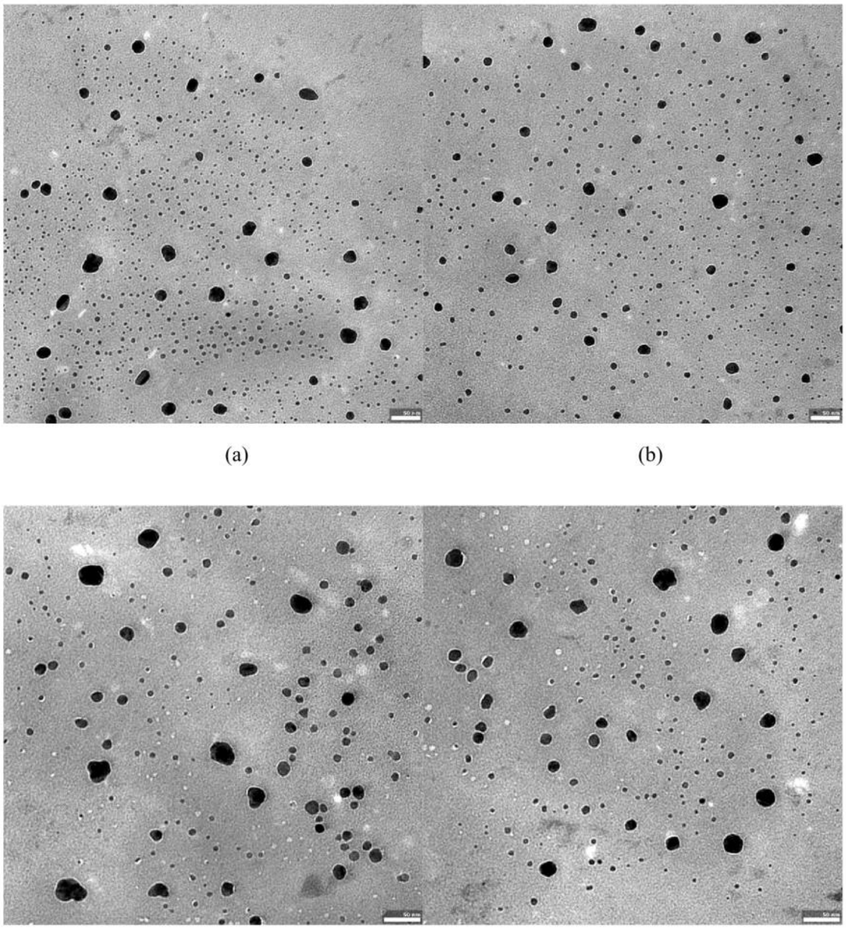

(a) (b)

(c) (d)

Figure S3: (a) – (d) TEM pictures of the pure nanoparticles (without copper (II) bromide).

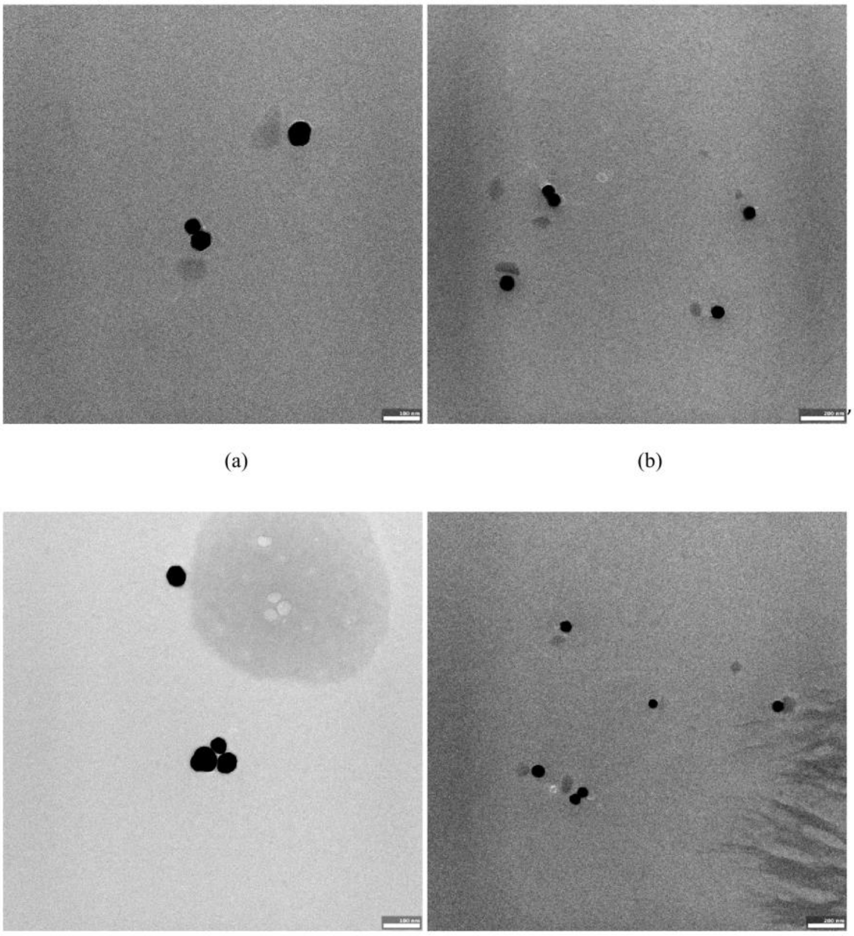

(a) (b)

(c) (d)

Figure S4: (a) – (d) TEM pictures of the sample with the highest copper (II) bromide concentration, i.e. 25 mM.

3 Adjusted Parameters of the model

The list of parameters as well as their values is provided below. It is important to underline that the adjustment procedure is sequential as all these parameters can be adjusted by sets of a reduced number of them and not the full set adjustment at once.

Table S1 : List and adjusted value of the parameters required to adjust the experimental data. First hyperpolarizability tensor elements are $\beta_{a,IJK,b}$ where $a = m, d$, m indicates monomer and d dimer, $b =$ AuNP, Cu(II)-AuNP where AuNP indicates gold nanoparticles in absence of copper(II) ions and Cu(II)-AuNP gold nanoparticles in the presence of Copper(II) ions. Also, I, J, K stands for the laboratory frame axes X, Y or Z and are reported in arb. units.

Hyperpolarizability Parameter	**Value (arb. units)**
$\beta_{m,XXX,AuNP}$	55
$\beta_{m,XXX,Cu(II)-AuNP}$	41
$\beta_{d,XXX,AuNP}$	115
$\beta_{d,XXX,Cu(II)-AuNP}$	175
$\beta_{m,XYY,AuNP}$	30
$\beta_{m,XYY,Cu(II)-AuNP}$	21
$\beta_{d,XYY,AuNP}$	81
$\beta_{d,XYY,Cu(II)-AuNP}$	118
$\beta_{m,XXY,AuNP}$	16.3
$\beta_{m,XXY,Cu(II)-AuNP}$	16.5
$\beta_{d,XXY,AuNP}$	32.1
$\beta_{d,XXY,Cu(II)-AuNP}$	64.1
$\beta_{m,ZXX,AuNP}$	17
$\beta_{m,ZXX,Cu(II)-AuNP}$	13
$\beta_{d,ZXX,AuNP}$	74

$\beta_{d,ZXX,Cu(II)-AuNP}$	98
$\beta_{m,ZYY,AuNP}$	16
$\beta_{m,ZYY,Cu(II)-AuNP}$	12
$\beta_{d,ZYY,AuNP}$	73
$\beta_{d,ZYY,Cu(II)-AuNP}$	100
$\beta_{m,ZXY,AuNP}$	0
$\beta_{m,ZXY,Cu(II)-AuNP}$	0
$\beta_{d,ZXY,AuNP}$	0
$\beta_{d,ZXY,Cu(II)-AuNP}$	0

whereas all other hyperpolarizability tensor elements required are vanishing.

Other Parameters	**Value**
α_m	0.01 μM^{-1}
α_d	3.4×10^{-5} μM^{-1}
K_0	0 μM^{-1}
K_1	0.00022 μM^{-2}

The constant of the monomer – dimer equilibrium K_{md} is given by :

$$K_{md} = \frac{[d]}{[m]^2} = K_0 + K_1 C \tag{S1}$$

Also, the relationships between the HRS intensity parameters a^V, b^V, c^V and a^H, b^H , c^H, see main text, are :

$$a^V = [m]\langle\beta_{m,XXX}^2\rangle + [d]\langle\beta_{d,XXX}^2\rangle$$

$$b^V = [m]\{\langle 2\beta_{m,XXX}\beta_{m,XYY} + 4\beta_{m,XXY}^2\rangle\} + [d]\{\langle 2\beta_{d,XXX}\beta_{d,XYY} + 4\beta_{d,XXY}^2\rangle\}$$

$$c^V = [m]\langle\beta_{m,XYY}^2\rangle + [d]\langle\beta_{d,XYY}^2\rangle$$

and

$$a^{H} = [m]\langle\beta_{m,ZXX}^{2}\rangle + [d]\langle\beta_{d,ZXX}^{2}\rangle$$

$$b^{H} = [m]\{\langle 2\beta_{m,ZXX}\beta_{m,ZYY} + 4\beta_{m,ZXY}^{2}\rangle\} + [d]\{\langle 2\beta_{d,ZXX}\beta_{d,ZYY} + 4\beta_{d,ZXY}^{2}\rangle\}$$

$$c^{H} = [m]\langle\beta_{m,ZYY}^{2}\rangle + [d]\langle\beta_{d,ZYY}^{2}\rangle$$

4 Polarization-resolved HRS measurements

Polarization resolved plots of the HRS intensity as a function of the fundamental angle of polarization are presented below, see Figure S5(a)-(h).

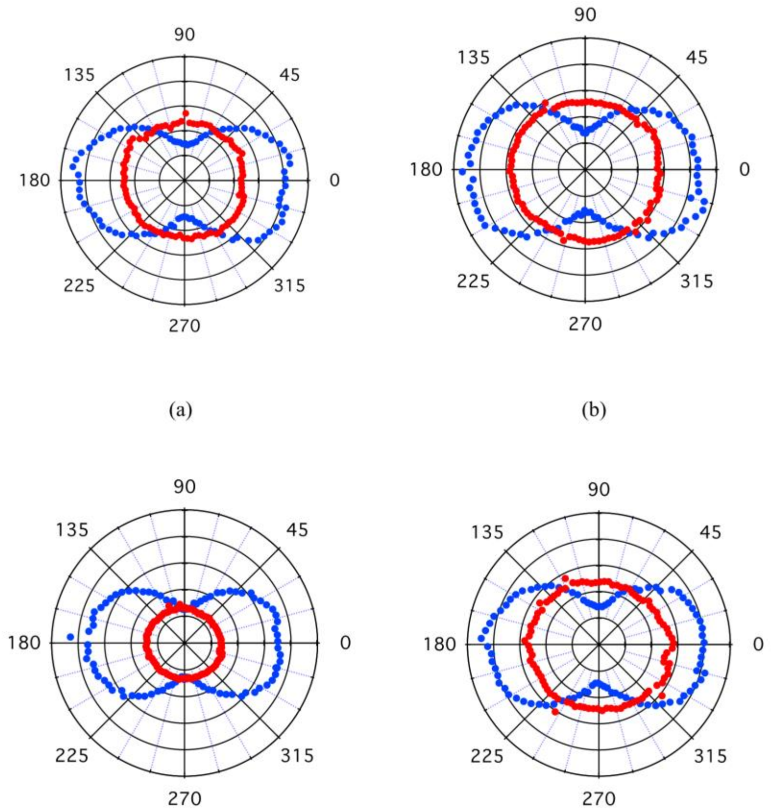

(a) (b)

(c) (d)

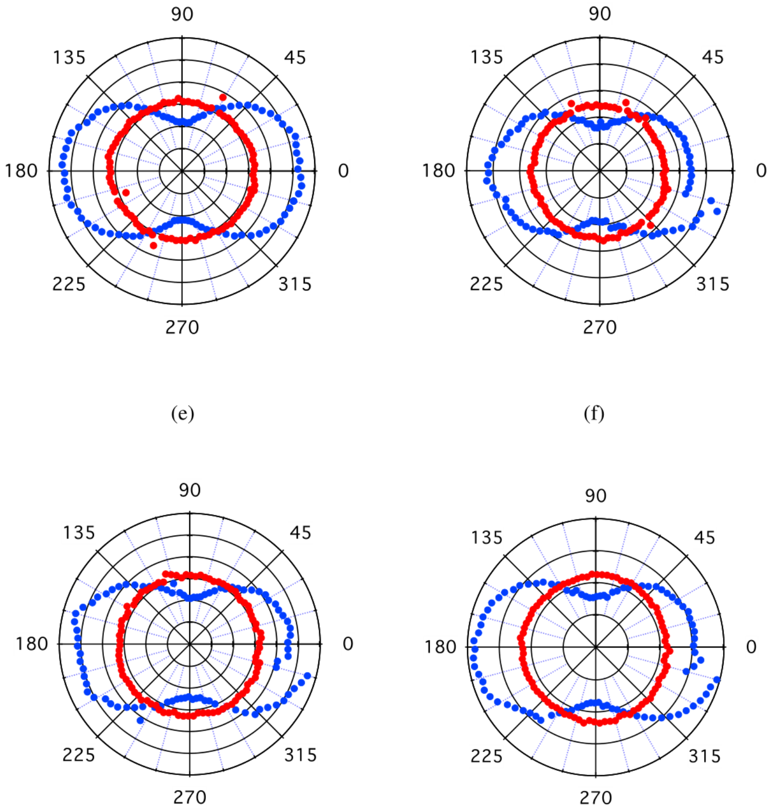

(e) (f)

(g) (h)

Figure S5 : (a) – (h) Polar plots of the polarization-resolved normalized HRS intensity as a function of the angle of polarization of the fundamental beam, (blue) vertically polarized HRS intensity, (red) horizontally polarized HRS intensity. Copper (II) bromide concentrations (a) 200 µM, (b) 300 µM, (c) 400 µM, (d) 500 µM, (e) 1 mM, (f) 5 mM, (g) 10 mM, and (h) 25 mM.

6. Summary and conclusions

This thesis is a complementary work concerning Hyper Rayleigh Scattering for sensing purposes with use of gold nanoparticles. First, a theoretical introduction was presented. It concerned topics such as nanoplasmonics, gold nanoparticles' fabrication or nonlinear optics. In the first part of experimental study, gold nanotriangles of sizes ranging between 26 and 87 nm were successfully synthesised and characterised. Not only the non centrosymmetrical shape was of concern, but also a novel approach to study a mixture of shapes, in this case nanotriangles and nanospheres.

The first hyperpolarizability per surface unit is constant, thus the signal stems from surface effects for both nanospheres and nanotriangles, which is in contrary to results known from the literature for centrosymmetrically-shaped nanoparticles. The value itself is significantly lower compared to literature, however the influence of stabilizing agent should be studied in detail.

The polarization-resolved studies' results are contradictory to results obtained for other shapes. Namely, the retardation remains low despite a size growth. The depolarization ratio oscillates around 0.45, which is far away from a point-like one-fold structure, where it is expected to be 0.2.

Surprisingly, the first hyperpolarizability of nanotriangles is very low, which may be nevertheless addressed to the stabilizing agent. The low retardation level is promising for sensing purposes.

In Chapter 5.3, the influence of surrounding medium refractive index on the HRS response was studied. Gold nanospheres of 40 and 100 nm mean diameter were added glycerol to change the refractive index. As it turns out, the HRS signal is rather driven by the surface effects than LSPR peak shift, which is a volume effect. The best results were obtained for smaller nanoparticles, where a significant drop for the lowest glycerol addition was observed. A simple model was introduced to explain the HRS signal behaviour, where local surface modifications compete with nanoparticles' aggregation. A Figure of Merit was based on relative change of the HRS signal, namely $(\Delta I/I)/RIU$, with its value of around 4000. Along with the simplicity of the HRS measurement setup, it manifests the use of Hyper Rayleigh Scattering in sensing applications. Notably, UV-Vis spectroscopy turns out to be insufficient below 1% volume fraction of glycerol, as opposed to HRS.

The last but not least experimental part, described in Chapter 5.4, covers detection of metal ions. In this case, copper (II) bromide was added to 50 nm gold nanospheres. The UV-Vis spectra, Zeta potential measurements and Dynamic Light Scattering confirmed that below 1 mM $CuBr_2$ corona-structures are formed thanks to weak interactions between copper and citrate. Above this limit the nanoparticles aggregate. Various Figure of Merit possibilities were discussed: based on the HRS signal, the depolarization ratio or retardation parameter for vertical polarization. Since surface effects are desired, depolarization ratio-based FoM or a HRS signal based one are of choice. On the contrary, for all proposed UV-Vis-based sensing protocols, the FoM's uncertainty was higher or close to the actual value, which excludes colorimetric methods for such low copper content detection.

In conclusion, it has been shown that gold nanoparticles' Hyper Rayleigh Scattering is a promising tool for sensing purposes, as compared with standard colorimetry. Namely, gold nanotriangles exhibit significantly lower retardation parameters, as compared with centrosymmetrically-shaped nanoparticles. Moreover, sensing of small changes of surrounding medium refractive index can be effectively detected by gold nanospheres, as well as the presence of copper ions. HRS is an effective tool for sensing of significantly lower changes, as compared to UV-Vis methods.

It is worth noting that this thesis does not only focus on sensing applications, but also reveals the nature of phenomena occurring in studied samples. Thus, it is of great value also for understanding the Hyper Rayleigh Scattering of metallic nanoparticles.

Nevertheless, this study provokes questions, such as the behaviour of nanoparticles of other shapes possibly owing sharp tips in the case of surrounding medium refractive index change or metal ion detection. Moreover, before using the proposed method for actual sensing applications, the selectivity shall be addressed, for instance in terms of the surface derivatization for targeting analyses.

7. References

1. S. Kumar, P. Bushan, S. Bhattacharya, Fabrication of Nanostructures with Bottom-up Approach and Their Utility in Diagnostics, Therapeutics, and Others. In *Environmental, Chemical and Medical Sensors*, S. Bhattacharya, A. K. Agarwal, N. Chanda, A. Pandey, A. Kumar Sen, Ed. Springer Singapore: 2018; Vol. 8.
2. L. Yang, Fundamentals of Nanotechnology and Orthopedic Materials. In *Nanotechnology-Enhanced Orthopedic Materials*, L. Yang, Ed. Woodhead Publishing: 2015; Vol. 1.
3. F. Pease, S. Y. Chou, Lithography and Other Patterning Techniques for Future Electronics. *Proceedings of the IEEE* **2008**, *96*, 248-270.
4. W. Nunn, T. K. Truttmann, B. Jalan, A Review of Molecular-Beam Epitaxy of Wide Bandgap Complex Oxide Semiconductors. *Journal of Materials Research* **2021**, *36*, 4846-4864.
5. C. Y. Chang, F. Kai, *Gaas High-Speed Devices*; Wiley, 1994.
6. P. M. Martin, P. Martin, *Introduction to Surface Engineering and Functionally Engineered Materials*; Wiley, 2011.
7. J. Orton, T. Foxon, *Molecular Beam Epitaxy: A Short History*; Oxford University Press: New York, United States of America, 2015.
8. J-O. Carlsson, P. M. M., Chemical Vapor Deposition. In *Handbook of Deposition Technologies for Films and Coatings*, P. M. Martin, Ed. Elsevier: 2010.
9. S. Sanders, D. Stümmler, P. Pfeiffer, N. Ackermann, G. Simkus, M. Heuken, P. K. Baumann, A. Vescan, H. Kalisch, Chemical Vapor Deposition of Organic-Inorganic Bismuth-Based Perovskite Films for Solar Cell Application. *Scientific Reports* **2019**, *9*, 9774.
10. M. Sabzi, S. H. Mousavi Anijdan, M. Shamsodin, M. Farzam, A. Hojjati-Najafabadi, P. Feng, N. Park, U. Lee, A Review on Sustainable Manufacturing of Ceramic-Based Thin Films by Chemical Vapor Deposition (Cvd): Reactions Kinetics and the Deposition Mechanisms. *Coatings* **2023**, *13*, 188.
11. X-D. Wang, K. Vinodgopal, G-P. Dai, Synthesis of Carbon Nanotubes by Catalytic Chemical Vapor Deposition. In *Perspective of Carbon Nanotubes*, H. El-Din Saleh, S. M. M. El-Sheikh, Ed. IntechOpen: 2018.
12. J. Turkevich, P. C. Stevenson, J. Hillier, A Study of the Nucleation and Growth Processes in the Synthesis of Colloidal Gold. *Discussion of the Faraday Society* **1951**, *11*, 55-75.
13. Frens, G., Controlled Nucleation for the Regulation of the Particle Size in Monodisperse Gold Suspensions. *Nature Physical Science* **1973**, *241*, 20-22.
14. Y-Y. Yu, S-S. Chang, C-L. Lee, C. R. C. Wang, Gold Nanorods: Electrochemical Synthesis and Optical Properties. *The Journal of Physical Chemistry B* **1997**, *101*, 6661-6664.
15. J. Olesiak-Banska, M. Gordel, K. Matczyszyn, V. Shynkar, J. Zyss, M. Samoc, Gold Nanorods as Multifunctional Probes in a Liquid Crystalline DNA Matrix. *Nanoscale* **2013**, *5*, 10975-10981.
16. J. A. Jenkins, T. J. Wax, J. Zhao, Seed-Mediated Synthesis of Gold Nanoparticles of Controlled Sizes to Demonstrate the Impact of Size on Optical Properties. *Journal of Chemical Education* **2017**, *94*, 1090-1093.
17. T. K. Sau, C. J. Murphy, Seeded High Yield Synthesis of Short Au Nanorods in Aqueous Solution. *Langmuir* **2004**, *20*, 6414-6420.
18. J. G. Mehtala, D. Y. Zemlyanov, J. P. Max, N. Kadasala, S. Zhao, A. Wei, Citrate-Stabilized Gold Nanorods. *Langmuir* **2014**, *30*, 13727-13730.
19. R. Venkatesan, A. Pichaimani, K. Hari, P. K. Balasubramanian, J. Kulandaivel, K.

Premkumar, Doxorubicin Conjugated Gold Nanorods: A Sustained Drug Delivery Carrier for Improved Anticancer Therapy. *Journal of Materials Chemistry B* **2013**, *1*, 1010-1018.

20. R. Deska, P. Obstarczyk, K. Matczyszyn, J. Olesiak-Banska, Circular Dichroism of Gold Bipyramid Dimers. *The Journal of Physical Chemistry Letters* **2021**, *12*, 5208-5213.

21. H. Zhang, J. Liu, Gold Nanobipyramids as Saturable Absorbers for Passively Q-Switched Laser Generation in the 1.1 Mm Region. *Optics Letters* **2016**, *41*, 1150-1152.

22. C. Kuttner, M. Mayer, M. Dulle, A. Moscoso, J. M. Lopez-Romero, S. Forster, A. Fery, J. Perez-Juste, R. Contreras-Caceres, Seeded Growth Synthesis of Gold Nanotriangles: Size Control, Saxs Analysis, and Sers Performance. *ACS Applied Materials & Interfaces* **2018**, *10*, 11152-11163.

23. F. Liebig, R. M. Sarhan, M. Bargheer, C. N. Z. Schmitt, A. H. Poghosyan, A. A. Shahinyan, J. Koetz, Spiked Gold Nanotriangles: Formation, Characterization and Applications in Surface-Enhanced Raman Spectroscopy and Plasmon-Enhanced Catalysis. *RSC Advances* **2020**, *10*, 8152-8160.

24. F. Liebig, R. Henning, R. M. Sarhan, C. Prietzel, C. N. Z. Schmitt, M. Bargheer, J. Koetz, A Simple One-Step Procedure to Synthesise Gold Nanostars in Concentrated Aqueous Surfactant Solutions. *RSC Advances* **2019**, *9*, 23633-23641.

25. Fabris, L., Gold Nanostars in Biology and Medicine: Understanding Physicochemical Properties to Broaden Applicability. *The Journal of Physical Chemistry C* **2020**, *124*, 26540-26553.

26. J-E. Park, Y. L., J-M. Nam, Precisely Shaped, Uniformly Formed Gold Nanocubes with Ultrahigh Reproducibility in Single-Particle Scattering and Surface-Enhanced Raman Scattering. *Nano Letters* **2018**, *18*, 6475-6482.

27. H. Cang, T. Sun, Z-Y. Li, J. Chen, B. J. Wiley, Y. Xia, X. Li, Gold Nanocages as Contrast Agents for Spectroscopic Optical Coherence Tomography. *Optics Letters* **2005**, *30*, 3048-3050.

28. D. Zhang, X. Qin, T. Wu, Q. Qiao, Q. Song, Z. Zhang, Extracellular Vesicles Based Self-Grown Gold Nanopopcorn for Combinatorial Chemo-Photothermal Therapy. *Biomaterials* **2019**, *197*, 220-228.

29. L. M. Liz-Marzan, J. Perez-Juste, I. Pastoriza-Santos, Plasmonics of Gold Nanorods. Considerations for Biosensing. In *Nanomaterials for Application in Medicine and Biology*, M. Giersig, G. B. Khomutov, Ed. Springer, Dordrecht: 2008; pp 103-111.

30. S. I. Shopova, C. W. Blackledge, A. T. Rosenberger, N. F. Materer, Gold Nanorods Grown from Hgte Nanoparticles Directly on Various Surfaces. *Applied Physics Letters* **2006**, *89*, 023120.

31. S. L. Smitha, K. G. Gopchandran, T. R. Ravindran, V. S. Prasad, Gold Nanorods with Finely Tunable Longitudinal Surface Plasmon Resonance as Sers Substrates. *Nanotechnology* **2011**, *22*, 265705.

32. H-H. Chang, C. J. Murphy, Mini Gold Nanorods with Tunable Plasmonic Peaks Beyond 1000 Nm. *Chemistry of Materials* **2018**, *30*, 1427-1435.

33. K. Brach, K. Matczyszyn, J. Olesiak-Banska, M. Gordel, M. Samoc, Stabilization of DNA Liquid Crystals on Doping with Gold Nanorods. *Physical Chemistry Chemical Physics* **2016**, *18*, 7278-7283.

34. E. D. SoRelle, O. Liba, Z. Hussain, M. Gambhir, A. de la Zerda, Biofunctionalization of Large Gold Nanorods Realizes Ultrahighsensitivity Optical Imaging Agents. *Langmuir* **2015**, *31*, 12339-12347.

35. M. Klekotko, K. Matczyszyn, J. Siednienko, J. Olesiak-Banska, K. Pawlik, M. Samoc, Bio-Mediated Synthesis, Characterization and Cytotoxicity of Gold Nanoparticles. *Physical Chemistry Chemical Physics* **2015**, *17*, 29014-29019.

36. X. Zhuo, X. Zhu, Q. Li, Z. Yang, J. Wang, Gold Nanobipyramid-Directed Growth of Length-Variable Silver Nanorods with Multipolar Plasmon Resonances. *ACS Nano* **2015**, *9*, 7523-7535.

37. Z. Sun, A. Umar, J. Zeng, X. Luo, L. Song, Z. Zhang, Z. Chen, J. Li, F. Su, Y. Huang, Highly Pure Gold Nanotriangles with Almost 100% Yield for Surface Enhanced Raman Scattering. *ACS Applied Nano Materials* **2022**, *5*, 1220-1231.

38. S-J. Yoon, Y-S. Nam, J. Y. Lee, J. Y. Kim, Y. Lee, K-B. Lee, Highly Sensitive Colorimetric Determination of Nitrite Based on the Selective Etching of Concave Gold Nanocubes. *Microchimica Acta* **2021**, *188*.

39. S. Chatterjee, L. Ricciardi, J. I. Deitz, R. E. A. Williams, D. W. McComb, G. Strangi, Manipulating Acoustic and Plasmonic Modes in Gold Nanostars. *Nanoscale Advances* **2019**, *1*, 2690-2698.

40. M. Bardhan, B. Satpati, T. Ghosh, D. Senapati, Synergistically Controlled Nano-Templated Growth of Tunable Gold Bud-to-Blossom Nanostructures: A Pragmatic Growth Mechanism. *Journal of Materials Chemistry C* **2014**, *2*, 3795-3804.

41. S. E. Skrabalak, J. Chen, Y. Sun, X. Lu, L. Au, C. M. Cobley, Y. Xia, Gold Nanocages: Synthesis, Properties, and Applications. *Accounts of Chemical Research* **2008**, *41*, 1587-1595.

42. H-H. Perkampus, *Uv-Vis Spectroscopy and Its Applications*; Springer-Verlag Berlin Heidelberg: Berlin, 1992.

43. A. Djorović, S. J. Oldenburg, J. Grand, E. C. Le Ru, Extinction-to-Absorption Ratio for Sensitive Determination of the Size and Dielectric Function of Gold Nanoparticles. *ACS Nano* **2020**, *14*, 17597-17605.

44. C. A. De Caro, H. Claudia, *Uv/Vis Spectrophotometry - Fundamentals and Applications*; Mettler-Toledo, 2015.

45. W. Haiss, N. T. K. Thanh, J. Aveyard, D. G. Fernig, Determination of Size and Concentration of Gold Nanoparticles from Uv−Vis Spectra. *Analytical Chemistry* **2007**, *79*, 4215-4221.

46. L. de Broglie, *Recherches Sur La Théorie Des Quanta*, 1924; Vol. 10.

47. R. F. Egerton, *Physical Principles of Electron Microscopy. An Introduction to Tem, Sem and Aem*; Springer Science+Business Media, Inc.: USA, 2005.

48. C. Davisson, L.H. Germer, Diffraction of Electrons by a Crystal of Nickel. *Physical Review* **1927**, *30*, 705-740.

49. Ul-Hamid, A., *A Beginners' Guide to Scanning Electron Microscopy*; Springer Nature Switzerland AG: Switzerland, 2018.

50. M. Azubel, J. Koivisto, S. Malola, D. Bushnell, G. L. Hura, A. L. Koh, H. Tsunoyama, T. Tsukuda, M. Pettersson, H. Häkkinen, R. D. Kornberg, Electron Microscopy of Gold Nanoparticles at Atomic Resolution. *Science* **2014**, *345*, 909-912.

51. A. Goldstein, Y. Soroka, M. Frušić-Zlotkin, I. Popov, R. Kohen, High Resolution Sem Imaging of Gold Nanoparticles in Cells and Tissues. *Journal of Microscopy* **2014**, *256*, 237-247.

52. S. Naveenraj, R. V. Mangalaraja, J. J. Wu, A. M. Asiri, S. Anandan, Gold Triangular Nanoprisms and Nanodecahedra: Synthesis and Interaction Studies with Luminol toward Biosensor Applications. *Langmuir* **2016**, *32*, 11854-11860.

53. P. Elia, R. Zach, S. Hazan, S. Kolusheva, Z. Porat, Y. Zeiri, Green Synthesis of Gold Nanoparticles Using Plant Extracts as Reducing Agents. *International Journal of Nanomedicine* **2014**, *9*, 4007-4021.

54. D. S. Negi, Recent Developments in the Colorimetric Sensing of Biological Molecules Using Gold Nanoparticles-Based Probes. *Talanta Open* **2022**, *6*, 100122.

55. H. R. Hegde, S. Chidangil, R. K. Sinha, Refractive Index Sensitivity of Au Nanostructures in Solution and on the Substrate. *Journal of Materials Science: Materials in Electronics* **2022**, *33*, 4011-4024.

56. Kirby, B. J., *Micro- and Nanoscale Fluid Mechanics. Transport in Microfluidic Devices*; Cambridge University Press: USA, 2010.

57. S. Skoglund, J. Hedberg, E. Yunda, A. Godymchuk, E. Blomberg, I. O. Wallinder, Difficulties and Flaws in Performing Accurate Determinations of Zeta Potentials of Metal

Nanoparticles in Complex Solutions—Four Case Studies. *PLoS One* **2017**, *12*, 0181735.
58. G. V. Lowry, R. J. Hill, S. Harper, A. F. Rawle, C. O. Hendren, F. Klaessig, U. Nobbmann, P. Sayre, J. Rumble, Guidance to Improve the Scientific Value of Zeta-Potential Measurements in Nanoehs. *Environmental Science: Nano* **2016**, *3*, 953-965.
59. T. L. Doane, C-H. Chuang, R. J. Hill, C. Burda, Nanoparticle Z -Potentials. *Accounts of Chemical Research* **2012**, *45*, 317-326.
60. N. C. Ford, Jr., Light Scattering Apparatus. In *Dynamic Light Scattering. Applications of Photon Correlation Spectroscopy*, R. Pecora, Ed. 1985.
61. S. Falke, C. Betzel, Dynamic Light Scattering (Dls). In *Radiation in Bioanalysis*, A. Pereira, P. Tavares, P. Limao-Vieira, Ed. Springer Nature Switzerland AG: 2019; Vol. 8.
62. Provencher, S. W., Contin: A General Purpose Constrained Regularization Program for Inverting Noisy Linear Algebraic and Integral Equations. *Computer Physics Communications* **1982**, *27*, 229-242.
63. A. Wishard, B. C. Gibb, Dynamic Light Scattering – an All-Purpose Guide for the Supramolecular Chemist. *Supramolecular Chemistry* **2019**, *31*, 608-615.
64. H. Fissan, S. Ristig, H. Kaminski, C. Asbach, M. Epple, Comparison of Different Characterization Methods for Nanoparticle Dispersions before and after Aerosolization. *Analytical Methods* **2014**, *6*, 7324-7334.
65. R. Ragheb, U. Nobbmann, Multiple Scattering Effects on Intercept, Size, Polydispersity Index, and Intensity for Parallel (Vv) and Perpendicular (Vh) Polarization Detection in Photon Correlation Spectroscopy. *Scientific Reports* **2020**, *10*, 21768.
66. Pluchery, O., Optical Properties of Gold Nanoparticles. In *Gold Nanoparticles for Physics, Chemistry and Biology*, C. Louis, O. Pluchery, Ed. Imperial College Press: London, 2012.
67. H. H. Nguyen, J. Park, S. Kang, M. Kim, Surface Plasmon Resonance: A Versatile Technique for Biosensor Applications. *Sensors* **2015**, *15*, 10481-10510.
68. C. Y. Chain, M. A. D. Millone, J. S. Cisneros, E. A. Ramirez, M. E. Vela, Surface Plasmon Resonance as a Characterization Tool for Lipid Nanoparticles Used in Drug Delivery. *Analytical Chemistry* **2021**, *8*, 605307.
69. Bakhtiar, R., Surface Plasmon Resonance Spectroscopy: A Versatile Technique in a Biochemist's Toolbox. *Journal of Chemical Education* **2013**, *90*, 203-209.
70. Mayergoyz, I. D., *Plasmon Resonances in Nanoparticles*; World Scientific Publishing Co. Pte. Ltd.: Singapore, 2013; Vol. 6.
71. M. Forough, E. Bilgen, O. P. Cetinkol, Advanced Sensor Technology. In *Advanced Sensor Technology*, A. Barhoum, Z. Altintas, Ed. Elsevier: 2023.
72. Garnett, J. C. M., Colours in Metal Glasses and in Metallic Films. *Philosophical Transactions of the Royal Society of London* **1904**, *203*, 385-420.
73. M. Born, E. Wolf, Optics of Metals. In *Principles of Optics : Electromagnetic Theory of Propagation, Interference and Diffraction of Light*, 6 ed.; M. Born, E. Wolf, Ed. Elsevier Science & Technology: Great Britain, 1980.
74. R. Murata, K. Inoue, L. Wang, S. Ye, A. Morita, Dispersion of Complex Refractive Indices for Intense Vibrational Bands. I. Quantitative Spectra. *The Journal of Physical Chemistry B* **2021**, *125*, 9794-9803.
75. Maier, S. A., *Plasmonics: Fundamentals and Applications*; Springer Science+Business Media LLC: Bath, 2007.
76. P. B. Johnson, R. W. Christy, Optical Constants of the Noble Metals. *Physical Review B* **1972**, *6*, 4370.
77. C. F. Bohren, D. R. Huffman, *Absorption and Scattering of Light by Small Particles*; John Wiley & Sons Inc.: New York, NY, USA, 1983.
78. K. M. Mayer, J. H. Hafner, Localized Surface Plasmon Resonance Sensors. *Chemical Reviews* **2011**, *111*, 3828-3857.
79. L. J. E. Anderson, K. M. Mayer, R. D. Fraleigh, Y. Yang, S. Lee, J. H. Hafner,

Quantitative Measurements of Individual Gold Nanoparticle Scattering Cross Sections. *The Journal of Physical Chemistry C* **2010**, *114*, 11127-11132.

80. Mie, G., Beiträge Zur Optik Trüber Medien, Speziell Kolloidaler Metallösungen. *Annalen der Physik* **1908**, *4*, 377-445.

81. A. Hohenau, A. Leitner, F. R. Aussenegg, Near-Field and Far-Field Properties of Nanoparticle Arrays. In *Surface Plasmon Nanophotonics*, M. L. Brongersma, P. G. Kik, Ed. Springer: Dordrecht, The Netherlands, 2007.

82. M. Meier, A. Wokaun, Enhanced Field on Large Metal Particles: Dynamic Depolarization. *Optics Letters* **1983**, *8*, 581-583.

83. H. Kuwata, H. Tamaru, K. Esumi, K. Miyano, Resonant Light Scattering from Metal Nanoparticles: Practical Analysis Beyond Rayleigh Approximation. *Applied Physics Letters* **2003**, *83*, 4625.

84. C. P. Burrows, W. L. Barnes, Large Spectral Extinction Due to Overlap of Dipolar and Quadrupolar Plasmonic Modes of Metallic Nanoparticles in Arrays. *Optics Express* **2010**, *18*, 3187-3198.

85. Schatz, G. C., Electrodynamics of Nonspherical Noble Metal Nanoparticles and Nanoparticle Aggregates. *Journal of Molecular Structure (Theochem)* **2001**, *573*, 73-80.

86. L. Cheng, G. Zhu, G. Liu, L. Zhu, Fdtd Simulation of the Optical Properties for Gold Nanoparticles. *Materials Research Express* **2020**, *7*, 125009.

87. T. Grosges, A. Vial, D. Barchiesi, Models of near-Field Spectroscopic Studies: Comparison between Finite-Element and Finite-Difference Methods. *Optics Express* **2005**, *13*, 8483-8497.

88. J. Grand, E. Le Ru, Practical Implementation of Accurate Finite-Element Calculations for Electromagnetic Scattering by Nanoparticles. *Plasmonics* **2020**, *15*, 109-121.

89. Q. Sun, E. Klaseboer, A Non-Singular, Field-Only Surface Integral Method Forinteractions between Electric and Magnetic Dipoles Andnano-Structures. *Annalen der Physik* **2022**, *534*, 2100397.

90. K. Saha, S. S. Agasti, C. Kim, X. Li, V. M. Rotello, Gold Nanoparticles in Chemical and Biological Sensing. *Chemical Reviews* **2012**, *112*, 2739-2779.

91. E. Ferrari, Gold Nanoparticle-Based Plasmonic Biosensors. *Biosensors* **2023**, *13*, 411.

92. X. Hu, Y. Zhang, T. Ding, J. Liu, H. Zhao, Multifunctional Gold Nanoparticles: A Novel Nanomaterial for Various Medical Applications and Biological Activities. *Frontiers in Bioengineering and Biotechnology* **2020**, *8*, 990.

93. A. Rossi, M. Zannotti, M. Cuccioloni, M. Minicucci, L. Petetta, M. Angeletti, R. Giovannetti, Silver Nanoparticle-Based Sensor for the Selective Detection of Nickel Ions. *Nanomaterials (Basel)* **2021**, *11*, 1733.

94. A. Loiseau, V. Asila, G. Boitel-Aullen, M. Lam, M. Salmain, S. Boujday, Silver-Baded Plasmonic Nanoparticles for and Their Use in Biosensing. *Biosensors (Basel)* **2019**, *9*, 78.

95. J. Chen, S. Shi, R. Su, W. Qi, R. Huang, M. Wang, L. Wang, Z. He, Optimization and Application of Reflective Lspr Optical Fiber Biosensors Based on Silver Nanoparticles. *Sensors* **2015**, *15*, 12205-12217.

96. M. B. Gawande, A. Goswami, F-X. Felpin, T. Asefa, X. Huang, R. Silva, X. Zou, R. Zboril, R. S. Varma, Cu and Cu-Based Nanoparticles: Synthesis and Applications in Catalysis. *Chemical Reviews* **2016**, *116*, 3722-3811.

97. B. D. Harishchandra, M. Pappuswamy, A. PU, G. Shama, P. A, V. A. Arumugam, T. Periyaswamy, R. Sundaram, Copper Nanoparticles: A Review on Synthesis, Characterization and Applications. *Asian Pacific Journal of Cancer Biology* **2020**, *5*, 201-210.

98. K. Shah, N. K. Sharma, V. Sajal, Simulation of Lspr Based Fiber Optic Sensor Utilizing Layer of Platinum Nanoparticles. *Optik* **2018**, *154*, 530-537.

99. H. Vahed, E. Ghazanfari, Sensitivity Enhancement of a Nanocomposite-Based Fiber Optics Sensor with Platinum Nanoparticles. *Optica Applicata* **2019**, *XLIX*, 65-74.

100. L. Wang, M. H. Kafshgari, M. Meunier, Optical Properties and Applications of Plasmonic-Metal Nanoparticles. *Advanced Functional Materials* **2020**, *30*.
101. A. M. Smith, M. C. Mancini, S. Nie, Second Window for *in Vivo* Imaging. *Nature Nanotechnology* **2009**, *4*, 710-711.
102. E. Solati, D. Dorranian, Comparison between Silver and Gold Nanoparticles Prepared by Pulsed Laser Ablation in Distilled Water. *Journal of Cluster Science* **2015**, *26*, 727-742.
103. H. P. Paudel, A. Safaei, M. N. Leuenberger, Nanoplasmonics in Metallic Nanostructures and Dirac Systems. In *Nanoplasmonics - Fundamentals and Applications*, Barbillon, G., Ed. Intech Open: London, 2017.
104. J. Perez-Juste, I. Pastoriza-Santos, L. M. Liz-Marzan, P. Mulvaney, Gold Nanorods: Synthesis, Characterization and Applications. *Coordination Chemistry Reviews* **2005**, *249*, 1870-1901.
105. H. Chen, X. Kou, Z. Yang, W. Ni, J. Wang, Shape- and Size-Dependent Refractive Index Sensitivity of Gold Nanoparticles. *Langmuir* **2008**, *24*, 5233-5237.
106. A. M. Ibrahim, H. A. A. Alzahrani, M. M. Abd El-Latif, M. M. Selim, Influence of Different Stabilizers on the Morphology of Gold Nanoparticles. *Bulletin of the National Research Centre* **2019**, *43*, 33.
107. G. Liu, M. Lu, X. Huang, T. Li, D. Xu, Application of Gold-Nanoparticle Colorimetric Sensing to Rapid Food Safety Screening. *Sensors* **2018**, *18*, 4166.
108. J. Olesiak-Banska, M. Waszkielewicz, P. Obstarczyk, M. Samoc, Two-Photon Absorption and Photoluminescence of Colloidal Gold Nanoparticles and Nanoclusters. *Chemical Society Reviews* **2019**, *48*, 4087-4117.
109. Mooradian, A., Photoluminescence of Metals. *Physical Review Letters* **1969**, *22*, 185-187.
110. G. T. Boyd, Z. H. Yu, Y. R. Shen, Photoinduced Luminescence from the Noble Metals and Its Enhancement on Roughened Surfaces. *Physical Review B* **1986**, *33*, 7923-7936.
111. Y. Fang, W-S. Chang, B. Willingham, P. Swanglap, S. Dominguez-Medina, S. Link, Plasmon Emission Quantum Yield of Single Gold Nanorods as a Function of Aspect Ratio. *ACS Nano* **2012**, *6*, 7177-7184.
112. B. E. A. Saleh, M. C. Teich, *Fundamentals of Photonics*; Wiley - Interscience, 2007.
113. A. Javadi, I. Söllner, M. Arcari, S. Lindskov Hansen, L. Midolo, S. Mahmoodian, G. Kirsanske, T. Pregnolato, E. H. Lee, J. D. Song, S. Stobbe, P. Lodahl, Single-Photon Non-Linear Optics with a Quantum Dot in a Waveguide. *Nature Communications* **2015**, *6*, 8655.
114. S. Sun, K. Müller, Single-Photon Nonlinear Optics with a Semiconductor Quantum Dot. In *Semicondutors and Semimetals*, S. T. Cundiff, M. Kira, Ed. Elsevier: 2020; Vol. 105, pp 387-416.
115. M. Gullans, D. E. Chang, F. H. L. Koppens, F. J. Garcia de Abajo, M. D. Lukin, Single-Photon Nonlinear Optics with Graphene Plasmons. *Physical Review Letters* **2013**, *111*, 247401.
116. R. W. Boyd, *Nonlinear Optics. Third Edition*; Elsevier Inc.: USA, 2008.
117. S. G. He, *Nonlinear Optics and Photonics*; Oxford University Press: New York, 2015.
118. M. Dudek, A. Kaczmarek-Kędziera, R. Deska, J. Trojnar, P. Jasik, P. Młynarz, M. Samoć, K. Matczyszyn, Linear and Nonlinear Optical Properties of Azobenzene Derivatives Modified with an (Amino)Naphthalene Moiety. *The Journal of Physical Chemistry B* **2022**, *126*, 6063-6073.
119. Z. Szakacs, E. Vauthey, Excited-State Symmetry Breaking and the Laporte Rule. *The Journal of Physical chemistry Letters* **2021**, *12*, 4067-4071.
120. H. Wei, Y. Wang, Y. Wang, W. Fan, L. Zhou, M. Long, S. Xiao, J. He, Giant Two-Photon Absorption in Mxene Quantum Dots. *Optics Express* **2022**, *30*, 8482-8493.
121. DI K-D. Bauer. Second Harmonic Generation in Centrosymmetric Media. Johannes Kepler University Linz, Linz, Austria, 2019.
122. G. New, *Introduction to Nonlinear Optics*; Cambridge University Press, 2011.
123. D. Epperlein, B. Dick, G. Marowsky, Second-Harmonic Generation in Centro-

Symmetric Media. *Applied Physics B* **1987**, *44*, 5-10.

124. G. Le Breton, O. Bonhomme, P-F. Brevet, E. Benichou, C. Loison, First Hyperpolarizability of Water at the Air–Vapor Interface: A Qm/Mm Study Questions Standard Experimental Approximations. *Physical Chemistry Chemical Physics* **2019**, *23*, 24932.

125. D. Verreault, K. Moreno, E. Merlet, F. Amadietz, B. Kauffmann, Y. Ferrand, C. Olivier, V. Rodriguez, Hyper-Rayleigh Scattering as a New Chiroptical Method: Uncovering the Nonlinear Optical Activity of Aromatic Oligoamide Foldamers. *Journal of the American Chemical Society* **2020**, *142*, 257-263.

126. K. Clays, A. Persoons, Hyper-Rayleigh Scattering in Solution. *Review of Scientific Instruments* **1992**, *63*, 3285-3289.

127. Y. El Harfouch, E. Benichou, F. Bertorelle, I. Russier-Antoine, C. Jonin, N. Lascoux, P-F. Brevet, Effect of a Thioalkane Capping Layer on the First Hyperpolarizabilities of Gold and Silver Nanoparticles. *Journal of Physics: Condensed Matter* **2012**, *24*, 124104.

128. J. Duboisset, G. Matar, I. Russier-Antoine, E. Benichou, G. Bachelier, C. Jonin, D. Fichieux, F. Besson, P-F. Brevet, First Hyperpolarizability of the Natural Aromatic Amino Acids Tryptophan, Tyrosine, and Phenylalanine and the Tripeptide Lysine−Tryptophan−Lysine Determined by Hyper-Rayleigh Scattering. *The Journal of Physical Chemistry B* **2010**, *114*, 13861-13865.

129. F. W. Vance, B. I. Lemon, J. T. Hupp, Enormous Hyper-Rayleigh Scattering from Nanocrystalline Gold Particle Suspensions. *The Journal of Physical Chemistry B* **1998**, *102*, 10091-10093.

130. J. Campo, F. Desmet, W. Wenseleers, E. Goovaerts, Highly Sensitive Setup for Tunable Wavelength Hyper-Rayleigh Scattering with Parallel Detection and Calibration Data for Various Solvents *Optics Express* **2009**, *17*, 4587-4604.

131. I. Russier-Antoine, E. Benichou, G. Bachelier, C. Jonin, P-F. Brevet, Multipolar Contributions of the Second Harmonic Generation from Silver and Gold Nanoparticles. *The Journal of Physical Chemistry C* **2007**, *111*, 9044-9048.

132. J. I. Dadap, J. Shan, K. B. Eisenthal, T. F. Heinz, Second-Harmonic Rayleigh Scattering from a Sphere of Centrosymmetric Material. *Physical Review Letters* **1999**, *83*, 4045.

133. J. Butet, G. Bachelier, I. Russier-Antoine, C. Jonin, E. Benichou, P.-F. Brevet, Interference between Selected Dipoles and Octupoles in the Optical Second-Harmonic Generation from Spherical Gold Nanoparticles. *Physical Review Letters* **2010**, *105*, 077401.

134. P. Nemec, F. Pasztor, M. Brajer, I. Nemec, Spectrally- and Polarization-Resolved Hyper-Rayleigh Scattering Measurements with Polarization-Insensitive Detection. *Optics Communications* **2017**, *388*, 21-28.

135. J. Nappa, G. Revillod, I. Russier-Antoine, E. Benichou, C. Jonin, P.F. Brevet, Electric Dipole Origin of the Second Harmonic Generation of Small Metallic Particles. *Physical Review B* **2005**, *71*, 165407.

136. J. Nappa, I. Russier-Antoine, E. Benichou, C. Jonin, P-F. Brevet, Second Harmonic Generation from Small Gold Metallic Particles: From the Dipolar to the Quadrupolar Response. *The Journal of Chemical Physics* **2006**, *125*, 184712.

137. J. Duboisset, P-F. Brevet, Second-Harmonic Scattering-Defined Topological Classes for Nano-Objects. *The Journal of Physical Chemistry C* **2019**, *123*, 25303-25308.

138. I. Russier-Antoine, G. Bachelier, V. Sabloniere, J. Duboisset, E. Benichou, C. Jonin, F. Bertorelle, P-F. Brevet, Surface Heterogeneity in Au-Ag Nanoparticles Probed by Hyper-Rayleigh Scattering. *Physical Review B* **2008**, *78*, 035436.

139. G. Revillod, I. Russier-Antoine, E. Benichou, C. Jonin, P-F. Brevet, Investigating the Interaction of Crystal Violet Probe Molecules on Sodium Dodecyl Sulfate Micelles with Hyper-Rayleigh Scattering. *The Journal of Physical Chemistry B* **2005**, *109*, 5383-5387.

140. S. Brasselet, J. Zyss, Multipolar Molecules and Multipolar Fields: Probing and Controlling the Tensorial Nature of Nonlinear Molecular Media. *Journal of the Optical Society of*

America B **1998**, *15*, 257-288.

141. G. S. Agarwal, S. S. Jha, Theory of Second Harmonic Generation at a Metal Surface with Surface Plasmon Excitation. *Solid State Communications* **1982**, *41*, 499-501.

142. C. K. Chen, A. R. B. de Castro, Y. R. Shen, Surface-Enhanced Second-Harmonic Generation. *Physical Review Letters* **1981**, *46*, 145-148.

143. E. C. Hao, G. C. Schatz, R. C. Johnson, J. T. Hupp, Hyper-Rayleigh Scattering from Silver Nanoparticles. *The Journal of Chemical Physics* **2002**, *117*, 5963.

144. F. W. Vance, B. I. Lemon, J. A. Ekhoff, J. T. Hupp, Interrogation of Nanoscale Silicon Dioxide/Water Interfaces Via Hyper-Rayleigh Scattering. *The Journal of Physical Chemistry B* **1998**, *102*, 1845-1848.

145. Y. El Harfouch, E. Benichou, F. Bertorelle, I. Russier-Antoine, C. Jonin, N. Lascoux, P-F. Brevet, Hyper-Rayleigh Scattering from Gold Nanorods. *The Journal of Physical Chemistry C* **2014**, *118*, 609-616.

146. I. Russier-Antoine, H. J. Lee, A. W. Wark, J. Butet, E. Benichou, C. Jonin, O. J. F. Martin, P-F. Brevet, Second Harmonic Scattering from Silver Nanocubes. *The Journal of Physical Chemistry C* **2018**, *122*, 17447-17455.

147. H. M. Ngo, N. D. Lai, I. Ledoux-Rak, High Second-Order Nonlinear Response of Platinum Nanoflowers: The Role of Surface Corrugation. *Nanoscale* **2016**, *8*, 3489-3495.

148. I. Russier-Antoine, J. Duboisset, G. Bachelier, E. Benichou, C. Jonin, N. Del Fatti, F. Vallee, A. Sanchez-Iglesias, I. Pastoriza-Santos, L. M. Liz-Marzan, P-F. Brevet, Symmetry Cancellations in the Quadratic Hyperpolarizability of Non-Centrosymmetric Gold Decahedra. *The Journal of Physical Chemistry Letters* **2010**, *1*, 874-880.

149. M. Torres, G. Pastor, I. Jimenez, F. Montero De Espinosa, Five-Fold Quasicrystal-Like Germinal Pattern in the Faraday Wave Experiment. *Chaos, Solitons & Fractals* **1995**, *5*, 2089-2091, 2093.

150. J. Lyu, F. Rondepierre, C. Jonin, P-F. Brevet, C. Hamon, D. Constantin, Shape-Controlled Second-Harmonic Scattering from Gold Nanotetrapods. *The Journal of Physical Chemistry C* **2022**, *126*, 9831-9835.

151. K. Nadolski, E. Benichou, N. Tarnowicz-Staniak, A. Żak, C. Jonin. K. Matczyszyn, P-F. Brevet, Adverse Role of Shape and Size in Second-Harmonic Scattering from Gold Nanoprisms. *The Journal of Physical Chemistry C* **2020**, *124*, 14797-14803.

152. A. Ruivo, C. Gomes, A. Lima, M. L. Botelho, R. Melo, A. Belchior, A. Pires de Matos, Gold Nanoparticles in Ancient and Contemporary Ruby Glass. *Journal of Cultural Heritage* **2008**, *9*, e134-e137.

153. J. C. Almeida, E. J. C. Davim, I. M. Miranda Salvado, M. H. V. Fernandes, F. M. Costa, F. Rey-Garcia, L. M. Francisco, A. B. Lopes, Red Ruby Glass from Gold Nanoparticles Obtained by Lasis - a New Approach. *Journal of Non-Crystalline Solids* **2020**, *537*, 119987.

154. S. Haslbeck, K-P. Martinek, L. Stievano, F. E. Wagner, Formation of Gold Nanoparticles in Gold Ruby Glass: The Influence of Tin. *Hyperfine Interactions* **2005**, *165*, 89-94.

155. H. Takebe, M. Okamoto, K. Mori, Fabrication of Gold Ruby Glasses Using Solar Panel Glass Cullet. *Journal of the Ceramic Society of Japan* **2021**, *129*, 590-593.

156. Carabineiro, S. A. C., Supported Gold Nanoparticles as Catalysts for the Oxidation of Alcohols and Alkanes. *Frontiers in Chemistry* **2019**, *7*, 702.

157. G. Li, R. Jin, Catalysis by Gold Nanoparticles: Carbon-Carbon Coupling Reactions. *Nanotechnology Reviews* **2013**, *2*, 529-545.

158. N. Tarnowicz-Staniak, S. Vazquez-Diaz, V. Pavlov, K. Matczyszyn, M. Grzelczak, Cellulose as an Inert Scaffold in Plasmon-Assisted Photoregeneration of Cofactor Molecules. *ACS Applied Materials & Interfaces* **2020**, *12*, 19377-19383.

159. A. Alshammari, V. N. Kalevaru, Supported Gold Nanoparticles as Promising Catalysts. In *Catalytic Application of Nano-Gold Catalysts*, N. K. Mishra, Ed. IntechOpen: 2016.

160. K. Gopinath, S. Gowri, V. Karthika, A. Arumugam, Green Synthesis of Gold Nanoparticles from Fruit Extract of Terminalia Arjuna, for the Enhanced Seed Germination Activity of Gloriosa Superba. *Journal of Nanostructure in Chemistry* **2014**, *4*, 115.
161. V. Giannini, A. I. Fernandez-Dominguez, S. C. Heck, S. A. Maier, Plasmonic Nanoantennas: Fundamentals and Their Use in Controlling the Radiative Properties of Nanoemitters. *Chemical Reviews* **2011**, *111*, 3888-3912.
162. A. Habib, X. Zhu, S. Fong, A. A. Yanik, Active Plasmonic Nanoantenna: An Emerging Toolbox from Photonics to Neuroscience. *Nanophotonics* **2020**, *9*, 3805-3829.
163. H. A. Atwater, A. Polman, Plasmonics for Improved Photovoltaic Devices. *Nature Materials* **2010**, *9*, 205-213.
164. A. F. Versiani, L. M. Andrade, E. M. N. Martins, S. Scalzo, J. M. Geraldo, C. R. Chaves, D. C. Ferreira, M. Ladeira, S. Guatimosim, L. O. Ladeira, F. G. da Fonseca, Gold Nanoparticles and Their Applications in Biomedicine. *Future Virology* **2016**, *11*, 293-309.
165. P. Si, N. Razmi, O. Nur, S. Solanki, C. M. Pandey, R. K. Gupta, B. D. Malhotra, M. Willander, A. de la Zerda, Gold Nanomaterials for Optical Biosensing and Bioimaging. *Nanoscale Advances* **2021**, *3*, 2679-2698.
166. P. K. Jain, K. S. Lee, I. H. El-Sayed, M. A. El-Sayed, Calculated Absorption and Scattering Properties of Gold Nanoparticles of Different Size, Shape, and Composition: Applications in Biological Imaging and Biomedicine. *The Journal of Physical Chemistry B* **2006**, *110*, 7238-7248.
167. J-L. Li, L. Wang, X-Y. Liu, Z-P. Zhang, H-C. Guo, W-M. Liu, S-H. Tang, *In Vitro* Cancer Cell Imaging and Therapy Using Transferrin-Conjugated Gold Nanoparticles. *Cancer Letters* **2009**, *274*, 319-326.
168. W. Qian, X. Huang, B. Kang, M. A. El-Sayed, Dark-Field Light Scattering Imaging of Living Cancer Cell Component from Birth through Division Using Bioconjugated Gold Nanoprobes. *Journal of Biomedical Optics* **2010**, *15*, 046025.
169. H. Yuan, C. G. Khoury, H. Hwang, C. M. Wilson, G. A. Grant, T. Vo-Dinh, Gold Nanostars: Surfactant-Free Synthesis, 3d Modelling, and Two-Photon Photoluminescence Imaging. *Nanotechnology* **2012**, *23*, 075102.
170. I. Maliszewska, E. Wanarska, A. C. Thompson, I. D. W. Samuel, K. Matczyszyn, Biogenic Gold Nanoparticles Decrease Methylene Blue Photobleaching and Enhance Antimicrobial Photodynamic Therapy. *Molecules* **2021**, *26*, 623.
171. C. Lian, M. Piksa, K. Yoshida, S. Persheyev, K. J. Pawlik, K. Matczyszyn, I. D. W. Samuel, Flexible Organic Light-Emitting Diodes for Antimicrobial Photodynamic Therapy. *npj Flexible Electronics* **2019**, *3*, 18.
172. T. Labouret, J-F. Audibert, R. B. Pansu, B. Palpant, Plasmon-Assisted Production of Reactive Oxygen Species by Single Gold Nanorods. *Small* **2015**, *11*, 4475-4479.
173. G. Baffou, F. C., R. Quidant, Applications and Challenges of Thermoplasmonics. *Nature Materials* **2020**, *19*, 946-958.
174. G. Hüttmann, R. B., On the Possibility of High-Precision Photothermal Microeffects and the Measurement of Fast Thermal Denaturation of Proteins. *IEEE Journal of Selected Topics in Quantum Electronics* **1999**, *5*, 954-962.
175. J. A. Garcia, D. Monzon-Hernandez, J. Manriquez, E. Bustos, One Step Method to Attach Gold Nanoparticles onto the Surface of an Optical Fiber Used for Refractive Index Sensing. *Optical Materials* **2016**, *51*, 208-212.
176. P. Tuersun, T. Yusufu, A. Yimiti, A. Sidike, Refractive Index Sensitivity Analysis of Gold Nanoparticles. *Optik* **2017**, *149*, 384-390.
177. R. Rojanathanes, A. Sereemaspun, N. Pimpha, V. Buasorn, P. Ekawong, V. Wiwanitkit, Gold Nanoparticle as an Alternative Tool for a Urine Pregnancy Test. *Taiwanese Journal of Obstetrics and Gynecology* **2008**, *47*, 296-299.
178. H. Chen, K. Zhou, G. Zhao, Gold Nanoparticles: From Synthesis, Properties to Their

Potential Application as Colorimetric Sensors in Food Safety Screening. *Trends in Food Science & Technology* **2018**, *78*, 83-94.

179. F. Tian, F. Bonnier, A. Casey, A. E. Shanahan, H. J. Byrne, Surface Enhanced Raman Scattering with Gold Nanoparticles: Effect of Particle Shape. *Analytical Methods* **2014**, *6*, 9116-9123.

180. C-C. Huang, H-T. Chang, Selective Gold-Nanoparticle-Based "Turn-on" Fluorescent Sensors for Detection of Mercury(Ii) in Aqueous Solution. *Analytical Chemistry* **2006**, *78*, 8332-8338.

181. J. Xu, H. Yu, Y. Hu, M. Chen, S. Shao, A Gold Nanoparticle-Based Fluorescence Sensor for High Sensitive and Selective Detection of Thiols in Living Cells. *Biosensors and Bioelectronics* **2016**, *75*, 1-7.

182. Y-C. Yeh, B. Creran, V. M. Rotello, Gold Nanoparticles: Preparation, Properties, and Applications in Bionanotechnology. *Nanoscale* **2012**, *4*, 1871-1880.

183. E. I. Laderman, E. Whitworth, E. Dumaual, M. Jones, A. Hudak, W. Hogrefe, J. Carney, J. Groen, Rapid, Sensitive, and Specific Lateral-Flow Immunochromatographic Point-of-Care Device for Detection of Herpes Simplex Virus Type 2-Specific Immunoglobulin G Antibodies in Serum and Whole Blood. *Clinical and Vaccine Immunology* **2008**, *15*, 159-163.

184. J-M. Nam, C. S. Thaxton, C. A. Mirkin, Nanoparticle-Based Bio-Bar Codes for the Ultrasensitive Detection of Proteins. *Science* **2003**, *301*, 1884-1886.

185. D. G. Georganopoulou, L. Chang, J-M. Nam, C. S. Thaxton, E. J. Mufson, W. L. Klein, C. A. Mirkin, Nanoparticle-Based Detection in Cerebral Spinal Fluid of a Soluble Pathogenic Biomarker for Alzheimer's Disease. *Proceedings of the National Academy of Sciences of the United States of America* **2005**, *102*, 2273-2276.

186. K. Nadolski, C. Jonin, E. Salmon, Z. Behel, K. Matczyszyn, P-F. Brevet, Sensitivity of Gold Nanoparticles Second Harmonic Scattering to Surrounding Medium Change. *Journal of Molecular Liquids* **2023**, *388*, 122704.

187. K. Nadolski, F. Rondepierre, C. Jonin, T. M. Goszczyński, K. Matczyszyn, P-F. Brevet, Sensing Copper(Ii) Ions with Hyper Rayleigh Scattering from Gold Nanoparticles. *The Journal of Physical Chemistry C* **2023**, *127*, 13097-13104.

188. L. Chen, F. Ji, Y. Xu, L. He, Y. Mi, F. Bao, B. Sun, X. Zhang, Q. Zhang, High-Yield Seedless Synthesis of Triangular Gold Nanoplates through Oxidative Etching. *Nano Letters* **2014**, *14*, 7201-7206.

189. M. R. Jones, C. A. Mirkin, Bypassing the Limitations of Classical Chemical Purification with DNA-Programmable Nanoparticle Recrystallization. *Angewandte Chemie International Edition* **2013**, *52*, 2886-2891.

190. B. Nikoobakht, M. A. El-Sayed, Preparation and Growth Mechanism of Gold Nanorods (Nrs) Using Seed-Mediated Growth Method. *Chemistry of Materials* **2003**, *15*, 1957-1962.